



Universiteit
Leiden
The Netherlands

X-ray-induced chemistry of water and related molecules in low-mass protostellar envelopes

Notsu, S.; Dishoeck, E.F. van; Walsh, C.; Bosman, A.D.; Nomura, H.

Citation

Notsu, S., Dishoeck, E. F. van, Walsh, C., Bosman, A. D., & Nomura, H. (2021). X-ray-induced chemistry of water and related molecules in low-mass protostellar envelopes. *Astronomy & Astrophysics*, 650, 1-34. doi:10.1051/0004-6361/202140667

Version: Accepted Manuscript

License: [Leiden University Non-exclusive license](#)

Downloaded from: <https://hdl.handle.net/1887/3275258>

Note: To cite this publication please use the final published version (if applicable).

X-ray induced chemistry of water and related molecules in low-mass protostellar envelopes

Shota Notsu^{1,2*}, Ewine F. van Dishoeck^{2,3}, Catherine Walsh⁴, Arthur D. Bosman⁵, and Hideko Nomura⁶

¹ Star and Planet Formation Laboratory, RIKEN Cluster for Pioneering Research, 2-1 Hirosawa, Wako, Saitama 351-0198, Japan
e-mail: shota.notsu@riken.jp

² Leiden Observatory, Faculty of Science, Leiden University, PO Box 9513, 2300 RA Leiden, The Netherlands

³ Max-Planck-Institut für Extraterrestrische Physik, Giessenbachstrasse 1, 85748 Garching, Germany

⁴ School of Physics and Astronomy, University of Leeds, Leeds, LS2 9JT, UK

⁵ Department of Astronomy, University of Michigan, 1085 South University Avenue, Ann Arbor, MI 48109, USA

⁶ National Astronomical Observatory of Japan, 2-21-1 Osawa, Mitaka, Tokyo 181-8588, Japan

Received February 26, 2021; Accepted April 14, 2021

ABSTRACT

Context. Water is a key molecule in star and planet forming regions. Recent water line observations toward several low-mass protostars suggest low water gas fractional abundances ($< 10^{-6}$ with respect total hydrogen density) in the inner warm envelopes ($r < 10^2$ au). Water destruction by X-rays has been proposed to influence the water abundances in these regions, but the detailed chemistry, including the nature of alternative oxygen carriers, is not yet understood.

Aims. We aim to understand the impact of X-rays on the composition of low-mass protostellar envelopes, focusing specifically on water and related oxygen bearing species.

Methods. We compute the chemical composition of two proto-typical low-mass protostellar envelopes using a 1D gas-grain chemical reaction network. We vary X-ray luminosities of the central protostars and thus the X-ray ionisation rates in the protostellar envelopes.

Results. The protostellar X-ray luminosity has a strong effect on the water gas abundances, both within and outside the H₂O snowline ($T_{\text{gas}} \sim 10^2$ K, $r \sim 10^2$ au). Outside, the water gas abundance increases with L_X , from $\sim 10^{-10}$ for low L_X to $\sim 10^{-8} - 10^{-7}$ at $L_X > 10^{30}$ erg s⁻¹. Inside, water maintains a high abundance of $\sim 10^{-4}$ for $L_X \lesssim 10^{29} - 10^{30}$ erg s⁻¹, with water and CO being the dominant oxygen carriers. For $L_X \gtrsim 10^{30} - 10^{31}$ erg s⁻¹, the water gas abundances significantly decrease just inside the water snowline (down to $\sim 10^{-8} - 10^{-7}$) and in the innermost regions with $T_{\text{gas}} \gtrsim 250$ K ($\sim 10^{-6}$). For these cases, the fractional abundances of O₂ and O gas reach $\sim 10^{-4}$ within the water snowline, and they become the dominant oxygen carriers. In addition, the fractional abundances of HCO⁺ and CH₃OH, which have been used as tracers of the water snowline, significantly increase/decrease within the water snowline, respectively, as the X-ray fluxes become larger. The fractional abundances of some other dominant molecules, such as CO₂, OH, CH₄, HCN, and NH₃, are also affected by strong X-ray fields, especially within their own snowlines. These X-ray effects are larger in lower density envelope models.

Conclusions. X-ray induced chemistry strongly affects the abundances of water and related molecules including O, O₂, HCO⁺, and CH₃OH, and can explain the observed low water gas abundances in the inner protostellar envelopes. In the presence of strong X-ray fields, gas-phase water molecules within the water snowline are mainly destroyed with ion-molecule reactions and X-ray induced photodissociation. Future observations of water and related molecules (using e.g., ALMA and ngVLA) will access the regions around protostars where such X-ray induced chemistry is effective.

Key words. Astrochemistry – ISM: molecules – Stars: formation – Stars: protostars – Protoplanetary disks –

1. Introduction

Water is essential for habitability of planets, and it is a key molecule in star and planet forming regions. Water acts as a gas coolant (e.g., Neufeld et al. 1995), and efficient coagulation of dust grains covered by water ice is a key process in planetesimal and planet formation (e.g., Okuzumi et al. 2012; Okuzumi & Tazaki 2019; Wada et al. 2013; Schoonenberg & Ormel 2017; Arakawa & Krijt 2021).

In diffuse and dense clouds, water gas and ice are important oxygen carriers (Melnick et al. 2020; van Dishoeck et al. 2021). In diffuse and cold gas (gas temperature $T_{\text{gas}} \lesssim 100$ K), water is mainly produced by ion-molecule reactions (Hollenbach et al. 2009). When such a cloud becomes opaque (extinction $A_V > 3$

mag) and cool ($T_{\text{gas}} \lesssim 20 - 30$ K) enough, water is also efficiently formed by hydrogenation of oxygen atoms sticking onto cold dust grain surfaces where it forms an icy mantle (e.g., Cuppen et al. 2010). Water ice is a dominant oxygen carrier in dark-clouds and pre-stellar cores (e.g., Öberg et al. 2011; Caselli et al. 2012; Marboeuf et al. 2014; Boogert et al. 2015; Taquet et al. 2016b; Melnick et al. 2020; van Dishoeck et al. 2021). In warm regions ($T_{\text{gas}} > 100$ K), water ice sublimates from the dust-grain surfaces into the gas phase. At temperatures above 250 K, H₂O is largely produced by gas-phase reactions of O and OH with H₂ (Baulch et al. 1992; Oldenberg et al. 1992). This high-temperature chemistry route dominates the formation of water in shocks, in the inner envelopes around protostars, and in the warm surface layers of protoplanetary disks.

Recently, water vapor emission from the inner warm en-

* RIKEN Special Postdoctoral Researcher (SPDR, Fellow)

velopes ($T_{\text{gas}} > 100$ K) of low-mass Class 0 protostars have been investigated using PdBI¹ (e.g., Jørgensen & van Dishoeck 2010; Persson et al. 2012, 2014, 2016), ALMA² (e.g., Bjerkeli et al. 2016; Jensen et al. 2019), and *Herschel*³/HIFI (e.g., van Dishoeck et al. 2011, 2021; Visser et al. 2013). The interferometric observations using PdBI and ALMA targeted the para- H_2^{18}O 203 GHz $3_{13} - 2_{20}$ line (upper state energy $E_{\text{up}}=203.7$ K), which is also considered to be a tracer of water emission in the inner warm regions and the position of the water snowline in Class II disks (Notsu et al. 2018, 2019). The velocity-resolved observations using *Herschel*/HIFI targeted several water lines, including the $3_{12} - 3_{03}$ lines of ortho- H_2^{16}O (1097 GHz, $E_{\text{up}}=249.4$ K) and ortho- H_2^{18}O (1096 GHz, $E_{\text{up}}=248.7$ K), and were part of the key program “Water in star-forming regions with *Herschel*” (WISH; van Dishoeck et al. 2011, 2021), which aimed to study the physics and chemistry of water during star formation across a range of masses and evolutionary stages. The water abundances in the outer cold envelopes were also investigated, using e.g., the ground-state ortho- H_2^{16}O 557 GHz $1_{10} - 1_{01}$ line ($E_{\text{up}}=61.0$ K, e.g., Kristensen et al. 2010, 2012; van Dishoeck et al. 2011, 2021; Coutens et al. 2012, 2013; Mottram et al. 2013; Schmalzl et al. 2014).

According to Persson et al. (2012, 2014, 2016), and Visser et al. (2013), the water gas abundance is around 6×10^{-5} with respect to total H_2 density in the inner warm envelope and the disk of NGC 1333-IRAS 2A, and this value is similar to the expected value ($\sim 10^{-4}$) if water molecules are mostly inherited from the water ice in dark-clouds and pre-stellar cores (e.g., Boogert et al. 2015). In contrast, the water gas abundances in the inner envelopes and disks of NGC 1333 IRAS 4A and 4B are lower by 1 – 3 orders of magnitude than the value of NGC 1333-IRAS 2A. While some of this decrease can be accounted for if the detailed small scale physical structure is considered, Persson et al. (2016) even found such low water gas abundances when using thin disk+envelope models. Questions on how the water abundance is changed from dense clouds to protostellar envelopes and planet-forming disks and the nature of the main oxygen carrier instead thus arise (van Dishoeck et al. 2021). Since ALMA has much higher sensitivity and higher spatial and spectral resolution compared with previous instruments, water line surveys toward more Class 0 (and also Class I) protostars are expected using ALMA. Recently, Jensen et al. (2019) reported ALMA detections of the para- H_2^{18}O 203 GHz ($3_{1,1} - 2_{2,0}$) line for the inner warm envelopes around three isolated low-mass Class 0 protostars (L483, B335 and BHR71-IRS1). The estimated H_2^{18}O column densities in the warm inner envelopes for the three objects are around a few $\times 10^{15} \text{ cm}^{-2}$ in a 0.4" beam, which is similar to that of NGC 1333 IRAS 4B, and around 10 times lower than that of NGC 1333 IRAS 2A (Persson et al. 2014). According to new observations by Harsono et al. (2020), water vapor is not abundant in the warm envelopes and disks around Class I protostars, and the upper limits of the water gas abundances averaged over the inner warm disks with $T_{\text{gas}} > 100$ K are $\sim 10^{-7} - 10^{-5}$ with respect to H_2 .

There is only limited information on other major oxygen carriers. In low-mass protostar observations, only one upper limit and a tentative detection are reported for O_2 lines. This

is partly because O_2 does not possess electric dipole-allowed rotational transition lines. Yıldız et al. (2013) observed the O_2 $3_3 - 1_2$ 487.2 GHz line ($E_{\text{up}} = 26.4$ K) and reported an upper limit O_2 gas abundance with respect to H_2 of 6×10^{-9} (3σ) towards the entire envelope of IRAS 4A using *Herschel*/HIFI, and they estimated that the observed O_2 gas abundance cannot be more than 10^{-6} for the inner warm region ($\lesssim 10^2$ au). Taquet et al. (2018) reported the tentative detection (3σ) of the $^{16}\text{O}^{18}\text{O}$ 234 GHz $2_1 - 0_1$ line ($E_{\text{up}} = 11.2$ K) toward the inner envelope around a low-mass protostar IRAS 16293-2422 B with ALMA. Assuming that the $^{16}\text{O}^{18}\text{O}$ was not detected and using CH_3OH as a reference species, Taquet et al. (2018) obtained an $\text{O}_2/\text{CH}_3\text{OH}$ abundance ratio $< 2 - 5$, which is 3 – 4 times lower abundance than that in comet 67P/Churyumov-Gerasimenko.

The low water gas abundances derived for the inner regions of protostellar envelopes are unexpected because it is assumed that all water ice inherited from the molecular cloud phase would be sublimated in this warm region. In tandem, observations have failed to identify sufficiently abundant alternative oxygen carriers. So, what has happened to the water? Stäuber et al. (2005, 2006) modeled the water gas chemistry including X-ray destruction processes, and suggested that water gas will be destroyed by strong X-ray fluxes in the inner warm envelopes of low-mass Class 0 and I protostars on relatively short timescales (~ 5000 yr). In addition, they suggested that FUV photons from the central source are less effective in destroying water compared with X-ray photons due to extinction. However, it is not yet understood that the nature of the major oxygen carriers under these conditions. Moreover, it is important to investigate whether HCO^+ and CH_3OH are also affected by strong X-ray fluxes, since they have been used as tracers of the water snowline (Visser et al. 2015; van ’t Hoff et al. 2018a,b; Leemker et al. 2021). The chemical model that Stäuber et al. (2005, 2006) adopted were limited. Most notably, they did not include detailed gas-grain interactions and grain-surface chemistry (e.g., Walsh et al. 2015). These additional reactions will be important in considering the abundances of water and related molecules, since major oxygen-bearing molecules including H_2O , CO_2 , and CH_3OH are efficiently formed on the grain surfaces.

In this study, we revisit the chemistry of water and related molecules in low-mass Class 0 protostellar envelopes, under various X-ray field strengths. We adopt a gas-grain chemical reaction network including X-ray induced chemical processes. We include gas-phase reactions, thermal and non-thermal gas-grain interactions, and grain-surface reactions, simultaneously. Through the calculations, we study the radial dependence of the abundance of water and related molecules on the strength of the X-ray field, and identify potential alternative oxygen carriers other than water. The outline of our model calculations are explained in Section 2. The results and discussion of our calculations are described in Sections 3 and 4, respectively. The conclusions are listed in Section 5.

¹ IRAM Plateau de Bure Interferometer, now NOEMA (NOthern Extended Millimeter Array)

² Atacama Large Millimeter/submillimeter Array

³ *Herschel* Space Observatory

2. Protostellar envelope models

2.1. Physical structure models

2.1.1. Temperature and number density profiles of Class 0 protostellar envelopes

For the physical structures of low-mass Class 0 protostellar envelopes, we adopted the radial gas temperature T_{gas} and molecular hydrogen number density n_{H_2} profiles for two sources; NGC 1333-IRAS 2A and NGC 1333-IRAS 4A⁴ from Kristensen et al. (2012) and Mottram et al. (2013). These are the best studied sources with well determined inner and outer water abundances (e.g., Persson et al. 2012, 2014, 2016; Mottram et al. 2013; Visser et al. 2013; van Dishoeck et al. 2021). The H^{13}CO^+ gas abundance (a good tracer of the water snowline) toward the envelope around IRAS 2A (van 't Hoff et al. 2018a) and an upper limit O_2 gas abundance toward the envelope around IRAS 4A (Yıldız et al. 2013) have been also reported. According to Jørgensen et al. (2007, 2009), the differences in luminosities L_{bol} and envelope masses M_{env} between these two objects are only a factor of 4 – 5 ($L_{\text{bol}} = 20L_{\odot}$ and $M_{\text{env}} = 1.0M_{\odot}$ for IRAS 2A, and $5.8L_{\odot}$ and $M_{\text{env}} = 4.5M_{\odot}$ for IRAS 4A). Thus, they are presumably in similar evolutionary stages of low-mass protostars. In addition, we used these two profiles in order to examine the effect of density differences on X-ray induced chemistry. Kristensen et al. (2012) derived these T_{gas} and n_{H_2} profiles using the 1D spherically symmetric dust radiative transfer code DUSTY (Ivezic & Elitzur 1997). In this procedure, the free model parameters (the radial profile, size, and mass) were fitted to the spatial extent of the sub-millimeter continuum (450 – 850 μm) emission and the spectral energy distribution (SED). These source models are appropriate on scales of a few 10^2 – a few 10^3 au. Several recent studies (e.g., Persson et al. 2016; Koumpia et al. 2017; van 't Hoff et al. 2018a) also adopted the same models to study the chemistry and line emission in these protostellar envelopes. In these models, the gas and dust temperatures are taken to be the same ($T_{\text{gas}} = T_{\text{dust}}$), and they are well mixed with a gas-to-dust mass ratio of 100:1.

Figure 1 shows the radial gas temperature and molecular hydrogen number density profiles for IRAS 2A and IRAS 4A. The radial temperature distributions are similar between these two models ($T_{\text{gas}} \sim 250$ K in the innermost region and $T_{\text{gas}} \sim 10$ K at the outer edge). At the same radii, the density in IRAS 4A is around 3 – 6 times larger than that in IRAS 2A. The differences in densities between these two objects gradually increase as the radii decrease. In the inner edge at $T_{\text{gas}} = 250$ K ($r \sim 35$ au), n_{H_2} in IRAS 2A is $4.9 \times 10^8 \text{ cm}^{-3}$ and n_{H_2} in IRAS 4A is $3.1 \times 10^9 \text{ cm}^{-3}$. The effects of the small scale structures such as disks are neglected, but they will lower the temperature for some fraction of the gas.

2.1.2. X-ray fields

The observed X-ray spectra from YSOs are usually fitted with the emission spectrum of a thermal plasma (e.g., Hofner & Churchwell 1997; Stauber et al. 2005; Bruderer et al. 2009). The thermal X-ray spectrum can be approximated with

$$F_{\text{X,in}}(E, r) = F_0(r) \exp(-E/kT_{\text{X}}) \text{ [photons s}^{-1} \text{ cm}^{-2} \text{ eV}^{-1}\text{]}, \quad (1)$$

where r is the radius in the envelope from the central protostar, $F_{\text{X,in}}(E, r)$ is the incident X-ray flux per unit energy, k is

⁴ In the remainder of this paper, we define NGC 1333-IRAS 2A and NGC 1333-IRAS 4A as “IRAS 2A” and “IRAS 4A”, respectively.

the Boltzmann constant, and T_{X} is the temperature of the X-ray emitting plasma. The factor $F_0(r)$ can be calculated from the following equation,

$$L_{\text{X}} = 4\pi r^2 \int_{E_{\text{min}}}^{E_{\text{max}}} F_{\text{X,in}}(E, r) E dE \text{ [erg s}^{-1}\text{]} \quad (2)$$

$$= 4\pi r^2 \int_{E_{\text{min}}}^{E_{\text{max}}} F_0(r) \exp(-E/kT_{\text{X}}) E dE \text{ [erg s}^{-1}\text{]}, \quad (3)$$

where L_{X} is the X-ray luminosity of the central protostar. The local (attenuated) X-ray flux per unit energy $F_{\text{X}}(E, r)$ is given by the following equation,

$$F_{\text{X}}(E, r) = F_{\text{X,in}}(E, r) \exp(-\tau(E, r)), \quad (4)$$

where $\tau(E, r)$ is the total optical depth from the central protostar position to r . The energy-integrated total attenuated X-ray flux $F_{\text{X}}(r)$ at radius r of the envelope is given by the following equation,

$$F_{\text{X}}(r) = \int_{E_{\text{min}}}^{E_{\text{max}}} F_{\text{X}}(E, r) E dE \text{ [erg s}^{-1} \text{ cm}^{-2}\text{]}. \quad (5)$$

$\tau(E, r)$ is determined by the following equation,

$$\tau(E, r) = \tau_{\text{p}}(E, r) + \tau_{\text{c}}(E, r), \quad (6)$$

where $\tau_{\text{p}}(E, r)$ and $\tau_{\text{c}}(E, r)$ are the optical depths determined by photoabsorption and incoherent Compton scattering of hydrogen (Nomura et al. 2007). We note that the attenuation of the X-rays is mainly determined by photoabsorption especially at $E < 10$ keV, and the influence of Compton scattering of hydrogen on the chemistry is negligible (Stauber et al. 2005; Bruderer et al. 2009).

Assuming that the photoabsorption cross section of an atom is equal to its photoionization cross section, $\tau_{\text{p}}(E, r)$ is obtained by the following equation,

$$\tau_{\text{p}}(E, r) = N_{\text{H}}(r) \sigma_{\text{tot,p}}(E) = N_{\text{H}}(r) \sum_i x(i) \sigma_{i,\text{p}}(E), \quad (7)$$

where $N_{\text{H}}(r)$ is the total hydrogen column density from the central protostar position to r , $\sigma_{\text{tot,p}}(E)$ is the total photoabsorption cross section given by the sum of the photoionization cross sections for each element $\sigma_{i,\text{p}}(E)$ multiplied by its fractional abundance $x(i)$. We calculate the values of $\sigma_{i,\text{p}}(E)$ using the analytical method in Verner et al. (1993), as done in Walsh et al. (2012). $\tau_{\text{c}}(E, r)$ is obtained by the following equation,

$$\tau_{\text{c}}(E, r) = N_{\text{H}}(r) \sigma_{\text{c}}(E), \quad (8)$$

where $\sigma_{\text{c}}(E)$ is the incoherent Compton scattering cross section of hydrogen. We have adopted the values of $\sigma_{\text{c}}(E)$ from the NIST/XCOM database (Berger et al. 1999).

In Class I and II protostars, the values of observed X-ray luminosities are typically around $L_{\text{X}} \sim 10^{28} - 10^{31} \text{ erg s}^{-1}$ (Imanishi et al. 2001; Preibisch et al. 2005; Gudel & Naze 2009). However, the values of L_{X} in low-mass Class 0 protostars have not yet been well determined (e.g., Hamaguchi et al. 2005; Forbrich et al. 2006; Giardino et al. 2007; Gudel & Naze 2009; Kamezaki et al. 2014; Grosso et al. 2020), since the X-rays from the central Class 0 protostars are absorbed by their surrounding dense envelopes. Recently, Grosso et al. (2020) reported a powerful X-ray flare from the Class 0 protostar

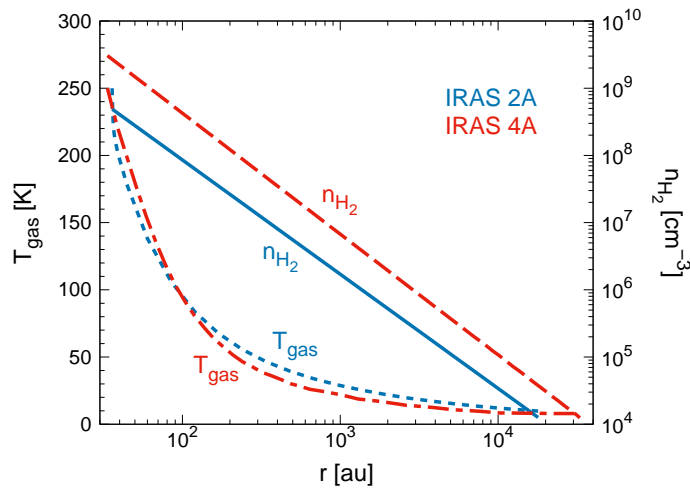


Fig. 1. The radial profiles of molecular hydrogen number densities n_{H_2} [cm^{-3}] and gas temperature T_{gas} [K] in NGC 1333-IRAS 2A and NGC 1333-IRAS 4A envelope models. The blue solid line and red dashed line show radial n_{H_2} profiles in IRAS 2A and IRAS 4A envelope models, respectively. The blue dotted line and red dashed dotted line show radial T_{gas} profiles in IRAS 2A and IRAS 4A envelope models, respectively.

HOPS 383 with $L_X \sim 4 \times 10^{31} \text{ erg s}^{-1}$ in the 2 – 8 keV energy band. Takasao et al. (2019) discussed from their simulations that protostar X-ray flares occur repeatedly (e.g., once in around 10 days) even in Class 0 protostars without magnetospheres. These flares are thought to occur when a portion of the large-scale magnetic fields, which are transported by accretion, are removed from the protostar as a result of magnetic reconnection. Stäuber et al. (2007) discussed the X-ray strengths from CN, CO^+ and SO^+ abundances, and they estimated that values of L_X in Class 0 low-mass protostars are around $10^{29} - 10^{32} \text{ erg s}^{-1}$, which are comparable to those in low-mass Class I protostars. However, Benz et al. (2016) discussed that the abundances of CN and CO^+ obtained by *Herschel*/HIFI observations can also be explained by FUV irradiation of outflow cavity walls (see also Bruderer et al. 2010), and suggested that the spatial resolution at scales of a few $\times 10^3$ au is not sufficient to detect molecular tracers of X-rays. Benz et al. (2016) also estimated the X-ray luminosities from the upper limits of H_3O^+ line fluxes obtained with *Herschel*/HIFI towards some low-mass protostars ($L_X < 10^{30} \text{ erg s}^{-1}$ in the Class 0 object IRAS16293-2422 and $L_X \gtrsim 10^{31} \text{ erg s}^{-1}$ in the Class I object TMC1).

In order to investigate the dependence of the chemical evolution on the strength of the X-ray field, we take values of $L_X = 0, 10^{27}, 10^{28}, 10^{29}, 10^{30}, 10^{31},$ and $10^{32} \text{ erg s}^{-1}$. We adopt $kT_X = 2.6 \text{ keV}$ ($= 3 \times 10^7 \text{ K}$), which is similar to Stäuber et al. (2006), and is also consistent with typical Class I protostars (Imanishi et al. 2001; Preibisch et al. 2005). We set $E_{\text{min}} = 0.1 \text{ keV}$ and $E_{\text{max}} = 100 \text{ keV}$ to cover a sufficient range of X-rays in our calculations. According to Maloney et al. (1996), Stäuber et al. (2005), and Bruderer et al. (2009), the shape of the X-ray spectrum will vary for different values of kT_X , with e.g., $10^7 - 10^8 \text{ K}$. However, they discussed that the calculated abundances differ only a factor of a few at most for the different X-ray temperatures, and that the influence of the X-ray luminosities on the chemistry is dominant. Note that we assume a constant value of X-ray luminosity during 10^5 year, since protostellar X-ray flares repeatedly occur and as a first step we would like to know the overall influence of X-ray fields on chemistry (see also Section 4.7).

In our calculations, the FUV radiation field from the central protostar is neglected. According to Stäuber et al. (2007), X-rays are suggested to be more effective for chemistry than FUV fields in the low-mass protostellar envelopes. Low-mass protostars ($L_{\text{bol}} \sim 10^{1-2} L_{\odot}$, $T_{\text{eff}} < 10^4 \text{ K}$) emit much less UV photons than high-mass protostars ($L_{\text{bol}} \sim 10^{4-5} L_{\odot}$, $T_{\text{eff}} \gtrsim$ a few $\times 10^4 \text{ K}$) due to their lower surface temperatures. Thus, FUV photons from the central source are not effective in destroying molecules in Class 0 protostellar envelopes (Stäuber et al. 2005, 2006). Some FUV radiation from the disk-star boundary can escape through outflow cavities, but only affects a narrow layer along the cavity walls (Visser et al. 2012).

The top panels of Figure 2 show the radial profiles of $F_X(r)$ in the IRAS 2A and IRAS 4A envelope models. In both models, the values of $F_X(r)$ in the innermost region are around $2 \times 10^{-4} \text{ erg s}^{-1} \text{ cm}^{-2}$ in the case of $L_X = 10^{27} \text{ erg s}^{-1}$, and around $20 \text{ erg s}^{-1} \text{ cm}^{-2}$ in the case of $L_X = 10^{32} \text{ erg s}^{-1}$. In the outer envelopes, the values of $F_X(r)$ reduce because of the increasing values of $N_{\text{H}}(r)$. Compared with the IRAS 2A model, $F_X(r)$ of the IRAS 4A model is lower in the outer regions due to higher densities (see also Figure 1). The values of $F_X(r)$ at $r \sim 10^3$ au are $\sim 1 \times 10^{-7} \text{ erg s}^{-1} \text{ cm}^{-2}$ (IRAS 2A) and $\sim 6 \times 10^{-8} \text{ erg s}^{-1} \text{ cm}^{-2}$ (IRAS 4A) in the case of $L_X = 10^{27} \text{ erg s}^{-1}$, and $\sim 1 \times 10^{-2} \text{ erg s}^{-1} \text{ cm}^{-2}$ (IRAS 2A) and $\sim 6 \times 10^{-3} \text{ erg s}^{-1} \text{ cm}^{-2}$ (IRAS 4A) in the case of $L_X = 10^{32} \text{ erg s}^{-1}$.

2.2. Calculations of chemical evolution

We calculate the chemical evolution of low-mass Class 0 protostellar envelopes using a detailed gas-grain chemical reaction network including X-ray induced chemical processes (Walsh et al. 2012, 2015). Note that Stäuber et al. (2005, 2006) focused on gas-phase water chemistry only. In order to investigate the radial dependence of the abundances of both gas and ice molecules on X-ray fields, we include gas-phase reactions, thermal and non-thermal gas-grain interactions, and grain-surface reactions, simultaneously.

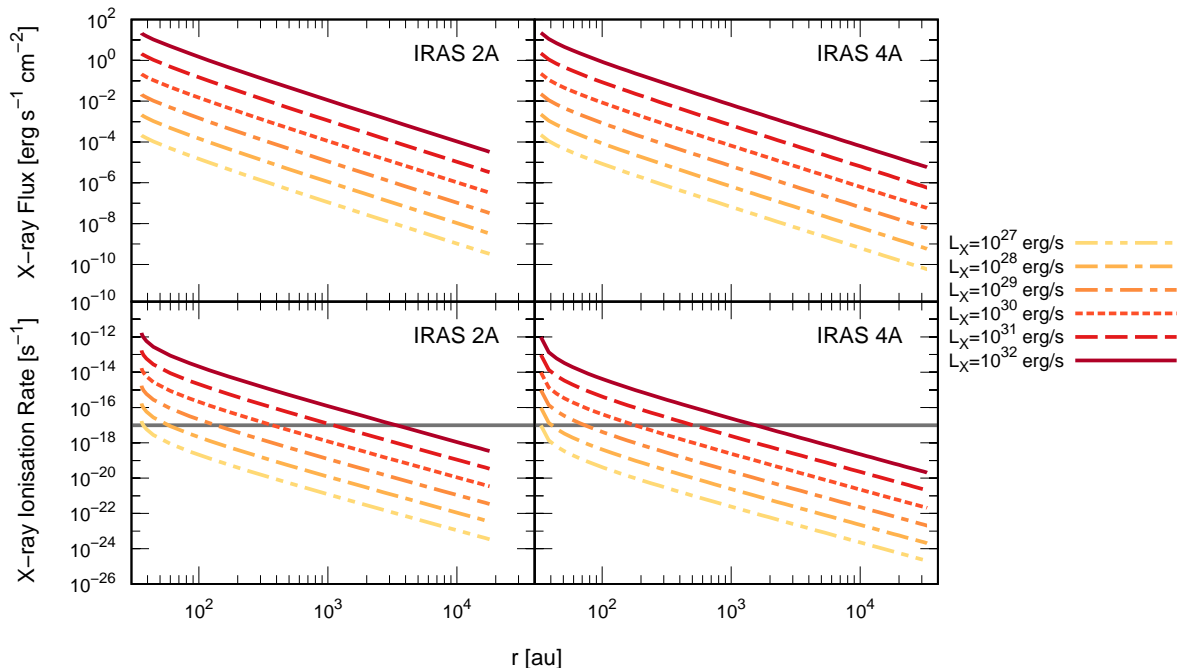


Fig. 2. [Top panels] The radial profiles of the X-ray flux $F_X(r)$ [$\text{erg s}^{-1} \text{cm}^{-2}$] in NGC 1333-IRAS 2A (top left panel) and NGC 1333-IRAS 4A (top right panel) envelope models. [Bottom panels] The radial profiles of the “secondary” X-ray ionization rate $\xi_X(r)$ [s^{-1}] in NGC 1333-IRAS 2A (bottom left panel) and NGC 1333-IRAS 4A (bottom right panel) envelope models. The horizontal gray solid lines show the assumed constant cosmic-ray ionization rate $\xi_{\text{CR}}(r) = 1.0 \times 10^{-17} \text{ s}^{-1}$. In all panels, the different line styles and colors in the radial $F_X(r)$ and $\xi_X(r)$ profiles denote models with different central star X-ray luminosities L_X .

The chemical network adopted in this work is based on the chemical model from Walsh et al. (2015), as also used in Eistrup et al. (2016, 2018), and Bosman et al. (2018b). The detailed background theories and procedures are also discussed in these papers and our previous works (e.g., Walsh et al. 2010, 2012, 2014a,b, Heinzeller et al. 2011, Notsu et al. 2016, 2017, 2018), although there are some differences between those studies and our paper. Here we provide a summary and describe important update of our adopted chemical network in this paper. Consistent with Stauber et al. (2006), the chemical evolution in envelopes is run for 10^5 years, which is the typical age of Class 0 protostars.

2.2.1. Gas-phase reactions

Our gas-phase chemistry is the complete network from the recent release of the UMIST Database for Astrochemistry (UDfA), termed “RATE12” which is publicly available⁵ (McElroy et al. 2013). RATE12 includes gas-phase two-body reactions, photodissociation and photoionisation, direct cosmic-ray ionisation, and cosmic-ray-induced photodissociation and photoionisation. Since the FUV radiation fields from the central protostar is ne-

glected in our calculations (see also Section 2.1.2), the photodissociation and photoionisation by FUV radiation is not included. In contrast, we have supplemented this gas-phase network with direct X-ray ionisation reactions, and X-ray-induced photoionisation and photodissociation processes (see Walsh et al. 2012, 2015, and Section 2.2.4 in this paper). In these X-ray induced photoreaction, UV photons are generated internally via the interaction of secondary electrons (produced by X-rays, see also Section 2.2.4) with H_2 molecules (Gredel et al. 1987, 1989). As in Walsh et al. (2015), we also add a set of three-body reactions and “Hot” H_2 chemistry, although they are not expected to be important at the densities and temperatures calculated in this study. Moreover, the gas phase chemical network is supplemented with reactions for important species, for example the CH_3O radical, that are not included in RATE12. The gas-phase formation and destruction reactions for these species are taken from the Ohio State University (OSU) network (Garrod et al. 2008).

2.2.2. Gas-grain interactions

In our calculations, we consider the freezeout of gas-phase molecules on dust grains, and the thermal and non-thermal desorption of molecules from dust grains (Hasegawa et al. 1992; Walsh et al. 2010, 2012, 2014a, 2015; Notsu et al.

⁵ <http://udfa.ajmarkwick.net>

Table 1. UV photodesorption yields

Species j	$Y_{\text{des}}(j)$ [molecules photon ⁻¹]	References
H ₂ O	*1.300 × 10 ⁻³	<i>a</i>
CO	2.700 × 10 ⁻³	<i>b, c</i>
CO ₂	2.300 × 10 ⁻³	<i>c, d</i>
N ₂	1.800 × 10 ⁻⁴	<i>b, c</i>
CH ₃ OH	*2.475 × 10 ⁻⁴	<i>e</i>
All other species	1.000 × 10 ⁻³	<i>f, g</i>

References. ^aÖberg et al. (2009b); ^bÖberg et al. (2007); ^cÖberg et al. (2009a); ^dFillion et al. (2014); ^eBertin et al. (2016); ^fWalsh et al. (2015); ^gCuppen et al. (2017);

* For H₂O and CH₃OH, the values of $Y_{\text{des}}(j)$ are the sum of all of their fragmentation pathways (see texts in Section 2.2.2).

2016). The adopted non-thermal desorption mechanisms are cosmic-ray-induced (thermal) desorption (Leger et al. 1985; Hasegawa & Herbst 1993; Hollenbach et al. 2009), reactive desorption (see Section 2.2.3), and photodesorption. We note that the direct cosmic-ray-induced desorption have no significant impact on chemistry, since its reaction timescale is typically much longer ($\gg 10^7$ years) than the age of protostars (Hollenbach et al. 2009).

We include photodesorption by both external X-ray photons and UV photons generated internally via the interaction of secondary electrons produced by cosmic-rays with H₂ molecules. Following Walsh et al. (2015), we assume compact spherical grains with a radius a of 0.1 μm and a fixed density of $\sim 10^{-12}$ relative to the gas number density. We adopt a value for the integrated cosmic-ray-induced UV photon flux as 10^4 photons $\text{cm}^{-2} \text{s}^{-1}$ (Prasad & Tarafdar 1983; Walsh et al. 2014a). We scale the internal UV photon flux by the cosmic-ray ionisation rate.

We use experimentally determined photodesorption yields, $Y_{\text{des}}(j)$, where available (e.g., Öberg et al. 2007, 2009a,b; Bertin et al. 2016; Cuppen et al. 2017). Such experiments were conducted by using UV lamps that mimic well the FUV radiation field (such as 100–200 nm) produced locally by H₂ emission excited by cosmic-rays or X-rays. For all species without experimentally determined photodesorption yields, a value of 10^{-3} molecules photon⁻¹ is used. The values of photodesorption yields adopted in our work are the same as those in Walsh et al. (2015), except the value of CH₃OH. Recent studies into methanol ice photodesorption showed that methanol does not desorb intact at low temperatures (e.g., Bertin et al. 2016; Cruz-Diaz et al. 2016), and the value of intact photodesorption yield for CH₃OH are considered to be much lower ($\sim 10^{-6} - 10^{-5}$) than that in the previous estimates ($\sim 10^{-3}$, Öberg et al. 2009c). The values of photodesorption yields adopted in this work, $Y_{\text{des}}(j)$, are listed in Table 1. On the basis of Öberg et al. (2009b), Arasa et al. (2010, 2015), Bertin et al. (2016), Cruz-Diaz et al. (2016), and Walsh et al. (2018), we include the fragmentation pathways for water ice (50% H₂O and 50% OH+H) and methanol photodesorption (e.g., 85.0% CO+H₂+H₂, 6.1% CH₃OH, 4.85% H₂CO+H₂, 3.0% CH₃+OH). The values of $Y_{\text{des}}(j)$ for H₂O and CH₃OH listed in Table 1 are the sum of all of these fragmentation pathways. The adopted value of intact photodesorption yield for CH₃OH is 1.5×10^{-5} [molecules photon⁻¹] and 6.1% of $Y_{\text{des}}(j)$

for CH₃OH.

As in Walsh et al. (2014a), we treat X-ray induced photodesorption as we treat UV photodesorption, and assume the same photodesorption yields for both X-ray induced photodesorption and UV photodesorption. In addition, following Walsh et al. (2014a), we do not include the photodesorption by UV photons generated internally via the interaction of secondary electrons produced by X-rays with H₂ molecules. This is because experimental constraints for X-ray induced photodesorption are limited, and the interaction of X-ray photons with ice is still not well understood (for more details, see e.g., Andrade et al. 2010; Walsh et al. 2014a). In Sections 4.2 and 4.3, we discuss the rates of X-ray induced photodesorption in detail, with conducting additional test calculations. We note that we also allow X-rays to photodissociate grain mantle material (see also Section 2.2.3 and Walsh et al. 2014a), in which UV photons are generated internally via the interaction of secondary electrons (produced by X-rays, see Section 2.2.4) with H₂. Recently, Dupuy et al. (2018) and Basalgète et al. (2021a,b) experimentally investigated X-ray induced photodesorption rates of H₂O, O₂, CH₃OH, and other related molecules (for more details, see Section 4.3).

The sticking coefficient is assumed to be 1 for all species, except for H that leads to H₂ formation (for more details, see Appendix B.2 of Bosman et al. 2018b). Compared with Walsh et al. (2015), the values of molecular binding energies, $E_{\text{des}}(j)$, are updated on the basis of the recent extensive literature review performed by Penteado et al. (2017) and grain-surface chemistry review by Cuppen et al. (2017). The values of binding energies for several important molecules, $E_{\text{des}}(j)$, are listed in Table 2.

2.2.3. Grain-surface reactions

For the grain-surface reactions, we use the reactions included in the Ohio State University (OSU) network (Garrod et al. 2008). In addition to grain-surface two-body reactions and reactive desorptions, grain-surface cosmic-ray-induced and X-ray-induced photodissociations are also included in our calculations (Garrod et al. 2008; Walsh et al. 2014a, 2015). In these X-ray induced photodissociation reactions, UV photons are generated internally via the interaction of secondary electrons (produced by X-rays, see also Section 2.2.4) with H₂ molecules (Gredel et al. 1987, 1989). In addition, as Walsh et al. (2018) adopted, we include an extended grain-surface chemistry network for methanol and its related compounds from Woods et al. (2013) and Chuang et al. (2016). Moreover, we have also added the hydrogenation abstraction pathway during hydrogenation from HNCO to NH₂CHO (Noble et al. 2015). As in Walsh et al. (2015) and Bosman et al. (2018b), the additional water formation routes studied by Cuppen et al. (2010) and Lamberts et al. (2013) are also included. The grain-surface two-body reaction rates are calculated assuming the Langmuir-Hinshelwood mechanism only, and using the rate equation method as described in Hasegawa et al. (1992). Only the top two monolayers of the ice mantle are chemically “active”. We assume that the size of the barrier to surface diffusion is $0.3 \times E_{\text{des}}(j)$ (Walsh et al. 2015). For the lightest reactants, H and H₂, we adopt either the classical diffusion rate or the quantum tunnelling rate depending on which is fastest (Hasegawa et al. 1992; Bosman et al. 2018b). For the latter quantum tunnelling rates, we adopt a rectangular barrier

of width 1.0 Å (Hasegawa et al. 1992; Bosman et al. 2018b). As in Bosman et al. (2018b), reaction-diffusion competition for grain-surface reactions with a reaction barrier (Garrod & Pauly 2011) is not included.

We note that grain-surface reactions take place on finite grain surfaces, where the populations of certain chemical species can become very small, i.e., $\ll 1$. If surface reactions occur very quickly in such a regime (the stochastic limit situation), the reaction rates might be overestimated compared with the actual values (Garrod 2008; Garrod & Pauly 2011; Cuppen et al. 2017). Such stochastic effects would be more important on the smaller dust grains (such as $a \lesssim 0.1 \mu\text{m}$), since the number of surface sites per grain is smaller (Barzel & Biham 2007; Garrod 2008). Stantcheva & Herbst (2004) and Vasyunin et al. (2009) showed that the stochastic effects are most important on chemical evolution in moderately warm regions ($T_{\text{dust}} \sim 30 \text{ K}$), and that the abundances of molecules such as H_2O and CO_2 can differ by more than an order of magnitude. In contrast, they also showed that such effects are not important in the regions with low ($T_{\text{dust}} \lesssim 10 \text{ K}$) and high ($T_{\text{dust}} \gtrsim 50 \text{ K}$) temperatures (see also Caselli et al. 1998). Comparing with the physical structures shown in Figure 1, the molecular abundances just outside the water snowline ($r \sim (1\text{--}a \text{ few}) \times 10^2 \text{ au}$) will not be strongly influenced by such effects. In addition, sizes of dust grains in protostellar envelopes are on average larger than $0.1 \mu\text{m}$ (Ormel et al. 2009; Miotello et al. 2014; Li et al. 2017), and thus the effects would be smaller than those in diffuse clouds. The micro- and macroscopic Monte Carlo techniques would be helpful for much more precise treatment of the grain-surface chemistry (e.g., Tielens & Hagen 1982; Vasyunin et al. 2009; Vasyunin & Herbst 2013; Garrod et al. 2009; Cuppen et al. 2017).

2.2.4. X-ray ionisation rates

We include a set of gas-phase and grain-surface X-ray-induced reactions which we duplicate from the existing set of cosmic-ray-induced reactions contained in RATE12 (McElroy et al. 2013; Walsh et al. 2015). The reaction rates are estimated by scaling the cosmic-ray-induced reaction rates by the ratio of the local X-ray ionization rate $\xi_X(r)$ and cosmic-ray ionisation rate $\xi_{\text{CR}}(r)$.

In this study, we calculate the “secondary” X-ray ionization rate at each radius $\xi_X(r)$ by the following equation (see also Glassgold et al. 1997; Walsh et al. 2012),

$$\xi_X(r) = \sum_i \int_{E_i}^{E_{\text{max}}} x(i) \sigma_{i,p}(E) F_X(E, r) \left[\frac{E - E_i}{\Delta\epsilon} \right] dE \quad [\text{s}^{-1}], \quad (9)$$

where E_i is the ionization potential for each element i . $x(i)$, $\sigma_{i,p}(E)$, and $F_X(E, r)$ are determined as described in Section 2.1.2. The number of secondary ionizations per unit energy produced by primary photoelectrons is given by the expression $(E - E_i)/\Delta\epsilon$, where $\Delta\epsilon = 37 \text{ eV}$ is the mean energy required to make an ion pair. X-rays interact only with atoms, regardless of whether an atom is bound within a molecule or free (Glassgold et al. 1997). According to Maloney et al. (1996), these “secondary” ionization rates $\xi_X(r)$ dominate the total ionization rates in X-ray dissociation regions. For atoms heavier than Li, inner-shell ionization is followed by the Auger effect, in which the excited, photo-produced ion undergoes two- or even three-electron decay (Glassgold et al. 1997). Our calculations

do not include the Auger effect. According to Igea & Glassgold (1999) and Stauber et al. (2005), Auger electrons, as well the primary photoelectron, are negligible compared to the secondary electrons for the ionization of the gas.

In this study, we adopt a constant value for the cosmic-ray ionisation rate of $\xi_{\text{CR}}(r) = 1.0 \times 10^{-17} \text{ s}^{-1}$ at all radii (Umebayashi & Nakano 2009). The bottom panels of Figure 2 show the radial profiles of the X-ray ionisation rate $\xi_X(r)$ in the IRAS 2A and IRAS 4A envelope models. In both models, the values of $\xi_X(r)$ in the innermost region are around 10^{-17} s^{-1} in the case of $L_X = 10^{27} \text{ erg s}^{-1}$, and around 10^{-12} s^{-1} in the case of $L_X = 10^{32} \text{ erg s}^{-1}$. In the outer envelopes, the values of $\xi_X(r)$ are reduced because of increasing values of $N_{\text{H}}(r)$. Compared with the IRAS 2A model, $\xi_X(r)$ of the IRAS 4A model is lower in the outer regions due to higher densities (see also Figure 1). The values of $\xi_X(r)$ at $r \sim 10^3 \text{ au}$ are $\sim 10^{-21} \text{ s}^{-1}$ (IRAS 2A) and $\sim 10^{-22} \text{ s}^{-1}$ (IRAS 4A) in the case of $L_X = 10^{27} \text{ erg s}^{-1}$, and $\sim 10^{-16} \text{ s}^{-1}$ (IRAS 2A) and $\sim 10^{-17} \text{ s}^{-1}$ (IRAS 4A) in the case of $L_X = 10^{32} \text{ erg s}^{-1}$. In regions with $\xi_X(r) > \xi_{\text{CR}}(r)$ ($= 1.0 \times 10^{-17} \text{ s}^{-1}$), X-ray induced photoionisation and photodissociation processes are considered to be dominant compared with cosmic-ray induced photoionisation and photodissociation processes. In the cases of $L_X \gtrsim 10^{31} \text{ erg s}^{-1}$, the values of $\xi_X(r)$ are larger than that of $\xi_{\text{CR}}(r)$ at $r \lesssim 10^3 \text{ au}$ in the IRAS 2A model and $r \lesssim 5 \times 10^2 \text{ au}$ in the IRAS 4A model. Inside the water snowline ($r < 10^2 \text{ au}$), the values of $\xi_X(r)$ are larger than that of $\xi_{\text{CR}}(r)$ in the cases of $L_X > 10^{29} \text{ erg s}^{-1}$ for IRAS 2A and $L_X > 10^{30} \text{ erg s}^{-1}$ for IRAS 4A.

We have also included the direct (“primary”) X-ray ionization of elements. The reaction rate $\xi_{\text{PX},i}(r)$ for each element i is given by the following equation (Verner et al. 1993; Walsh et al. 2012),

$$\xi_{\text{PX},i}(r) = \int_{E_i}^{E_{\text{max}}} \sigma_{i,p}(E) F_X(E, r) dE \quad [\text{s}^{-1}]. \quad (10)$$

2.2.5. Initial abundances

To generate a set of initial abundances for input into protostellar envelope models, we run a dark cloud model ($T_{\text{gas}} = T_{\text{dust}} = 10 \text{ K}$, $n_{\text{H}_2} = 10^4 \text{ cm}^{-3}$, $\xi_{\text{CR}}(r) = 1.0 \times 10^{-17} \text{ s}^{-1}$). As Walsh et al. (2015) adopted, the values of volatile elemental abundances for O, C, and N are 3.2×10^{-4} , 1.4×10^{-4} , and 7.5×10^{-5} relative to total hydrogen nuclei density, respectively. These values are based on diffuse cloud observations (Cardelli et al. 1991, 1996; Meyer et al. 1998). For other elements, we use the low-metal elemental abundances from Graedel et al. (1982). In this way, we begin the envelope calculations with an ice reservoir on the grain mantle built up in the dark-cloud and pre-stellar core phases. We use initial abundances at a time of 3.2×10^5 years on the basis of Walsh et al. (2015) and Drozdovskaya et al. (2016), except for the values of O gas, O_2 gas, and H_2O ice, which allow we treat as free parameters in our study but such that elemental oxygen abundance is preserved of 3.2×10^{-4} . This time scale of 3.2×10^5 years is consistent with the observed pre-stellar core lifetime of $\sim (2 - 5) \times 10^5$ years (Enoch et al. 2008).

In the above calculation under the dark cloud condition, the abundances with respect to total hydrogen nuclei density of O gas, O_2 gas, and H_2O ice at a time of 3.2×10^5 years are 8.5×10^{-5} , 2.2×10^{-6} , and 1.1×10^{-4} . If we consider longer time evolution ($\gtrsim 10^6$ years), however, the abundances of

Table 2. Initial abundances for dominant molecules in our protostellar envelope models and their binding energies

Species j	$n_{j,\text{gas}}/n_{\text{H}}$	$n_{j,\text{ice}}/n_{\text{H}}$	$E_{\text{des}}(j)$ [K]
H	3.807×10^{-5}	4.458×10^{-17}	650 ^a
H ₂	4.997×10^{-1}	4.140×10^{-5}	430 ^b
H ₂ O	7.080×10^{-7}	1.984×10^{-4}	4880 ^c
O	0.0	2.073×10^{-13}	1660 ^d
O ₂	0.0	4.035×10^{-12}	898 ^e
OH	5.164×10^{-8}	6.019×10^{-14}	3210 ^d
C	2.571×10^{-8}	1.310×10^{-16}	715 ^f
CO	7.532×10^{-5}	2.946×10^{-5}	855 ^g
CO ₂	7.487×10^{-7}	2.856×10^{-7}	2267 ^e
HCO ⁺	3.553×10^{-9}	—	—
CH ₄	1.120×10^{-6}	7.384×10^{-6}	1252 ^h
CH ₃ OH	3.558×10^{-9}	6.027×10^{-7}	3820 ⁱ
H ₂ CO	1.108×10^{-7}	8.437×10^{-6}	3260 ^e
C ₂ H	1.776×10^{-10}	5.537×10^{-17}	1330 ^f
C ₂ H ₂	7.440×10^{-8}	3.291×10^{-10}	2090 ⁱ
N	2.105×10^{-5}	5.531×10^{-14}	715 ^f
N ₂	9.765×10^{-6}	5.411×10^{-6}	790 ^g
NH ₃	2.933×10^{-7}	1.327×10^{-5}	2715 ⁱ
CN	3.016×10^{-9}	1.406×10^{-15}	1355 ^f
HCN	7.718×10^{-8}	2.772×10^{-6}	3610 ^f

References. ^aAl-Halabi & van Dishoeck (2007); ^bAcharyya (2014); ^cDulieu et al. (2013); ^dHe et al. (2014), He & Vidali (2014); ^eNoble et al. (2012); ^fAverage between Hasegawa & Herbst (1993) and Aikawa et al. (1996) values; ^gÖberg et al. (2005); ^hSmith et al. (2016); ⁱEstimated from Collings et al. (2004)

O gas and O₂ gas become much smaller ($\ll 10^{-6}$, see also Yıldız et al. 2013; Taquet et al. 2018) and the abundance of H₂O ice becomes larger ($\sim 2 \times 10^{-4}$, see also Schmalzl et al. 2014).

Previous chemical calculations (e.g., Walsh et al. 2015; Eistrup et al. 2016, 2018; Drozdovskaya et al. 2016) adopted a similarly high abundance for H₂O ice ($\sim (1-3) \times 10^{-4}$), and low or zero abundances for O and O₂ gas as initial conditions. Thus here we assume that all oxygen atoms in these three species are incorporated into H₂O ice ($= 1.984 \times 10^{-4}$).

Observations show that H₂O ice is indeed a major oxygen carrier in dark clouds and pre-stellar cores, although measured water ice abundances are consistently a factor of 2–4 below the expected value of 2×10^{-4} if all volatile oxygen that is not contained in CO is in water ice (Öberg et al. 2011; Boogert et al. 2015). Chemical modeling of Schmalzl et al. (2014) and Furuya et al. (2016) show that the water ice abundance in pre-stellar cores increases with pre-collapse time (see also van Dishoeck et al. 2021), and that such a low water ice abundance can only be obtained for a short pre-stellar period. At pre-collapse times of $t_{\text{pre}} < 10^6$ years, a considerable amount of oxygen is also found in other oxygen bearing species (mainly O besides CO). At $t_{\text{pre}} \gtrsim 10^6$ years, oxygen returns into the water network and water ice then becomes dominant oxygen reservoir (up to $\sim 2 \times 10^{-4}$) with CO.

The observed low water ice abundances with respect to hydrogen nuclei of low-mass protostellar envelopes of $\sim (3-8) \times 10^{-5}$ would require short pre-collapse lifetimes of $t_{\text{pre}} \lesssim 10^5$ years (Schmalzl et al. 2014), less than the observed pre-stellar core

lifetimes of $\sim (2-5) \times 10^5$ years (Enoch et al. 2008). In addition, this shorter pre-collapse phase is inconsistent with the discussions in Yıldız et al. (2013) who argued for a long pre-collapse phase of at least 10^6 years to explain the lower upper limit of gas-phase cold O₂ abundances ($\ll 10^{-6}$) towards IRAS 4A (see also Taquet et al. 2018). Possible mitigations of this conundrum include the possibility that a fraction of water ice is locked up in larger micron-sized grains that do not contribute to the infrared water ice bands, or the presence of some amount of “Unidentified Depleted Oxygen (UDO)” which has also been invoked to explain the oxygen budget in diffuse clouds (Whittet 2010; Schmalzl et al. 2014; van Dishoeck et al. 2021). Here we do not consider either of these two options.

The fractional abundances with respect to total hydrogen nuclei density for dominant and important molecules, which are used as initial abundances in our protostellar envelope models, are listed in Table 2.

3. Results

3.1. Water fractional abundances

Figure 3 shows the radial profiles of the water gas fractional abundances with respect to total hydrogen nuclei densities $n_{\text{H}_2\text{O}}/n_{\text{H}}$ in IRAS 2A (left panels) and IRAS 4A (right panels) envelope models, for the various X-ray luminosities ($L_X=0, 10^{27}, 10^{28}, 10^{29}, 10^{30}, 10^{31}$, and 10^{32} erg s⁻¹). Figure 4 shows the radial profiles of water ice fractional abundances $n_{\text{H}_2\text{O,ice}}/n_{\text{H}}$ in the same models. In both models, the water snowline positions are at $r \sim 10^2$ au, where T_{gas} is around 100 K.

For $L_X = 0$ erg s⁻¹, water gas abundances are around 2×10^{-4} inside the water snowline ($T_{\text{gas}} > 10^2$ K, $r < 10^2$ au), and sharply decrease to $\lesssim 10^{-10}$ just outside the water snowline ($T_{\text{gas}} < 10^2$ K, $r > 10^2$ au). The water gas abundances increase in the outer low density envelopes ($n_{\text{H}_2\text{O}}/n_{\text{H}} \sim 10^{-7}$ at $r \sim 10^4$ au), since in this region the water abundances are mainly determined by the balance between freeze-out of water vapor and cosmic-ray induced photodesorption of water ice, which maintains an approximately constant number density of gas phase water (for more details, see Schmalzl et al. 2014).

Outside the water snowline, for $L_X \gtrsim 10^{30}$ erg s⁻¹, water gas abundances become higher (up to $n_{\text{H}_2\text{O}}/n_{\text{H}} \sim 10^{-8} - 10^{-7}$), compared with the values ($n_{\text{H}_2\text{O}}/n_{\text{H}} \sim 10^{-10}$) for $L_X \lesssim 10^{27}$ erg s⁻¹ in IRAS 2A and $L_X \lesssim 10^{28}$ erg s⁻¹ in IRAS 4A. In addition, water ice abundances (see Figure 4) are around 2×10^{-4} outside the water snowline for $L_X \lesssim 10^{30}$ erg s⁻¹, and they become much lower (below to $n_{\text{H}_2\text{O}}/n_{\text{H}} \sim 10^{-8}$ at a few $\times 10^2$ au) for $L_X \gtrsim 10^{31}$ erg s⁻¹. We conclude that photodesorption by external X-ray photons (e.g., Walsh et al. 2015; Cuppen et al. 2017; Dupuy et al. 2018) is important in this region (see also Sections 4.2 and 4.3). This X-ray effect is stronger in the IRAS 2A model, since it has around a 3–6 times lower density and thus higher X-ray fluxes (see Figure 2) than the IRAS 4A model. The lower density in the IRAS 2A also decreases the efficacy of two-body ion-molecule reactions (see Appendix A where we demonstrate the effect of density only on the chemistry). Water gas abundances at $r \gtrsim 10^3$ au are also affected by strong X-ray fluxes, although $\xi_X(r)$ is smaller than $\xi_{\text{CR}}(r)$ in these regions. This is because at $r \gtrsim 10^3$ au the rates of the X-ray induced photodesorption of water ice are around 10^3 times larger than those of cosmic-ray induced photodesorption, and much larger

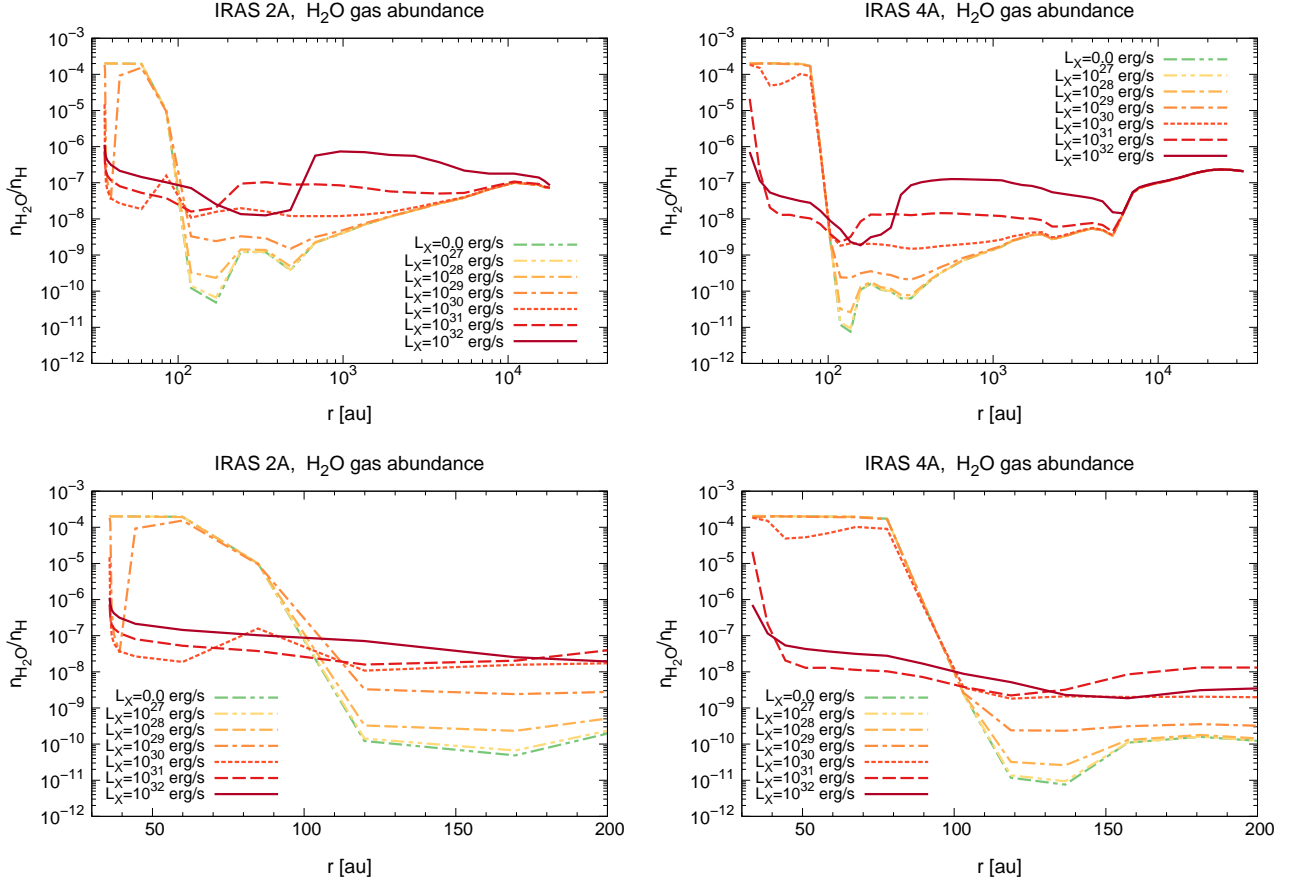


Fig. 3. [Top panels]: The radial profiles of water gas fractional abundances with respect to total hydrogen nuclei densities $n_{\text{H}_2\text{O}}/n_{\text{H}}$ in NGC 1333-IRAS 2A (left panel) and NGC 1333-IRAS 4A (right panel) envelope models. The double-dashed double-dotted lines, the dashed double-dotted lines, the double-dashed dotted lines, the dashed dotted lines, the dotted lines, the dashed lines, and the solid lines show radial $n_{\text{H}_2\text{O}}/n_{\text{H}}$ profiles for values of central star X-ray luminosities $L_X=0, 10^{27}, 10^{28}, 10^{29}, 10^{30}, 10^{31},$ and 10^{32} erg s $^{-1}$, respectively. The line colors gradually change from green to yellow, orange, red, and brown as the values of L_X increase. In Figures 5–7, C.1, C.2, D.1, E.1, H.1, and H.2, we adopt the same line type and color patterns of the calculated radial fractional abundance profiles of gas-phase molecules for different values of L_X . [Bottom panels]: The same radial profiles as shown in the top panels, but we enlarge the inner regions ($r < 200$ au) on a linear scale.

(> 10^{20} times) than that of thermal desorption and cosmic-ray induced (thermal) desorption. The chemical model adopted by Stauber et al. (2005, 2006) did not include non-thermal desorption processes, and thus they did not find this dependence of the gaseous water abundances on X-ray fluxes outside the water snowline.

Inside the water snowline ($T_{\text{gas}} > 10^2$ K, $r < 10^2$ au), for $L_X \lesssim 10^{29}$ erg s $^{-1}$ in IRAS 2A and $L_X \lesssim 10^{30}$ erg s $^{-1}$ in IRAS 4A, the gas maintains high water abundances of 10^{-4} , and they are the dominant oxygen carrier along with CO. On the other hand, for $L_X \gtrsim 10^{30}$ erg s $^{-1}$ in IRAS 2A and $L_X \gtrsim 10^{31}$ erg s $^{-1}$ in IRAS 4A, water gas abundances become much smaller just inside the water snowline ($T \sim 100 - 250$ K, below to $n_{\text{H}_2\text{O}}/n_{\text{H}} \sim 10^{-8} - 10^{-7}$) and in the innermost regions ($T \sim 250$ K, $n_{\text{H}_2\text{O}}/n_{\text{H}} \sim 10^{-6}$).

Within the water snowline, water sublimates from the dust-grain surfaces into the gas phase. According to Stauber et al. (2005, 2006), van Dishoeck et al. (2013, 2014) and Walsh et al. (2015), in the presence of X-rays, gas-phase water in this region is mainly destroyed with X-ray induced photodissociation (H+OH), and ion-molecule reactions (with, for example, HCO^+ ,

H^+ , H_3^+ , and He^+). For $L_X \gtrsim 10^{29}$ erg s $^{-1}$ in IRAS 2A and $L_X \gtrsim 10^{30}$ erg s $^{-1}$ in IRAS 4A, the X-ray ionization rates $\xi_X(r)$ are larger than our adopted cosmic ray ionization rate $\xi_{\text{CR}}(r)$ ($=1.0 \times 10^{-17}$ s $^{-1}$) within the water snowline (see Figure 2). Thus, these processes are important to explain the dependence on X-ray fluxes and number densities within the water snowline. Stauber et al. (2006) discussed that these ion-molecule reactions are more effective than X-ray-induced photodissociation, with resulting water gas abundances varying by less than 15% if they ignored the X-ray induced photodissociation. In our calculations, we also confirm that the reaction rates of these ion-molecule reactions are larger than those of the X-ray induced photodissociation leading to H+OH, and that the former reactions become more important compared with the latter reaction as the gas densities become larger (see also Appendix A).

At $r \sim 60$ au and for $L_X = 10^{32}$ erg s $^{-1}$ in the IRAS 2A model, the water gas abundance and $n_{\text{H}_2\text{O}}$ are 1.4×10^{-7} and 5.9×10^1 cm $^{-3}$ at $t = 10^5$ years, respectively, and the HCO^+ gas abundance and n_{HCO^+} ⁶ are 9.8×10^{-9} and 4.0 cm $^{-3}$ at $t = 10^5$ years,

⁶ n_{HCO^+} is the number density of HCO^+ and we obtain the value in Section 3.3 and Figure 6.

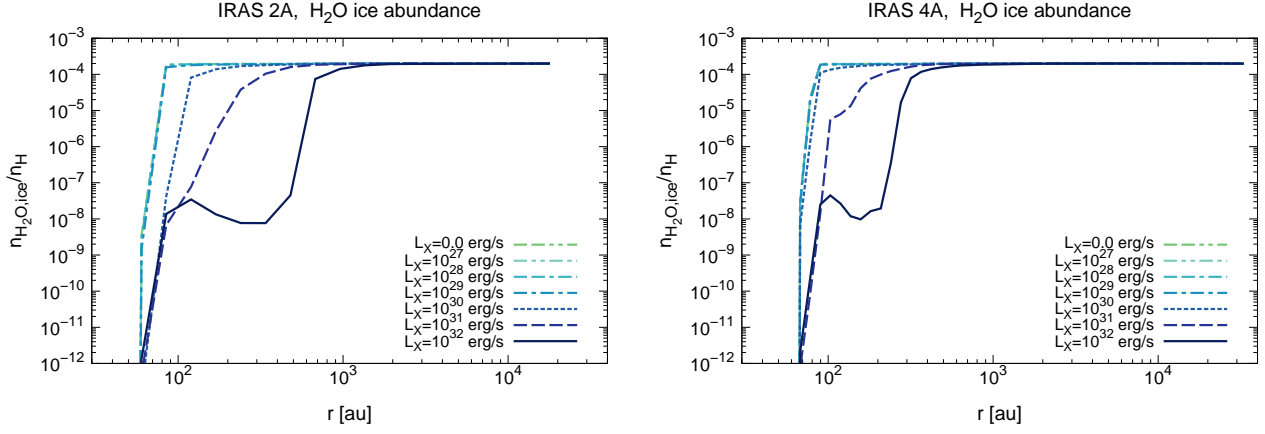


Fig. 4. The radial profiles of water ice fractional abundances $n_{\text{H}_2\text{O,ice}}/n_{\text{H}}$ in NGC 1333-IRAS 2A (left panel) and NGC 1333-IRAS 4A (right panel) envelope models. The line colors are gradually change from green to cyan, blue, and indigo as the values of L_X become large. The profiles for $L_X = 0 - 10^{29} \text{ erg s}^{-1}$ are almost overlapped. In Figures 7, C.1, and C.2, we adopt the same line type and color patterns of the radial fractional abundance profiles of icy-phase molecules for different values of L_X .

respectively. On the basis of these values, the rate coefficient of the ion-molecule reaction with $\text{H}_2\text{O} + \text{HCO}^+ \rightarrow \text{CO} + \text{H}_3\text{O}^+$, k_1 , is $\sim 3.7 \times 10^{-9} \text{ cm}^3 \text{ s}^{-1}$ (Adams et al. 1978), and the reaction rate, $R(1) = k_1 n_{\text{H}_2\text{O}} n_{\text{HCO}^+}$, is $\sim 8.7 \times 10^{-7} \text{ cm}^{-3} \text{ s}^{-1}$. In contrast, the rate coefficient of X-ray-induced photodissociation leading to $\text{H} + \text{OH}$, k_2 , is $\sim 8.6 \times 10^{-11} \text{ s}^{-1}$ (Gredel et al. 1989), and the reaction rate, $R(2) = k_2 n_{\text{H}_2\text{O}}$, is $\sim 5.1 \times 10^{-9} \text{ cm}^{-3} \text{ s}^{-1}$.

We note that for $L_X \gtrsim 10^{31} \text{ erg s}^{-1}$, abundances of HCO^+ within the water snowline ($\gtrsim 10^{-9}$, see Section 3.3) are larger than those of other molecular ions which are important to water gas destruction such as He^+ ($\lesssim 10^{-10}$). This makes HCO^+ the most important destructor of H_2O in highly ionized regions.

In the innermost high temperature region ($T_{\text{gas}} \sim 250 \text{ K}$), the following two-body reaction with the reaction barrier of 1736 K (Oldenberg et al. 1992),



becomes more efficient, and thus water gas abundances become relatively large ($n_{\text{H}_2\text{O}}/n_{\text{H}} \sim 10^{-6}$) even in the highest X-ray flux cases ($L_X = 10^{32} \text{ erg s}^{-1}$). As Stauber et al. (2005, 2006) noted, X-ray destruction processes are more effective in lower density models.

3.2. Molecular and atomic oxygen fractional abundances

Figure 5 presents the radial profiles of the fractional abundance of gaseous molecular oxygen $n_{\text{O}_2}/n_{\text{H}}$ (top panels) and atomic oxygen $n_{\text{O}}/n_{\text{H}}$ (bottom panels) in IRAS 2A (left panels) and IRAS 4A (right panels) envelope models, for the various X-ray luminosities. It is seen that the O_2 abundances at $r \lesssim 10^4 \text{ au}$ (IRAS 2A) and $r \lesssim 6 \times 10^3 \text{ au}$ (IRAS 4A), and the O abundance at $r \lesssim 10^3 \text{ au}$ increase (within each snowline position) as X-ray luminosities become larger. Both molecular and atomic oxygen are very volatile ($E_{\text{des}}(\text{O}) = 1660 \text{ K}$ and $E_{\text{des}}(\text{O}_2) = 898 \text{ K}$) compared with H_2O ($E_{\text{des}}(\text{H}_2\text{O}) = 4880 \text{ K}$), thus their snowline positions are located in the outer envelopes ($r > 5 \times 10^2 \text{ au}$).

Inside the water snowline, both molecular and atomic oxygen abundances are much lower ($< 10^{-8}$) in the cases of

low X-ray luminosities ($L_X \lesssim 10^{28} \text{ erg s}^{-1}$ in IRAS 2A and $L_X \lesssim 10^{29} \text{ erg s}^{-1}$ in IRAS 4A). In contrast, for moderate X-ray luminosities ($L_X \sim 10^{29} \text{ erg s}^{-1}$ in IRAS 2A and $L_X \sim 10^{30} \text{ erg s}^{-1}$ in IRAS 4A) and high X-ray luminosities ($L_X \gtrsim 10^{30} \text{ erg s}^{-1}$ in IRAS 2A and $L_X \gtrsim 10^{31} \text{ erg s}^{-1}$ in IRAS 4A), their abundances become larger, and reach about $\sim 5 \times 10^{-5} - 10^{-4}$ with $L_X \gtrsim 10^{31} \text{ erg s}^{-1}$. Compared with the water gas abundances, both molecular and atomic oxygen have opposite dependence on X-ray fluxes. Thus, the identity of the main volatile oxygen carrier in the inner regions is very sensitive to the X-ray flux from the central protostars (see also Section 4.1). In Sections 3.2-3.7 and 4.1, and Appendix C, D, and E, we adopted the same definition for the values of low, moderate and high X-ray luminosities.

According to Voitke et al. (2009) and Walsh et al. (2015), in the presence of X-rays, atomic oxygen is mainly produced by X-ray induced photodissociation of OH and CO. OH is efficiently produced by X-ray induced photodissociation and fragmental photodesorption of H_2O (see Section 3.4), and thus the O abundance becomes larger as X-ray fluxes become larger. In addition, as also discussed in Walsh et al. (2015) and Eistrup et al. (2016), molecular oxygen is formed in the gas-phase via the following reaction,



and is destroyed via photodissociation and reactions with C and H to yield CO and OH, respectively. Note that reaction (12) is a barrierless neutral-neutral reaction and has a negligible temperature dependence (Carty et al. 2006; Taquet et al. 2016b). Both the O and OH abundances become larger as X-ray fluxes become larger, and thus the O_2 abundances become larger, especially in the inner warm envelope where water is sublimated from dust grains.

3.3. HCO^+ fractional abundances

The top panels of Figure 6 show the radial profiles of the HCO^+ fractional abundances $n_{\text{HCO}^+}/n_{\text{H}}$ in IRAS 2A (left panel) and IRAS 4A (right panel) envelope models, for the various X-ray luminosities. According to our model, the HCO^+ abundances at

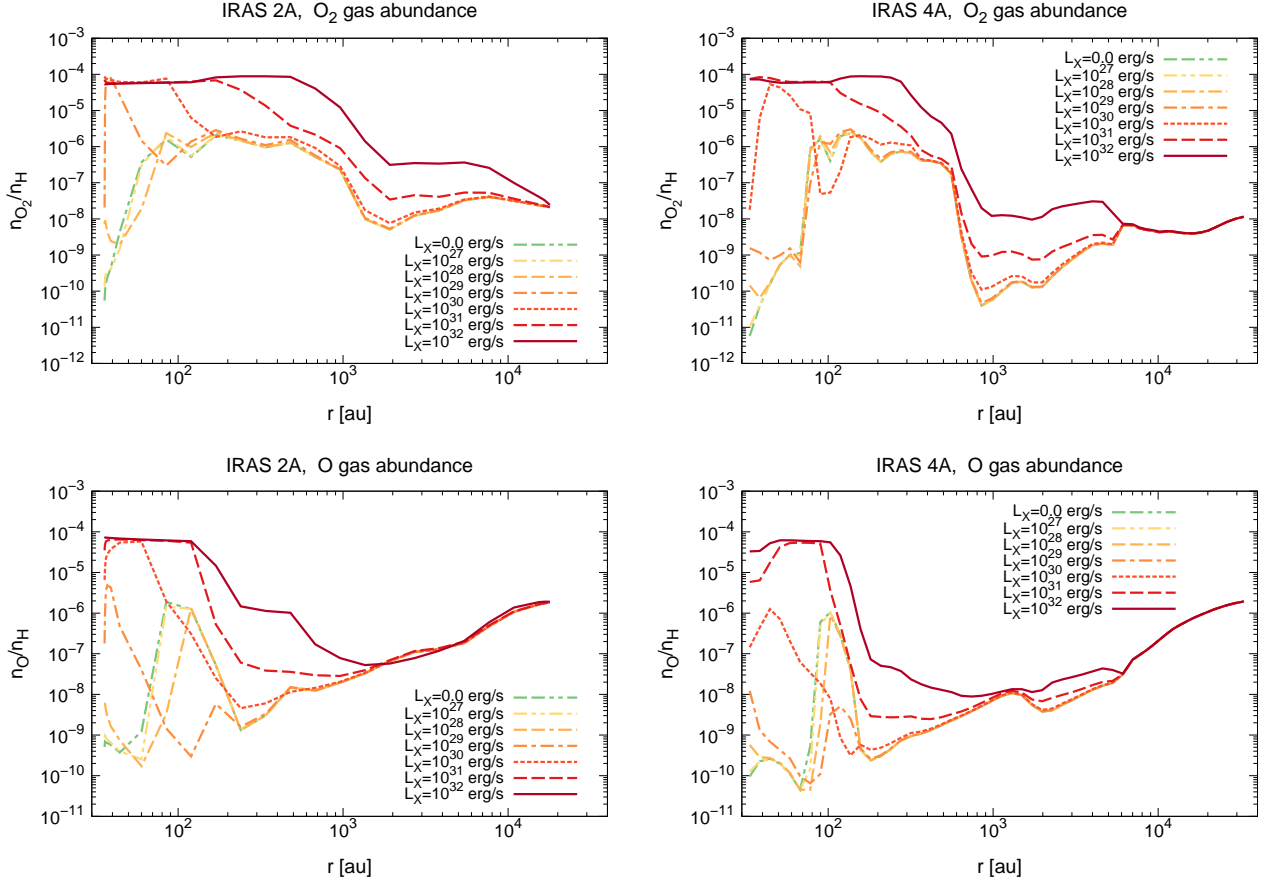


Fig. 5. [Top panels]: The radial profiles of molecular oxygen gas fractional abundances $n_{\text{O}_2}/n_{\text{H}}$ in NGC 1333-IRAS 2A (left panel) and NGC 1333-IRAS 4A (right panel) envelope models. [Bottom panels]: The radial profiles of atomic oxygen gas fractional abundances $n_{\text{O}}/n_{\text{H}}$ in the IRAS 2A (left panel) and IRAS 4A (right panel) envelope models.

$r \gtrsim 10^3$ au ($\sim 10^{-9} - 10^{-8}$ for IRAS 2A, and $\sim 10^{-10} - 10^{-9}$ for IRAS 4A) do not change with different X-ray luminosities. This is consistent with the input assumption that cosmic-ray ionization dominates at these radii (see Figure 2 and Section 4.6).

The HCO^+ abundances at $r \lesssim 10^3$ au are affected by strong X-ray fluxes. For low X-ray luminosities, HCO^+ abundances drop in the inner envelope, and reach $\lesssim 10^{-13}$ within the water snowline, due to the efficient destruction by water (see below). In contrast, for high X-ray luminosities, they become higher in the inner envelope, and reach more than 10^{-9} (for IRAS 2A) and 10^{-10} (for IRAS 4A) within water snowline. The overall HCO^+ abundances are larger and X-ray effects are also stronger in the IRAS 2A model, since it has around 3 – 6 times lower densities and thus higher X-ray fluxes than the IRAS 4A model has (see Figures 1 and 2, and Appendix A).

HCO^+ has been considered as a chemical tracer of the water snowline, since its most abundant destroyer in warm dense gas is water via the following reaction (Jørgensen et al. 2013; Visser et al. 2015; van ’t Hoff et al. 2018a; Hsieh et al. 2019; Lee et al. 2020; Leemker et al. 2021),



Thus, a strong decline in HCO^+ (and its isotopologue H^{13}CO^+) is expected within the water snowline. van ’t Hoff et al. (2018a)

conducted spherically symmetric physical-chemical modeling using the same IRAS 2A temperature and number density model which we adopt (see Section 2.1.1 and Figure 1). Their gas-grain chemical model included gas-phase cosmic-ray induced reactions, but did not include X-ray induced chemistry (see e.g., Taquet et al. 2014). They reported an increase of H^{13}CO^+ emission just outside the water snowline and a spatial anti-correlation of H^{13}CO^+ and H_2^{18}O emission in the envelope around IRAS 2A. The radial profiles of water and HCO^+ gas abundances in van ’t Hoff et al. (2018a) are similar to those in our model with $L_{\text{X}} \lesssim 10^{29}$ erg s $^{-1}$. On the basis of our modeling, for high X-ray luminosities, the water gas abundance sharply decreases inside the water snowline and thus HCO^+ is not efficiently destroyed. Formation of HCO^+ is dominated by the ion-molecule reaction between H_3^+ and CO (Schwarz et al. 2018; van ’t Hoff et al. 2018a; Leemker et al. 2021), and H_3^+ is mainly formed by the ionization of H_2 . Therefore, the HCO^+ abundances increase as the X-ray ionisation rate increases, and they have relatively radially flat profiles for high X-ray luminosities (see Figure 6). Thus, our work suggested that HCO^+ and its isotopologue H^{13}CO^+ lines cannot be used as tracers of the water snowline position if X-ray fluxes are high and inner water gas is absent. The X-ray ionisation rates $\xi_{\text{X}}(r)$ where HCO^+ loses its efficacy as a water snowline tracer are $\gtrsim 10^{-16}$ s $^{-1}$ (see Figure 2), which correspond $L_{\text{X}} \gtrsim 10^{30} - 10^{31}$ erg s $^{-1}$, depending on density structures.

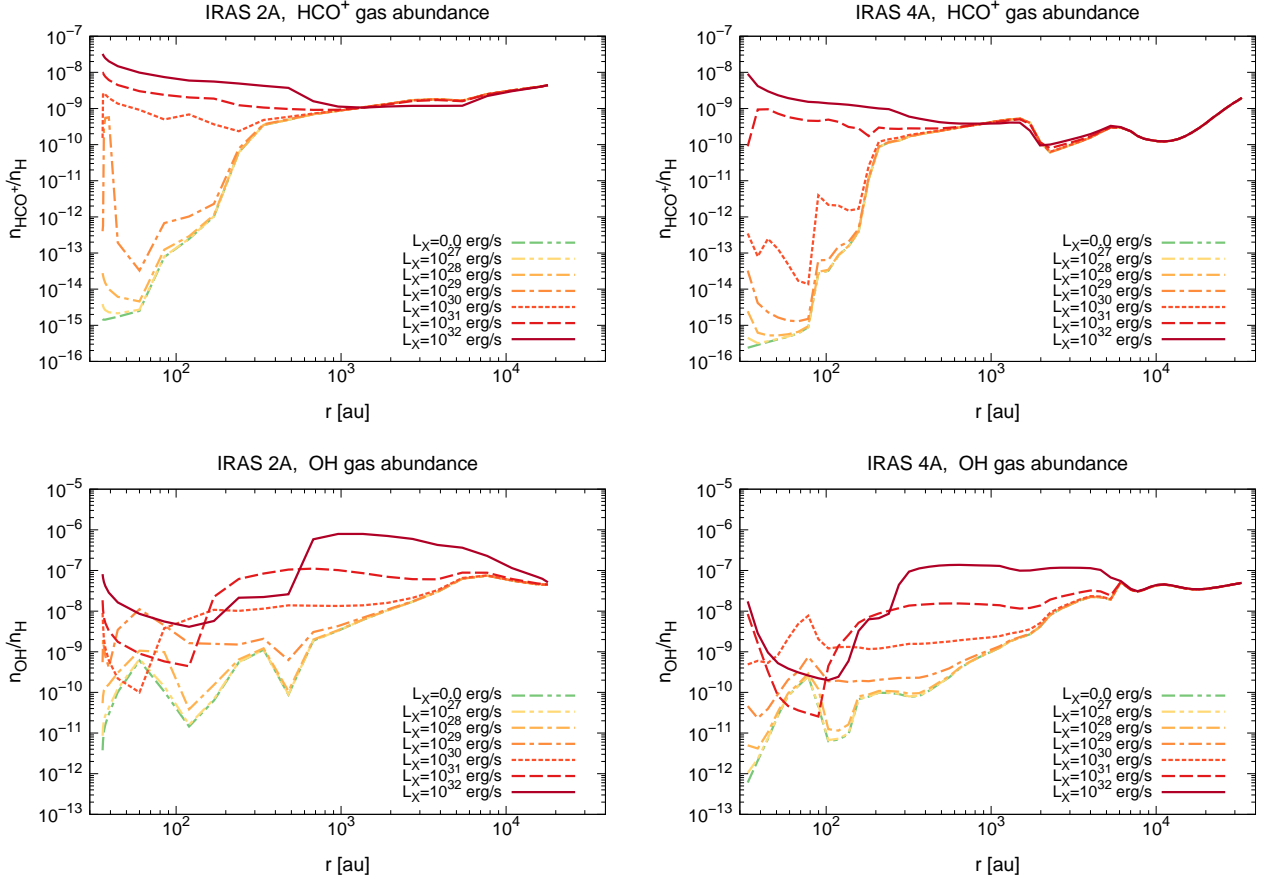


Fig. 6. [Top panels]: The radial profiles of HCO^+ gas fractional abundances $n_{\text{HCO}^+}/n_{\text{H}}$ in NGC 1333-IRAS 2A (left panel) and NGC 1333-IRAS 4A (right panel) envelope models. [Bottom panels]: The radial profiles of OH gas fractional abundances $n_{\text{OH}}/n_{\text{H}}$ in the IRAS 2A (left panel) and IRAS 4A (right panel) envelope models.

In Class II disks, HCO^+ and its isotopologues are considered to trace X-ray and high cosmic-ray ionisation rates with $\gtrsim 10^{-17} \text{ s}^{-1}$ in the disk surface (Cleeves et al. 2014). According to our calculations, HCO^+ is the dominant cation in the outer envelopes where the cosmic-ray ionisation is dominant (see Figure 2), and also in the inner envelopes if $\xi_{\text{X}}(r)$ is $\gtrsim 10^{-16} \text{ s}^{-1}$. Thus, in these cases HCO^+ line emission could be used to estimate the electron number densities and the ionization rates (see also van 't Hoff et al. 2018a and Section 4.6 of this paper).

3.4. OH fractional abundances

The bottom panels of Figure 6 show the radial profiles of the OH gas fractional abundances $n_{\text{OH}}/n_{\text{H}}$ in IRAS 2A (left panel) and IRAS 4A (right panel) envelope models, for the various X-ray luminosities. The OH abundances increase at $r \lesssim 10^4$ au as values of X-ray luminosities become larger. For low X-ray luminosities, the OH abundances are around $10^{-9} - 10^{-8}$ at $r \gtrsim 10^3$ au, and become lower in the inner envelopes ($\sim 10^{-10} - 10^{-9}$ at $r \sim 10^2$ au, and $\sim 10^{-12} - 10^{-11}$ at the inner edge). For moderate X-ray luminosities, the OH abundances become higher in the inner envelope, and reach more than 10^{-9} within water snowline. In addition, for high X-ray luminosities, the OH abundances are much higher at $r \sim 10^2 - 10^4$ au ($\sim 10^{-8} - 10^{-6}$), and become a bit lower ($\lesssim 10^{-8}$) around and just inside the water snowline ($\lesssim 10^2$ au).

OH is efficiently produced by X-ray induced photodissociation of H_2O gas and fragmental photodesorption of H_2O ice (see also Section 2.2.2), thus the OH abundances increase as the X-ray flux becomes larger (see Section 3.1 and Figure 3). The former X-ray induced photodissociation reaction is dominant within the water snowline, whereas the fragmental photodesorption reaction is dominant outside the water snowline where a large amount of water ice is present on the dust-grain surface. For example, at $r \sim 480$ au and $L_{\text{X}} = 10^{32} \text{ erg s}^{-1}$ in the IRAS 2A model, the rate coefficient of the former X-ray induced photodissociation reaction, k_3 , is $\sim 5.6 \times 10^{-13} \text{ s}^{-1}$ (Gredel et al. 1989; Heays et al. 2017), and the reaction rate, $R(3) = k_3 n_{\text{H}_2\text{O}}$, is $\sim 1 \times 10^{-13} \text{ cm}^{-3} \text{ s}^{-1}$ at $t = 10^5$ years. In contrast, the rate coefficient of the latter photodesorption reaction, k_4 , is $\sim 1.9 \times 10^{-9}$ (Öberg et al. 2009b; Walsh et al. 2015, see also Section 2.2.2), and the reaction rate, $R(4) = k_4 n_{\text{H}_2\text{O,ice}}$, is $\sim 1 \times 10^{-9} \text{ cm}^{-3} \text{ s}^{-1}$ at $t = 10^5$ years. As discussed in Sections 3.1 and 3.2, atomic oxygen is mainly produced by X-ray induced photodissociation of OH, and molecular oxygen is produced from OH in the gas phase ($\text{O} + \text{OH}$). Therefore, for high X-ray luminosities, the OH abundances decrease around and inside the water snowline where molecular and atomic oxygen abundances are high ($\sim 10^{-4}$).

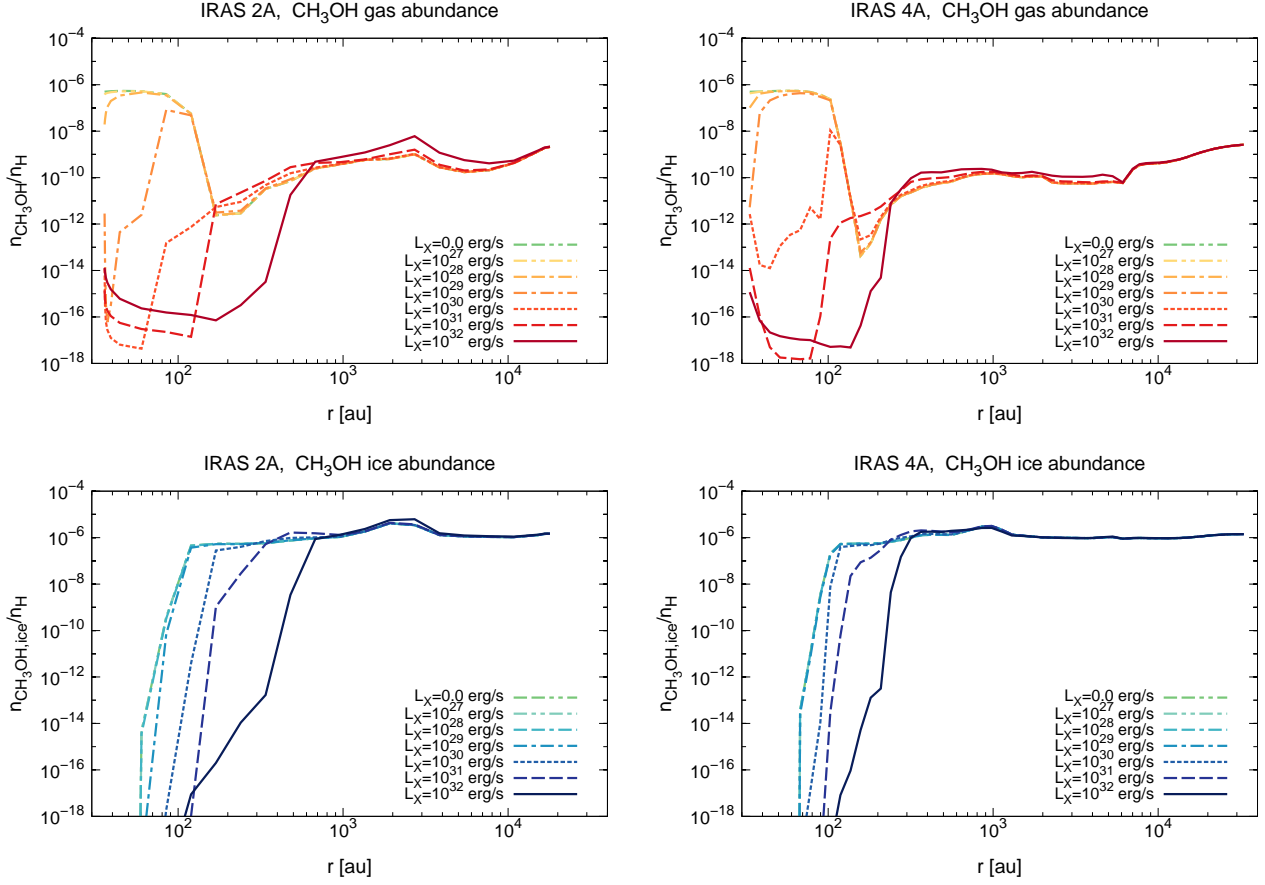


Fig. 7. The radial profiles of methanol gas and ice fractional abundances $n_{\text{CH}_3\text{OH}}/n_{\text{H}}$ (top panels) and $n_{\text{CH}_3\text{OH,ice}}/n_{\text{H}}$ (bottom panels) in NGC 1333-IRAS 2A (left panels) and NGC 1333-IRAS 4A (right panels) envelope models.

3.5. CH_3OH fractional abundances

Figure 7 shows the radial profiles of the methanol gas fractional abundances $n_{\text{CH}_3\text{OH}}/n_{\text{H}}$ and ice fractional abundances $n_{\text{CH}_3\text{OH,ice}}/n_{\text{H}}$ in IRAS 2A (left panel) and IRAS 4A (right panel) envelope models, for the various X-ray luminosities. According to Table 2, the binding energy of CH_3OH is somewhat smaller than that of H_2O ($E_{\text{des}}(\text{CH}_3\text{OH})=3820$ K and $E_{\text{des}}(\text{H}_2\text{O})=4880$ K), and the CH_3OH snowline position ($\sim 2 \times 10^2$ au) is located outside the water snowline ($\sim 10^2$ au). Thus, CH_3OH has been considered to probe the $\gtrsim 100$ K region in hot cores (Nomura & Millar 2004; Garrod & Herbst 2006; Herbst & van Dishoeck 2009; Taquet et al. 2014), and also provides an outer limit to the water snowline position in protostellar envelopes (e.g., Jørgensen et al. 2013; van 't Hoff et al. 2018b; Lee et al. 2019, 2020).

The CH_3OH abundances within $r \lesssim 200$ au decrease as the values of X-ray luminosities become larger. Outside the CH_3OH snowline, CH_3OH gas abundances are around $10^{-10} - 10^{-9}$ with various X-ray fluxes. Within the CH_3OH and H_2O snowlines, for low X-ray luminosities, the CH_3OH gas abundances are around $10^{-7} - 10^{-6}$. In contrast, for high X-ray luminosities, the CH_3OH gas abundances decrease and reach below 10^{-16} inside the water snowline.

According to previous studies (e.g., Tielens & Hagen 1982; Watanabe & Kouchi 2002; Cuppen et al. 2009; Fuchs et al.

2009; Drozdovskaya et al. 2014; Furuya & Aikawa 2014; Walsh et al. 2016, 2018; Bosman et al. 2018b; Aikawa et al. 2020), the main pathway to form methanol ice on or within icy mantles of dust grains is CO hydrogenation. Drozdovskaya et al. (2014) discussed the methanol related chemistry both in gas and ice phases, and gas-phase methanol is supplied by the desorption of CH_3OH ice. In our modeling, fragmental X-ray induced photodesorption reactions are included (see Section 2.2.2 of this paper and e.g., Bertin et al. 2016), and the photofragments of CH_3OH (e.g., CH_3 , CH_2OH , CH_3O) will lead to larger and more complex molecules with grain-surface reactions (e.g., Chuang et al. 2016; Drozdovskaya et al. 2016). The gas-phase production via ion-molecule reactions has been considered not to be efficient (Charnley et al. 1992; Garrod & Herbst 2006; Geppert et al. 2006). In the presence of X-rays, gas-phase CH_3OH and other complex organic molecules (COMs) are mainly destroyed by X-ray induced photodissociation in the inner envelopes (e.g., Garrod & Herbst 2006; Öberg et al. 2009b; Drozdovskaya et al. 2014; Taquet et al. 2016a). Therefore, CH_3OH is predicted not to be an efficient tracer of the warm inner envelope and the water snowline position for moderate and high X-ray luminosities. The X-ray ionisation rates $\xi_{\text{X}}(r)$ where CH_3OH loses its efficacy as a water snowline tracer are \gtrsim a few $\times 10^{-17} \text{ s}^{-1}$ (see Figure 2).

3.6. IRAS 4A sub-grid envelope models

In Appendix B, Figure B.1 shows the radial profiles of H₂O, O₂, O, OH, HCO⁺, and CH₃OH gas fractional abundances in the IRAS 4A envelope models, with X-ray luminosities between $L_X = 10^{30}$ and 10^{31} erg s⁻¹. We plot these sub-grid model profiles since there is a large jump in abundances in this X-ray luminosity range (see Figures 3-7). For the abundance profiles of H₂O, HCO⁺ and CH₃OH gas, between 10^{30} and 2×10^{30} erg s⁻¹ seems to be the clear boundary. Compared to them, the abundance profiles of O₂ and O gas gradually increase in the inner region as the values of L_X increase from 10^{30} to $\sim 6 \times 10^{30}$ erg s⁻¹.

3.7. Fractional abundances of other dominant oxygen, carbon, and nitrogen bearing molecules

In Figures C.1, C.2, D.1, and E.1, we show the radial fractional abundances of other dominant oxygen, carbon, and nitrogen bearing molecules (CO₂, CO, CH₄, C₂H, HCN, NH₃, and N₂) for the various X-ray luminosities. According to these figures, as the X-ray flux becomes large, the fractional abundances of gas-phase CH₄, HCN, and NH₃ decrease within their own snowline positions. The gas-phase CO₂ abundances increase at $r \gtrsim 3 \times 10^2$ au (outside the CO₂ snowline), as the X-ray fluxes become larger. At $r \lesssim 3 \times 10^2$ au and for low and moderate X-ray luminosities, the CO₂ gas abundance increases as the X-ray fluxes become larger, and they reach $\sim 10^{-5} - 10^{-4}$ for moderate X-ray luminosities. In contrast, they decrease for high X-ray luminosities (below to $< 10^{-6}$). In addition, the radial CO and N₂ abundance profiles are constant for the various X-ray luminosities, and they are the dominant carbon and nitrogen carriers under the strong X-ray fields. The dependence of radial C₂H gas fractional abundances on X-ray fluxes are much smaller than other dominant molecules. In Appendix C, D, and E, more details about their radial abundance profiles are described.

4. Discussion

4.1. Dominant oxygen carriers

Figure 8 shows the radial profiles of percentage contributions of the dominant oxygen-bearing molecules (CO, H₂O, O, O₂, and CO₂) to the total elemental oxygen abundance ($= 3.2 \times 10^{-4}$) in the IRAS 2A envelope model and the IRAS 4A envelope model at the various assumed X-ray luminosities ($L_X = 10^{28}$, 10^{30} , and 10^{32} erg s⁻¹). Figure 9 shows the pie charts of the percentage contributions of the dominant oxygen-bearing molecules at $r \sim 60$ au ($T_{\text{gas}} \sim 150$ K, inside the water snowline) in the IRAS 2A and IRAS 4A envelope models. Table F.1 in Appendix F shows the fractional abundances of major oxygen bearing molecules at $r = 60$ au in the IRAS 2A and IRAS 4A envelope models for the various X-ray luminosities, and their percentage contributions. We note that O₂ and CO₂ include two oxygen atom per molecule, and thus percentage contributions are twice as much as those of CO, H₂O, and O when they have same abundances with respect to hydrogen nuclei. On the basis of Figures 8 and 9, and Table F.1, for low X-ray luminosities, H₂O and CO molecules are the dominant oxygen carriers ($>90\%$), both in the gas and ice. The percentage contributions of H₂O gas and ice are $\gtrsim 60\%$, and that of CO gas and ice are $\gtrsim 30\%$ throughout the envelopes.

As the X-ray fluxes increase, the abundances of H₂O gas decrease at $r \lesssim 10^2$ au, and those of H₂O ice also decrease

just outside the water snowline ($r \gtrsim 10^2$ au), where the X-ray induced photodesorption is considered to be efficient (see also Section 3.1). Moreover, as the X-ray fluxes increase, the abundances of O₂ and O gas increase in the inner envelopes (inside and just outside the water snowline, see also Section 3.2). For high X-ray luminosities, the water gas abundances at $r \lesssim 10^2$ au become much smaller ($\ll 10^{-6}$), and O₂ and O gas are the dominant oxygen carriers along with CO at $r \lesssim$ a few $\times 10^2$ au. In these cases, the percentage contributions of O₂, O, and CO gas at these radii are $\approx 40\%$, $\lesssim 20\%$, and $\gtrsim 40\%$, respectively. In the outer envelopes where the X-ray induced photodesorption of water is not efficient, H₂O ice and CO gas and ice molecules are still dominant oxygen carriers. In addition, the percentage contributions of CO₂ gas or ice are around 10 – 40% for moderate X-ray luminosities and around 10 – 20% for high X-ray luminosities in the regions where the contributions of O₂ gas and H₂O are similar. As discussed in Section 3.7 and Appendix C, CO₂ gas abundances at $r \lesssim 3 \times 10^2$ au are highest (up to $\sim 10^{-5} - 10^{-4}$) for moderate X-ray luminosities. The outer edge of the region where X-ray induced photodesorption of water is efficient spreads out from $r \sim 10^2$ au to a few $\times 10^2$ au as the values of L_X become larger.

On the basis of our calculations and the discussion above, in order to estimate the total oxygen abundances in the inner envelopes of protostars under the various X-ray luminosities, not only CO and H₂O line observations, but also O₂ and O, and CO₂ line observations are important.

However, as discussed in Section 4.5, O₂ line observations are very difficult and only ¹⁶O¹⁸O lines can be observed with ALMA. The fine structure lines of O are available only at far-infrared wavelengths where dust opacity precludes probing the inner regions in the low-mass protostellar envelopes (see also Section 4.5).

In addition, because of the lack of a permanent dipole moment, CO₂ can only be observed using ro-vibrational absorption or emission lines in the near- and mid-infrared wavelengths (Boonman et al. 2003; Bosman et al. 2017). These lines are included in the wavelengths coverage of James Webb Space Telescope (JWST), and one can probe the CO₂ abundances in the outer envelopes around low-mass protostars through these line observations with JWST, as done for high-mass protostellar envelopes using ISO (van Dishoeck et al. 1996; Boonman et al. 2003). For low-mass protostellar envelopes, a hint of gas-phase CO₂ lines has been obtained using Spitzer (see e.g., Poteet et al. 2013). We note that high dust opacities in these wavelengths make it difficult to probing the CO₂ gas abundances directly in the inner envelopes around low-mass protostars. In Appendix C, the dependence of CO₂ abundances on X-rays in protostellar envelopes are discussed in detail.

4.2. Comparison with observations for IRAS 4A

In the left panel of Figure 10, the observational best-fit $n_{\text{H}_2\text{O}}/n_{\text{H}}$ profile in the IRAS 4A envelope, obtained from van Dishoeck et al. (2021), is overplotted on our model profiles (see also Section 3.1 and the top right panel of Figure 3). This profile is based on analysis of *Herschel*/HIFI spectra which mainly trace the cold outer part (Mottram et al. 2013; Schmalzl et al. 2014), with the modification of the inner ($T_{\text{gas}} > 100$ K) water gas abundance from $> 10^{-4}$ to 3×10^{-6} (Persson et al. 2012, 2014, 2016). In the cold outer part of the

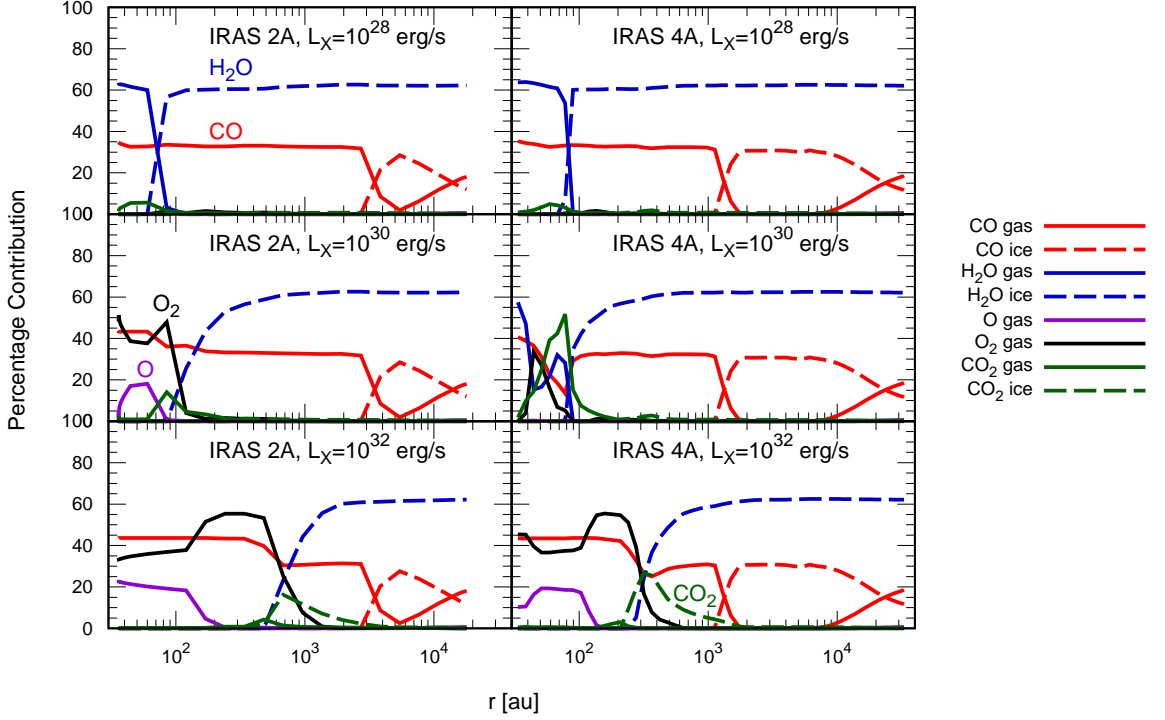


Fig. 8. The radial profiles of percentage contributions of the dominant oxygen-bearing molecules to the total elemental oxygen abundance ($= 3.2 \times 10^{-4}$) in the NGC 1333-IRAS 2A envelope model (left panels) and the NGC 1333-IRAS 4A envelope model (right panels). Top, middle, and bottom panels show the radial profiles with $L_X = 10^{28}$, 10^{30} , and 10^{32} erg s^{-1} , respectively. Red, blue, purple, black, and green line profiles show the contribution of CO, H₂O, O, O₂, and CO₂ molecules, respectively. Solid and dashed line profiles show the contribution of gaseous and icy molecules, respectively. Since O₂ and CO₂ include two oxygen atom per molecule, percentage contributions are twice as much as those of CO, H₂O, and O when they have same fractional abundances with respect to hydrogen nuclei.

envelope ($T_{\text{gas}} < 10^2$ K, $r > 10^2$ au), the best-fit profile is consistent with our model profiles for $L_X \lesssim 10^{28}$ erg s^{-1} . In contrast, in the inner warm envelopes ($T_{\text{gas}} \gtrsim 150$ K, $r \lesssim 60$ au), the gaseous water abundance in the best-fit profile is 3×10^{-6} (Persson et al. 2016), which suggests the possibility of efficient X-ray induced water destructions of gas-phase water molecules with $L_X \gtrsim 10^{30}$ erg s^{-1} in these regions. The reason for this discrepancy between the inner and outer envelope is not clear.

In the cold outer part of the envelope, X-ray induced photodesorption of water molecules controls the water gas abundance. Therefore, if the rates of X-ray induced photodesorption of water are much lower (e.g., $Y_{\text{des}}(\text{H}_2\text{O}) \lesssim 10^{-5}$ molecules photon $^{-1}$) than our adopted values, the water gas abundance profiles in the cold outer part of the envelope for $L_X \gtrsim 10^{30}$ erg s^{-1} are expected to be more similar to the observational profile. In Section 4.3, we discuss the rates of X-ray induced photodesorption in detail, with conducting additional model calculations.

The 3σ upper limit O₂ gas abundance with respect to H₂ obtained by Yıldız et al. (2013) is $\leq 6 \times 10^{-9}$ towards the entire

envelope of IRAS 4A using *Herschel*/HIFI. They estimated that the observed O₂ gas abundance cannot be more than 10^{-6} for the inner warm region ($r \lesssim 10^2$ au). In the right hand panel of Figure 10, the three model abundance profiles calculated in Yıldız et al. (2013) are over-plotted on our model profiles (see also Section 3.2 and the top right panel of Figure 5). The black solid line shows the drop gaseous O₂ abundance profile obtained using the best-fit CO abundance profile produced from the observed C¹⁸O line emission (Yıldız et al. 2012) and assuming O₂ has the same snowline position as CO (= a constant O₂/CO abundance ratio). The blue dashed and the green dotted lines show the gaseous O₂ abundance profiles via their gas-grain modeling with different pre-collapse lifetimes of $t_{\text{pre}} = 8 \times 10^5$ years and $t_{\text{pre}} = 10^6$ years, respectively. As the basis for their gas-grain chemical network (Yıldız et al. 2013), the Ohio State University (OSU) gas-grain network Garrod et al. (2008) is used, which also included gas phase reactions, grain surface reactions, and thermal and non-thermal gas-grain interactions. Although the X-ray induced reactions were not contained, the cosmic-ray induced reactions were included in their calculations.

These three model profiles are consistent with the above

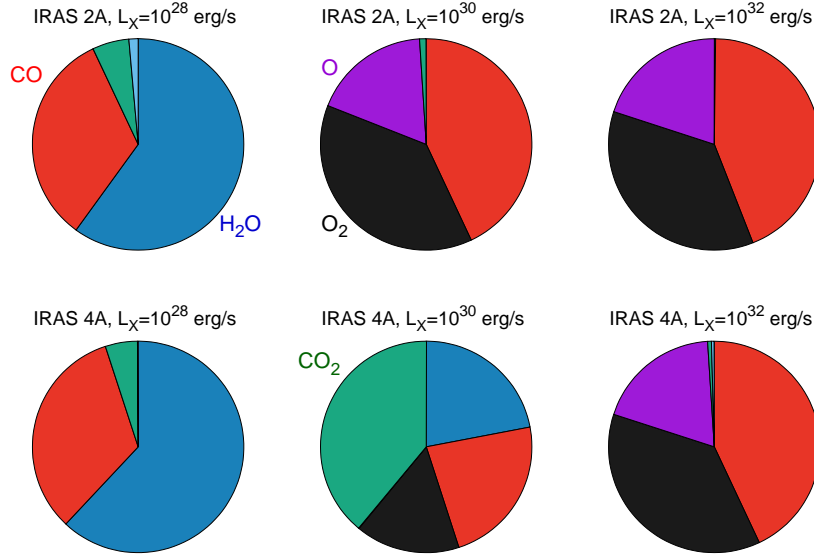


Fig. 9. The pie charts of the percentage contributions of the dominant oxygen-bearing molecules to the total elemental oxygen abundance ($= 3.2 \times 10^{-4}$) at $r \sim 60$ au ($T_{\text{gas}} \sim 150$ K, inside the water snowline) in the NGC 1333-IRAS 2A envelope model (top three charts) and the NGC 1333-IRAS 4A envelope model (bottom three charts). Left, middle, and right charts show the contributions with $L_X = 10^{28}$, 10^{30} , and 10^{32} erg s $^{-1}$, respectively. Red, dark blue, purple, black, green, and sky blue parts are the contributions of CO, H $_2$ O, O, O $_2$, CO $_2$, and other molecules (such as CH $_3$ OH), respectively.

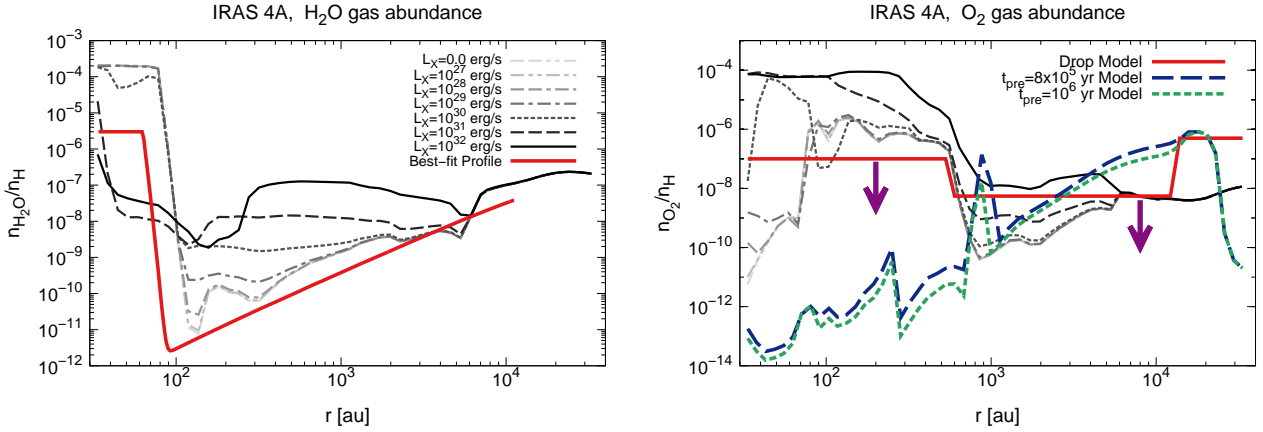


Fig. 10. [Left panel]: The gray-scale plots (from white to black) are the radial profiles of water gas fractional abundances $n_{\text{H}_2\text{O}}/n_{\text{H}}$ in the NGC 1333-IRAS 4A envelope model, which are the same as the color plots in the top right panel of Figure 3. The red solid line shows the observational best-fit $n_{\text{H}_2\text{O}}/n_{\text{H}}$ profile in the IRAS 4A envelope, obtained from van Dishoeck et al. (2021). This profile is based on analysis of *Herschel*/HIFI spectra which mainly trace the cold outer part (Mottram et al. 2013; Schmalzl et al. 2014), with the modification of the inner ($T_{\text{gas}} > 100$ K) water gas abundance from $> 10^{-4}$ to 3×10^{-6} (Persson et al. 2016). [Right panel]: The gray-scale plots (from white to black) are the radial profiles of molecular oxygen gas fractional abundances $n_{\text{O}_2}/n_{\text{H}}$ in the NGC 1333-IRAS 4A envelope model, which are the same as the color plots in the top right panel of Figure 5. The model abundance profiles obtained in Yıldız et al. (2013) are over-plotted. The red solid line shows the drop gaseous O $_2$ abundance profile by using the C 18 O modeling (Yıldız et al. 2012) and assuming O $_2$ follows the same freeze-out and sublimation processes as C 18 O. The blue dashed and the green dotted lines show the gaseous O $_2$ abundance profiles via their gas-grain modeling with $t_{\text{pre}} = 8 \times 10^5$ years and $t_{\text{pre}} = 10^6$ years, respectively. The purple arrows are to indicate that Yıldız et al. (2013) only obtained the upper limit O $_2$ gas abundance for this object.

observational upper limit in Yıldız et al. (2013) (the peak temperatures are similar between models and the observation), and within the values of our chemical modeling at $r \gtrsim 10^3$ au. At $r \sim 10^2 - 6 \times 10^2$ au, the gaseous O $_2$ abundance limit in the drop model is 10^{-7} , which is similar to the values in our model profiles for $L_X \lesssim 10^{30}$ erg s $^{-1}$ within one order of magnitude. In

contrast, at $r < 6 \times 10^2$ au, the gaseous O $_2$ abundance in their gas-grain modeling are much smaller ($\ll 10^{-10}$) than those in our model profiles and that in the drop model.

We note that L_X of IRAS 4A is suggested to be $\gtrsim 10^{30}$ erg s $^{-1}$ by comparing the results of our model calculations

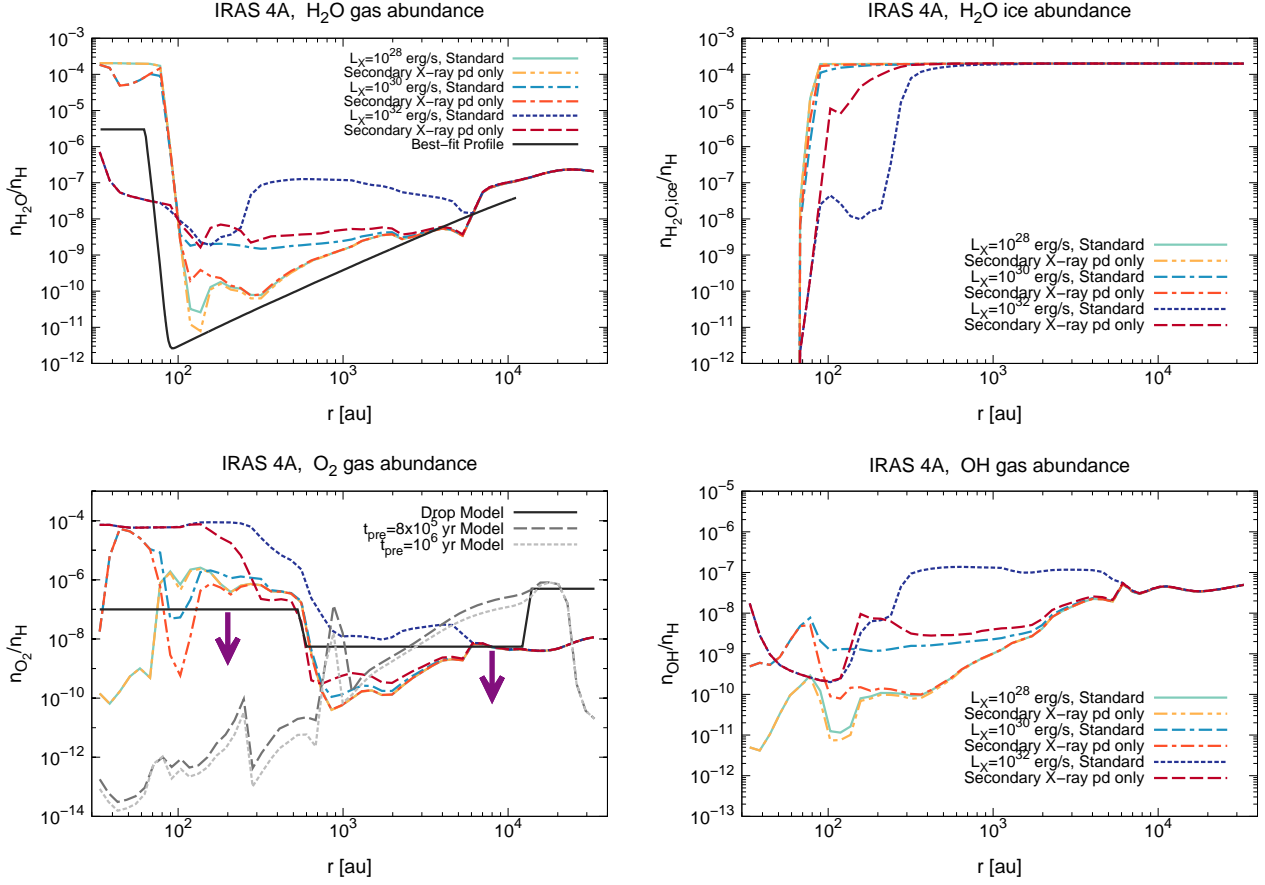


Fig. 11. The radial profiles of gaseous fractional abundances of H_2O , O_2 , and OH , and icy fractional abundances of H_2O in the NGC 1333-IRAS 4A envelope models. The light-green solid lines, the cyan double-dashed dotted lines, and blue dotted lines show the radial profiles of our standard model calculations, for values of central star X-ray luminosities $L_X=10^{28}$, 10^{30} , and 10^{32} erg s^{-1} , respectively (see also Figures 3, 4, 5, 6). The yellow dashed double-dotted lines, the scarlet dashed dotted lines, and the brown dashed lines show the radial profiles of our additional model calculations for $L_X=10^{28}$, 10^{30} , and 10^{32} erg s^{-1} , respectively. In the additional model calculations, we include the photodesorption by UV photons generated internally via the interaction of secondary electrons produced by X-rays with H_2 molecules (the secondary (indirect) X-ray induced photodesorption, see Figures G.1 and G.2), and we also switch off the direct X-ray induced photodesorption (see also Figure G.3). In the top left panel, the observational best-fit H_2O gas abundance profile obtained in van Dishoeck et al. (2021) is over-plotted with the black solid line (see also Figure 10). In the bottom left panel, the three model O_2 gas abundance profiles obtained in Yıldız et al. (2013) are over-plotted (see also Figure 10).

and the observationally estimated inner water gas abundances towards IRAS 4A (see discussions above). Thus, on the basis of the discussions about H_2O and O_2 in this subsection, L_X of IRAS 4A is suggested to be around 10^{30} erg s^{-1} , although the discrepancy of suggested L_X between the inner and outer envelope discussed above is still remained (see also Section 4.3). Since probing the O and CO_2 gas abundances in the inner envelopes are also difficult (see Sections 4.1 and 4.5, and Appendix C), observationally obtaining the abundance profiles of other tracers, especially HCO^+ and CH_3OH , is important to investigate the effects of X-ray induced chemistry and confine the values of L_X (see Section 4.6).

4.3. The rates of X-ray induced photodesorption

In our standard model calculations, we do not include the photodesorption by UV photons generated internally via the interaction of secondary electrons produced by X-rays with H_2 molecules, although we include X-ray induced photodesorption on dust-grains (see also Sections 2.2.2 and 2.2.3).

Our adopted rates of X-ray induced photodesorption are an approximation based on the UV photodesorption rates (see also Section 2.2.2), since experimental constraints for X-ray induced photodesorption are limited (e.g., Walsh et al. 2014a). Recently, Dupuy et al. (2018) experimentally investigated X-ray induced photodesorption rates of H_2O , O_2 , and other related molecules. According to their experiments, photodesorption yields of H_2O and O_2 at 0.55 keV for a compact amorphous solid water ice at 15 K are 3.4×10^{-3} and 4.0×10^{-4} molecules photon^{-1} . The differences of these values and our adopted values are within a factor of a few (see Table 1).

In addition, Dupuy et al. (2018) simply extrapolated X-ray photodesorption yields for higher X-ray photon energies using the absorption cross-sections of water gas. They estimated that the yields of H_2O at 15 K would be $\lesssim 10^{-4}$ at > 3 keV, although further experimental studies will be needed to obtain accurate values. If we estimate the local average X-ray induced photodesorption yields (by multiplying the energy-dependent photodesorption yields by the local X-ray spectrum) on the basis of their simply extrapolated results, the yields would become

lower in the outer envelope with larger values of N_{H} , where softer X-rays are more attenuated.

Here we conduct the two types of additional calculations which focus on the rates of X-ray induced photodesorption and their effect on the chemistry. In the first additional model (see Figures G.1 and G.2 in Appendix G), we include the photodesorption by UV photons generated internally via the interaction of secondary electrons produced by “X-rays” with H_2 molecules. We scale the cosmic-ray-induced photon flux (10^4 photons $\text{cm}^{-2} \text{s}^{-1}$, Walsh et al. 2014a) by the total ionisation rate (cosmic rays plus X-rays) relative to the cosmic-ray ionisation rate only, and use the revised value in estimating the photodesorption rates. According to our calculations (see Figures G.1 and G.2 in Appendix G), the effects of such additional secondary (indirect) X-ray induced photodesorption is marginal (the abundances are changed by $<1\%$). The direct photodesorption by X-ray photons is the dominant process in our calculations.

Next, in the second additional model (see Figures 11 and G.3), we switch off the direct X-ray induced photodesorption and include the secondary (indirect) X-ray induced photodesorption only. Through this calculation, we can also investigate the impact when the rates of the direct X-ray induced photodesorption are much smaller than our originally adopted values. As is seen in Figures 11 and G.3, the effects of X-ray induced photodesorption are decreased relative to the previous case. In the case of H_2O , the gas-phase abundances outside the water snowline for $L_{\text{X}} \gtrsim 10^{30} \text{ erg s}^{-1}$ become around two orders of magnitude smaller than those in our standard model and the first additional model. In addition, in the outer part of the envelope, the observational best-fit profile of H_2O gas is now roughly consistent with the models with $L_{\text{X}} \lesssim 10^{30} \text{ erg s}^{-1}$. We note that in cases of our standard model calculations (see Section 4.2), the best-fit profile is consistent with model profiles for $L_{\text{X}} \lesssim 10^{28} \text{ erg s}^{-1}$ in the outer region, whereas with those for $L_{\text{X}} \gtrsim 10^{30} \text{ erg s}^{-1}$ in the inner region. Thus, lower rates (e.g., $Y_{\text{des}}(\text{H}_2\text{O}) \lesssim 10^{-5}$ molecules photon^{-1}) of direct X-ray induced photodesorption bring the models more in line with the observed abundance profiles, which calls into question whether the direct X-ray desorption rates are over-estimated. We note that the OH gas abundances at $r \sim 10^2 - 10^4$ au for $L_{\text{X}} \gtrsim 10^{30} \text{ erg s}^{-1}$ become 1 – 2 orders of magnitude smaller than those in our standard model and the first additional model, since OH is efficiently produced by X-ray induced photodissociation of H_2O gas and fragmental photodesorption of H_2O ice (see also Section 3.4). In addition, O_2 gas abundances at $r \sim 10^2 - 10^4$ au for $L_{\text{X}} \gtrsim 10^{30} \text{ erg s}^{-1}$ become around several to ten times smaller, since O_2 is formed in the gas-phase of O and OH (see Section 3.2). For other molecules shown in Figure G.3 in Appendix G, the differences in abundances between the standard model and the second additional model are much smaller than those in H_2O , OH, and O_2 .

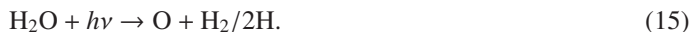
Future experimental and theoretical studies over a wider X-ray energy range are needed to understand how X-ray induced photodesorption rates behave as a function of the X-ray energy spectrum. X-ray induced photodesorption yields are also expected to vary for different ice composition. Basalgète et al. (2021a,b) recently investigated the X-ray induced photodesorption yields of CH_3OH experimentally, and they estimated that the intact yields for mixed methanol-water ices would be more than around two orders of magnitude smaller than those for pure methanol ices.

4.4. Model assumptions for chemistry

In our adopted chemical reaction network (see Section 2), the X-ray induced and cosmic-ray-induced photodissociation of H_2O in both gas and ice is the following route (McElroy et al. 2013);



According to van Harrevelt & van Hemert (2008) and Heays et al. (2017), however, there is another route of photodissociation of H_2O ;



Heays et al. (2017) calculated the photodissociation branching ratio of H_2O using various radiation fields as $\text{OH}/\text{O} \sim 3$, although it depends on wavelength.

In order to investigate the impacts of this photodissociation branching ratio on the abundances of H_2O and related molecules, in Figures 12 and H.1 (see Appendix H) we show the gas-phase abundance profiles of H_2O , O_2 , O, and OH, which are calculated assuming the extreme case that the product of H_2O photodissociation is 100% atomic oxygen (Reaction 15 only both in the gas and ice), and compare them with the profiles in our standard models (see also Figures 3, 5, and 6). Since the photodissociation of H_2O is important just inside the snowline (see Section 3.1), the abundances around $r \approx 10^2$ au are mainly affected. The OH gas abundances become smaller by a factor of a few at $r \lesssim 10^2$ au than those in our standard model. For $L_{\text{X}} \lesssim 10^{30} \text{ erg s}^{-1}$, the O and O_2 gas abundances increase by around 1 – 2 orders of magnitude at $r \lesssim 10^2$ au compared with those in our standard model. For $L_{\text{X}} \gtrsim 10^{31} \text{ erg s}^{-1}$ where O and O_2 gas become dominant oxygen carries, those abundances are similar between these different models. Outside the water snowline $r > 10^2$ au, these abundances are almost unchanged.

Except atomic oxygen, the differences of binding energies $E_{\text{des}}(j)$ for dominant molecules between our adopted values and those in recent other chemical modeling are up to around several tens of percent (see Table 2 and e.g., Cuppen et al. 2017; Penteado et al. 2017). In our adopted chemical model, $E_{\text{des}}(\text{O})$ is assumed to be 1660 K, on the basis of recent experimental measurements (He et al. 2014; He & Vidalí 2014). Taquet et al. (2016b) and Eistrup & Walsh (2019) adopted similar value of $E_{\text{des}}(\text{O})$. However, some of other recent chemical models (e.g., Eistrup et al. 2016; Bosman et al. 2018b) adopted the older estimated value of 800 K, which is around two times smaller than our adopted values. This value of 800 K has been widely used in many chemical models (e.g., Tielens & Hagen 1982; Hasegawa et al. 1992; Garrod & Pauly 2011), but He et al. (2014) pointed out that it has no strong theoretical derivation and no experimental confirmation.

In order to investigate the impacts of different binding energies of O on molecular abundances, in Figures 12 and H.2 (see Appendix H) we show the gas-phase abundance profiles of H_2O , O_2 , O, and OH, which are obtained from our test calculations assuming the smaller $E_{\text{des}}(\text{O})$ (= 800 K) than that in our fiducial model (= 1660 K), and compare them with the profiles in our standard models (see also Figures 3, 5, and 6). The O gas abundances become larger by up to one order of magnitude at $r \sim (1 - 4) \times 10^2$ au than those in our standard model. In contrast, only for $L_{\text{X}} \lesssim 10^{28} \text{ erg s}^{-1}$ the O_2 gas abundances become smaller by factor of a few at $r \sim (1 - 4) \times 10^2$ au than those in our standard model. The OH and H_2O gas abundances are similar to those in our standard model.

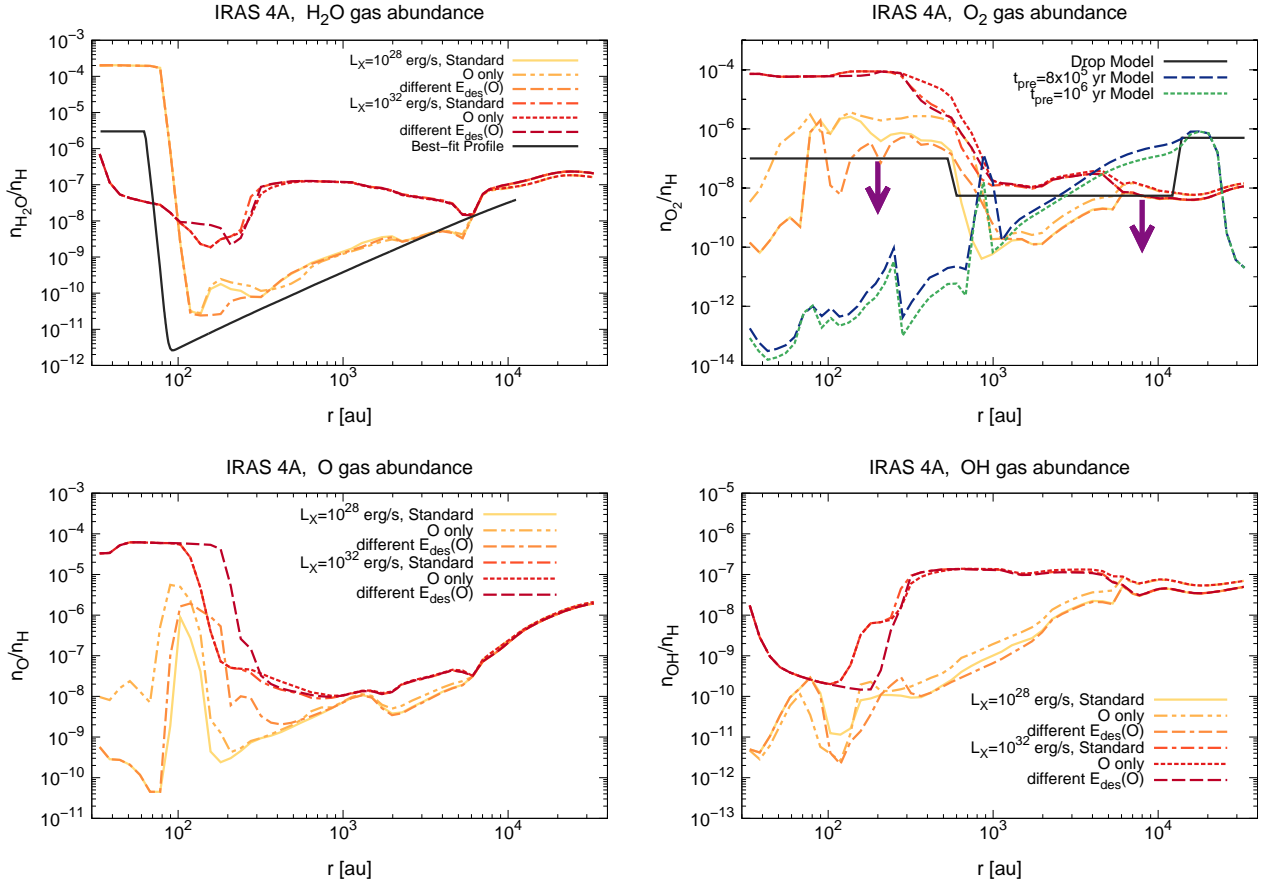


Fig. 12. The radial profiles of gaseous fractional abundances of H_2O , O_2 , O , and OH in NGC 1333-IRAS 4A envelope models. The yellow solid lines and scarlet dashed dotted lines show the radial profiles of our standard model calculations, for values of central star X-ray luminosities $L_X = 10^{28}$ and 10^{32} erg s^{-1} , respectively (see also Figures 3, 5, and 6). The orange dashed double-dotted lines and red dotted lines show those of our test calculations assuming that the product of H_2O photodissociation is 100% atomic oxygen, unlike our standard model (100% OH) (see also Figure H.1). The orange double-dashed dotted lines and brown dashed lines show those of our test calculations assuming the smaller $E_{\text{des}}(j)$ for atomic oxygen (≈ 800 K) than that in our fiducial model (≈ 1660 K) (see also Figure H.2). In the top left panel, the observational best-fit H_2O gas abundance profile obtained in van Dishoeck et al. (2021) is over-plotted with the black solid line (see also Figure 10). In the top right panel, the three model O_2 gas abundance profiles obtained in Yildiz et al. (2013) are over-plotted (see also Figure 10).

4.5. H_2O , O_2 , and O line observations for other protostars

On the basis of previous PdBI (NOEMA) and *Herschel*/HIFI observations (Persson et al. 2012, 2014, 2016; Visser et al. 2013), the water gas abundance is around 10^{-4} in the inner warm envelope and disk of IRAS 2A. In contrast, the water gas abundances in the inner envelopes and disks of IRAS 4A and 4B are lower by 1 – 3 orders of magnitude. Through recent ALMA observations, Jensen et al. (2019) estimated that the H_2^{18}O column densities in the warm inner envelopes around three isolated low-mass Class 0 protostars (L483, B335 and BHR71-IRS1) are around a few $\times 10^{15}$ cm^{-2} , which is similar to that of IRAS 4B, and around 10 times smaller than that of IRAS 2A (Persson et al. 2014). Compared with the results of our chemical modeling, the observational results of IRAS 2A are consistent with the profiles with $L_X \lesssim 10^{29}$ erg s^{-1} . In contrast, the reported inner water gas abundances for IRAS 4A, IRAS 4B, and other objects ($\sim 10^1 - 10^3$ times lower than that for IRAS 2A) are close to the values of our chemical modeling with $L_X \gtrsim 10^{30} - 10^{31}$ erg s^{-1} . Thus, X-ray induced destruction processes can explain the lower water abundances in the inner envelopes of these objects.

Harsono et al. (2020) show that water vapor is not abundant in the warm envelopes and disks around Class I protostars, and upper limit values of the water gas abundance averaged over the inner warm disk with $T_{\text{gas}} > 100$ K are $\sim 10^{-7} - 10^{-5}$. These lower water gas abundances might also be caused by efficient water gas destruction through X-ray induced chemistry, in addition to locking up water in icy dust grains. Future detailed water line observations using e.g., ALMA for more Class 0 and I objects with various X-ray luminosities, and chemical modeling with detailed physical structure models (e.g., disk+envelope, see also van Dishoeck et al. 2014, 2021; Furuya et al. 2017) will clarify the effects of X-ray induced chemistry on water and other related molecules and the water trail from protostellar envelopes to planet-forming regions in disks.

In low-mass protostar observations, only an upper limit and a tentative detection are reported for O_2 lines. This is partly because O_2 does not possess electric dipole-allowed rotational transition lines, and it possess only magnetic-allowed lines (Crowner et al. 1990). In addition to the report of an upper limit toward IRAS 4A using *Herschel*/HIFI (Yildiz et al. 2013) (see Sections 1 and 4.2 of this paper), Taquet et al. (2018)

recently performed a deep search for the $^{16}\text{O}^{18}\text{O}$ 234 GHz $2_1 - 0_1$ line ($E_{\text{up}} = 11.2$ K) toward the inner envelope around a low-mass protostar IRAS 16293-2422 B with ALMA, and reported a residual emission at a 3σ level after subtraction of the contaminated two brighter transitions at ± 1 km s $^{-1}$. However, they considered the detection as “tentative”, since there is a velocity offset of 0.3 – 0.5 km s $^{-1}$ relative to the source velocity. Assuming that the $^{16}\text{O}^{18}\text{O}$ was not detected and using CH $_3$ OH as a reference species, Taquet et al. (2018) obtained a $[\text{O}_2]/[\text{CH}_3\text{OH}]$ abundance ratio $< 2 - 5$, which is 3 – 4 times lower abundance ratio than that in comet 67P/Churyumov-Gerasimenko.

The strong far-infrared [O I] lines (such as the $^3\text{P}_1 - ^3\text{P}_2$ 63.2 μm line) have been used as an outflow and jet tracers in low-mass protostars (e.g., Karska et al. 2013; Nisini et al. 2015; Kristensen et al. 2017), but the inner regions in the protostellar envelopes cannot be probed using these lines because of high dust opacities at far-infrared wavelengths. Spectrally resolved [O I] lines profiles (which can be obtained using such as SOFIA/GREAT) can probe the atomic oxygen abundances in the outer envelopes, if the outflow can be properly disentangled (see also discussions in van Dishoeck et al. (2021)).

4.6. HCO $^+$, CH $_3$ OH, and other molecular line observations

On the basis of our chemical modeling, for $L_X \gtrsim 10^{30} - 10^{31}$ erg s $^{-1}$, HCO $^+$ is not efficiently destroyed within the water snowline, and its abundances remain $\gtrsim 10^{-9}$ both inside and just outside the water snowline (see Section 3.3). In addition, CH $_3$ OH is considered not to be an efficient tracer of the warm inner envelope and the water snowline position for $L_X \gtrsim 10^{30} - 10^{31}$ erg s $^{-1}$ (see Section 3.5). In these cases, the CH $_3$ OH gas abundances are expected to be much smaller (below to 10^{-16}) than those with $L_X \lesssim 10^{29} - 10^{30}$ erg s $^{-1}$ ($\sim 10^{-7} - 10^{-6}$). Thus, observationally obtaining the abundance profiles of HCO $^+$ (including its isotopologue H 13 CO $^+$) and CH $_3$ OH is important to investigate the effects of X-ray induced chemistry in protostellar envelopes.

van 't Hoff et al. (2018a) observationally reported an increase of H 13 CO $^+$ emission just outside the water snowline in the IRAS 2A envelope. It is consistent with the profiles of our modeling with $L_X \lesssim 10^{29}$ erg s $^{-1}$ (see also Section 3.3). We note that observationally obtained inner water gas abundances are also consistent with our model profiles for $L_X \lesssim 10^{29}$ erg s $^{-1}$ (see Section 4.5).

van 't Hoff et al. (2018b) and Lee et al. (2019) reported spatially resolved line images of CH $_3$ OH and other COMs (complex organic molecules) with ALMA toward the disk around the embedded protostar V883 Ori, which is a well-known FU Orionis star (e.g., Cieza et al. 2016). They discussed that the radial extent of CH $_3$ OH gas is around 100 au. In the FU Orionis type stars, sudden increases in the luminosity of the central star will quickly expand the sublimation front (the so-called snowline) to larger radii, which provide good opportunities to study the abundances of COMs in the planet forming materials (Lee et al. 2019).

Lee et al. (2020) obtained spatially resolved images of CH $_3$ OH and H 13 CO $^+$ emission lines with ALMA towards the embedded protostar EC53, in which quasi-periodic emission was reported by the near-infrared monitoring observations (Hodapp et al.

2012) and the submillimeter (JCMT 7) monitoring survey (Herczeg et al. 2017; Yoo et al. 2017), which strongly suggests variable accretion rates. Its luminosities L_{bol} of 1.7-4.8 L_{\odot} (e.g., Evans et al. 2009) and envelope mass M_{env} of 0.86-1.25 (Lee et al. 2020) are similar to those in IRAS 2A and IRAS 4A (the differences are within a factor of 4-5 times). This source is classified as Class I (Giardino et al. 2007), and L_X is around $1 - 3 \times 10^{30}$ erg s $^{-1}$, according to XMM-Newton X-ray observations (Preibisch 2003) and Chandra X-ray observations (Giardino et al. 2007). In this observation, H 13 CO $^+$ line emission is depleted near the continuum peak, where the CH $_3$ OH line emission is present. The CH $_3$ OH emission is more extended than the expected water snowline from the current luminosity of the central star, indicating previous outburst events. However, the derived CH $_3$ OH gas abundance for EC 53 is two orders of magnitude lower than the CH $_3$ OH abundance of $\sim 10^{-8}$ for V883 Ori (Lee et al. 2019), despite the similar size of methanol emitting region. Comparing with the profiles of our modeling, those observed profiles of H 13 CO $^+$ and CH $_3$ OH abundances for EC 53 will be explained if L_X is around $\times 10^{29} - 10^{30}$ erg s $^{-1}$, which is roughly consistent with the observed values of L_X .

Hsieh et al. (2019) reported the detections of the HCO $^+$ (3-2) line with ALMA toward the envelopes around 18 Class 0 and 11 Class I protostars in the Perseus molecular cloud, and also the detections of the CH $_3$ OH 254.015 GHz ($2_{0,2} - 1_{-1,1}$) line toward six of the above sources in which the HCO $^+$ line was detected. They discussed that in four sources where the CH $_3$ OH line was detected, the measured HCO $^+$ peak radii broadly agreed with the CH $_3$ OH emission extents, except two Class 0 sources with very weak CH $_3$ OH emission. In these two Class 0 objects (L1455-IRS4 and L1448-IRS2), both HCO $^+$ and CH $_3$ OH emissions have a similar peak position at the center. Our modeling would suggest that these two sources have strong X-ray emission, destroying H $_2$ O and CH $_3$ OH in the inner regions, leading to weak CH $_3$ OH and strong HCO $^+$ emission, while in the other sources, X-ray luminosities would be lower. This can be tested by independent determination of the X-ray luminosities for these sources, although observations of X-ray luminosities toward embedded Class 0 protostars are difficult (see Section 2.1.2).

CH $_3$ OH and C $_2$ H are the representative products of hot corino chemistry and warm carbon chain chemistry (WCCC) in star-forming cores, respectively (e.g., Sakai & Yamamoto 2013; Imai et al. 2016; Oya et al. 2016; Higuchi et al. 2018; Aikawa et al. 2020; Yang et al. 2021). As shown in Figures 7 and D.1, the dependence of radial profiles of C $_2$ H gas fractional abundances on X-ray fluxes are much smaller than those of CH $_3$ OH gas fractional abundances, in the inner envelopes ($r \lesssim 300$ au). As the X-ray flux increases, the CH $_3$ OH gas fractional abundances significantly decrease (from $10^{-7} - 10^{-6}$ to $< 10^{-15}$) at $r \lesssim 300$ au, whereas the C $_2$ H gas fractional abundances change within two orders of magnitude. Aikawa et al. (2020) investigated the physical conditions which affect the hot corino chemistry and WCCC, and deficiency of COMs (including CH $_3$ OH) in prototypical WCCC sources is hard to reproduce within their models. They discussed that gas-phase destruction processes of CH $_3$ OH and other COMs within several 10^4 years after sublimation from dust grains would be important (Charnley et al. 1992; Nomura et al. 2009; Taquet et al. 2016a). X-ray induced destruction reactions discussed in this

⁷ James Clerk Maxwell Telescope

paper would help to destroy these molecules within the above timescale.

Recently, the line observations of CH₃OH and other molecules (including COMs and C₂H) with much higher spatial resolutions ($\Delta r \lesssim$ several tens of au) have been conducted with ALMA and VLA towards disks and inner envelopes around Class 0 and I protostars (e.g., Sahu et al. 2019; Bianchi et al. 2020; De Simone et al. 2020, and FAUST⁸). These detailed observations can also be used to constrain the effects of X-ray induced chemistry on the abundance profiles of HCO⁺, CH₃OH, and other molecules. In addition, future molecular line observations with e.g., ngVLA⁹ will also be helpful. They are expected to constrain the inner gas abundances of CH₃OH, other COMs (Öberg et al. 2018), HCO⁺, and NH₃, which are also affected by X-ray induced chemistry (see Appendix E and Zhang et al. 2018), creating a more complete picture of the oxygen chemistry and opening a window into the independent nitrogen chemistry. Moreover, since the dust opacities in the frequencies of ngVLA are smaller than those of ALMA (see also e.g., De Simone et al. 2020), these observations will be useful to trace the inner gas abundances more precisely.

Particles are accelerated in shocks along the protostellar jets and on the protostellar surfaces, and they can enhance the cosmic-ray ionization rates in protostellar envelopes (e.g., Padovani et al. 2016). However, because of the differences in energies, they are much more transparent compared with X-rays, and they affect the ionization rates and thus abundances of ion molecules (such as HCO⁺ and N₂H⁺) not only in the inner regions, but also in the outermost regions, such as $r > 10^3$ au (Ceccarelli et al. 2014; Favre et al. 2017). Ceccarelli et al. (2014) reported a HCO⁺/N₂H⁺ abundance ratio of around 3-4 in the outer envelopes ($r >$ a few $\times 10^3$ au) around the protostar OMC-2 FIR4 from *Herschel* observations, which was very low compared to that in other protostellar envelopes ($\gg 10$). They suggested that the cosmic-ray ionization rate is around 10^{-14} s^{-1} , which is much higher than the average value in dense clouds ($\sim 10^{-17} \text{ s}^{-1}$, Umebayashi & Nakano 2009).

In addition, van 't Hoff et al. (2018a) conducted a first order approximation of the effect of cosmic-ray ionization rates on the HCO⁺ gas abundances in the outer envelopes, by considering the main formation (CO+H₃⁺) and destruction (HCO⁺ + e⁻) reactions of HCO⁺ outside the water snowline. Assuming steady state and the similar abundances for HCO⁺ and electron ($n_{\text{HCO}^+}/n_{\text{H}} \approx n_{\text{e}^-}/n_{\text{H}}$), they obtained the following expression for the HCO⁺ gas densities n_{HCO^+} in the outer envelopes,

$$n_{\text{HCO}^+} = \sqrt{\frac{\xi_{\text{CR}} n_{\text{H}_2}}{k_5}}, \quad (16)$$

where k_5 is the rate coefficient of the main destruction reaction of HCO⁺ + e⁻ (for more details, see Appendix B of van 't Hoff et al. (2018a)). Thus, with investigating the abundances of ion molecules such as HCO⁺ both the inner and outer regions, we could distinguish the effects of X-ray induced ionization and cosmic-ray induced ionization accelerated by e.g., protostellar jets. According to our model calculations ($\xi_{\text{CR}}(r) = 10^{-17} \text{ s}^{-1}$), the HCO⁺ abundances at $r \gtrsim 10^3$ au are $\sim 10^{-9} - 10^{-8}$ for IRAS 2A, and $\sim 10^{-10} - 10^{-9}$ for IRAS 4A.

Thus, if the HCO⁺ abundances at these radii are more than an order of magnitude higher, $\xi_{\text{CR}}(r)$ is estimated to be $\gtrsim 10^{-15} \text{ s}^{-1}$.

We note that Bruderer et al. (2009) and Benz et al. (2016) offered an alternative explanation for enhanced HCO⁺, originating in the UV irradiated warm outflow cavity walls. Spatially resolved observations for HCO⁺ lines are needed to distinguish the scenarios.

4.7. Chemical evolution from envelopes to disks

In our chemical modeling, we assume that the physical structures (especially the radial n_{H_2} and T_{gas} profiles) are constant throughout 10^5 years. However, the timescale of the main accretion phase of protostars (Class 0-I) is around a few 10^5 years (Dunham et al. 2014; Kristensen & Dunham 2018), and material in the envelopes moves inward (e.g., Visser et al. 2009, 2011; Harsono et al. 2015; Furuya et al. 2017). According to our calculations, for the highest X-ray luminosities of $L_{\text{X}} \gtrsim 10^{31} \text{ erg s}^{-1}$, the X-ray induced reactions in the inner envelopes proceed with shorter time scales of $t < 10^3$ years than the timescale of the main accretion phase, although the timescale of grain surface chemistry are longer ($t \gg 10^5$ years, see also Yoneda et al. 2016). Aikawa et al. (2008, 2020) suggested that the infalling material passes through the region with $T_{\text{gas}} \sim 10^1 - 10^2 \text{ K}$ in several 10^4 years, and fall into the central star and the disk $\sim 10^2$ years after they enter the region with $T_{\text{gas}} > 10^2 \text{ K}$. Therefore, the molecular abundances in the inner envelopes, especially in the innermost region, would be affected because of such inward accretion, unless they enter a rotating disk-like structure (Schöier et al. 2002).

In our chemical modeling of this paper, we assume that X-ray luminosities are constant throughout 10^5 years. However, X-ray luminosities of central protostars and X-ray fluxes in surrounding envelopes are expected to be changed with time, because protostar X-ray flares are the dominant X-ray source and they occur repeatedly once in around 10 days (Takasao et al. 2019). In the presence of strong X-ray fluxes, water is considered to be efficiently destroyed with very short timescale of $t < 10^3$ years (Stäuber et al. 2006) in the disks and the inner envelopes around protostars. Thus repetition of sudden increase (and decrease) of X-ray luminosities would also affect molecular abundances in the disks and inner envelopes around Class 0 and I protostars.

As future studies, the detailed chemical modeling with time-dependent physical structures of disks and envelopes around Class 0 and I protostars will be important to understand the effects of X-ray induced chemistry on the abundance profiles of water and related molecules in detail. We note that Cleaves et al. (2017) reported the time variation of the H¹³CO⁺ J= 3 – 2 line intensities in a Class II disk between three observational epochs, and they discussed that the enhancement of HCO⁺ abundance in the upper layer of the disk would be explained by X-ray driven chemistry during large X-ray flare events. Waggoner & Cleaves (2019) discussed that the day-scale impulsive increase and decrease of the H₂O gas abundances in the surfaces of Class II disks could be caused by the time dependent chemistry driven by X-ray flares.

According to our chemical modeling, X-ray induced chemistry affects the abundances profiles of H₂O and other dominant

⁸ <http://faust-almalab.riken.jp>

⁹ the next generation Very Large Array

molecules, such as O, O₂, HCO⁺, CH₃OH, OH, CO₂, CH₄, HCN, and NH₃. In the presence of strong X-ray fields (with $L_X \gtrsim 10^{30} - 10^{31} \text{ erg s}^{-1}$), the abundances of H₂O, CH₃OH, CH₄, HCN, and NH₃ significantly decrease in the inner envelopes around protostars, and CO, O₂, O become the dominant oxygen carriers. In addition, on the basis of Figures C.1-E.1, CO and N₂ become the dominant carbon and nitrogen carriers under such strong X-ray fields. Note that the material in the protostellar envelopes accretes into disks, thus the molecular abundances in protostellar envelopes determine the initial abundances of chemical evolution in disks, where planet formation occurs (see also the recent review by Öberg & Bergin 2021). In many studies of chemical modeling in disks (e.g., Walsh et al. 2015; Bosman et al. 2018b), initial chemical abundances were assumed to be inherited from dark clouds, pre-stellar cores, and protostellar envelopes, and they are water-rich, on the basis of previous observations (e.g., Visser et al. 2009, 2011; Boogert et al. 2015). However, whether the disk chemical evolution is started from initial abundance conditions of the chemical reset (by e.g., irradiation, accretion shocks) or the inheritance from the dark clouds and protostellar envelopes is an important question (e.g., Yoneda et al. 2016; Coutens et al. 2020; Jørgensen et al. 2020; van't Hoff et al. 2020; Öberg & Bergin 2021). Eistrup et al. (2016, 2018) and Notsu et al. (2020) discussed that the chemical abundances in Class II disks are strongly affected by ionisation rates in disks and the adopted initial molecular abundances (inheritance or reset). In the presence of strong X-ray fields (with $L_X \gtrsim 10^{30} - 10^{31} \text{ erg s}^{-1}$), the molecular abundances in protostellar envelopes are also altered from inheritance initial molecular abundances.

In future studies, the chemical modeling in disks with initial abundances which consider the effects of X-ray induced chemistry discussed in this paper will be important to understand the chemical evolution history in disks and the chemical compositions of exoplanets (e.g., Notsu et al. 2020; Turrini et al. 2021).

5. Conclusions

We investigated the radial dependence of the abundances of water and related molecules on X-rays in Class 0 low-mass protostellar envelopes, and identify potential oxygen carriers other than water. We used a detailed gas-grain chemical reaction network including X-ray-induced chemical processes. Gas-phase reactions, thermal and non-thermal gas-grain interactions, and grain-surface reactions are included in our adopted chemical reaction network. For the physical structures of the Class 0 protostellar envelopes, we adopted two type of spherically symmetric radial gas temperature T_{gas} and molecular hydrogen number density n_{H_2} profiles for IRAS 2A and IRAS 4A, in order to examine the effect of density differences on X-ray induced chemistry. Our findings can be summarized as follows:

- Outside the water snowline ($T_{\text{gas}} < 10^2 \text{ K}$, $r > 10^2 \text{ au}$), if X-ray luminosities of the central protostars L_X are larger than $10^{30} \text{ erg s}^{-1}$, water gas fractional abundances are increased (up to $n_{\text{H}_2\text{O}}/n_{\text{H}} \sim 10^{-8} - 10^{-7}$), compared with the values ($n_{\text{H}_2\text{O}}/n_{\text{H}} \sim 10^{-10}$) for $L_X < 10^{30} \text{ erg s}^{-1}$. In addition, water ice abundances are around 2×10^{-4} outside the water snowline for $L_X \lesssim 10^{30} \text{ erg s}^{-1}$, and they become much smaller (below to $n_{\text{H}_2\text{O,ice}}/n_{\text{H}} \sim 10^{-8}$ at a few $\times 10^2 \text{ au}$) for $L_X \gtrsim 10^{31} \text{ erg s}^{-1}$. X-ray induced photodesorption

of water ice affects in this region. Since there are limited experimental constraints for X-ray induced photodesorption rates, future theoretical and experimental studies for the X-ray induced photodesorption over a wider X-ray energy ranges are important.

- Inside the water snowline ($T_{\text{gas}} > 10^2 \text{ K}$, $r < 10^2 \text{ au}$), for $L_X \lesssim 10^{29} - 10^{30} \text{ erg s}^{-1}$, water maintains a high abundance of $\sim 10^{-4}$, and water and CO are the dominant oxygen carriers. For $L_X \gtrsim 10^{30} - 10^{31} \text{ erg s}^{-1}$, the water gas abundances significantly decrease just inside the water snowline ($T_{\text{gas}} \sim 100 - 250 \text{ K}$, down to $n_{\text{H}_2\text{O}}/n_{\text{H}} \sim 10^{-8} - 10^{-7}$) and in the innermost regions ($T_{\text{gas}} \sim 250 \text{ K}$, $n_{\text{H}_2\text{O}}/n_{\text{H}} \sim 10^{-6}$). In the presence of strong X-ray fields, gas-phase water is mainly destroyed with the ion-molecule reactions and the X-ray induced photodissociation. In our chemical modeling, the former ion-molecule reactions are dominant processes for the water gas destruction inside the water snowline. For $L_X \gtrsim 10^{29} - 10^{30} \text{ erg s}^{-1}$, the X-ray ionization rates $\xi_X(r)$ are larger than our adopted cosmic ray ionization rate $\xi_{\text{CR}}(r) (= 1.0 \times 10^{-17} \text{ s}^{-1})$ within the water snowline. In the innermost hot region, water abundances become relatively large since the two-body water formation reaction (OH+H₂) becomes efficient.
- As the X-ray fluxes become larger, the O₂ and O gas abundances become larger both inside and outside the water snowline. Inside the water snowline, both O₂ and O gas abundances are much smaller ($< 10^{-8}$) for $L_X \lesssim 10^{28} - 10^{29} \text{ erg s}^{-1}$. In contrast, for $L_X \gtrsim 10^{29} - 10^{30} \text{ erg s}^{-1}$, their abundances become larger, and reach about 10^{-4} with $L_X \gtrsim 10^{31} \text{ erg s}^{-1}$. Compared with the water gas abundances, both O₂ and O gas abundances have opposite dependence on X-ray fluxes. For $L_X \gtrsim 10^{30} - 10^{31} \text{ erg s}^{-1}$, O₂, O, and CO become the dominant oxygen carriers in the inner envelopes ($r \lesssim$ a few $\times 10^2 \text{ au}$).
- According to previous studies, the most abundant destroyer of HCO⁺ in warm gas is water, and the radius of the CH₃OH snowline ($\sim 2 \times 10^2 \text{ au}$) is around two times larger than that of the water snowline ($\sim 10^2 \text{ au}$). Thus, CH₃OH and HCO⁺ (and also H¹³CO⁺) gas lines have been used as good tracers of the water snowline. In our modeling, the HCO⁺ and CH₃OH gas abundances are increased/decreased within the water snowline, respectively, as the X-ray fluxes become larger. For $L_X \gtrsim 10^{30} - 10^{31} \text{ erg s}^{-1}$, the HCO⁺ abundances within the water snowline increase by four orders of magnitude, and reach more than $10^{-9} - 10^{-10}$, which are similar to those outside the water snowline. In contrast, CH₃OH gas abundance in these radii decrease from $\sim 10^{-7} - 10^{-6}$ to $< 10^{-16}$. Therefore, both HCO⁺ and CH₃OH cannot be used as tracers of the water snowline position for $L_X \gtrsim 10^{30} - 10^{31} \text{ erg s}^{-1}$. Observationally obtaining the abundance profiles of HCO⁺, H¹³CO⁺, and CH₃OH is important to investigate the effects of X-ray induced chemistry in protostellar envelopes.
- The gas-phase fractional abundances of OH and CO₂ increase in the outer disk ($>$ a few hundred au), as the X-ray fluxes become larger. At $r <$ a few hundred au, for $L_X \lesssim 10^{29} - 10^{30} \text{ erg s}^{-1}$, OH and CO₂ gas abundances increase as the X-ray fluxes become larger. CO₂ gas abundances are $\sim 10^{-5} - 10^{-4}$ at $L_X \sim 10^{29} - 10^{30} \text{ erg s}^{-1}$. In these cases, CO₂ also becomes one of dominant oxygen bearing molecules, especially in the regions where the abundances

of O_2 gas and H_2O are similar. However, OH and CO_2 gas abundances decrease for $L_X \gtrsim 10^{30} - 10^{31} \text{ erg s}^{-1}$, and CO_2 gas abundances are $\lesssim 10^{-6}$ at $L_X \gtrsim 10^{31} - 10^{32} \text{ erg s}^{-1}$.

numbers ST/R000549/1 and ST/T000287/1). H.N. is supported by MEXT/JSPS Grants-in-Aid for Scientific Research (KAKENHI) 18H05441, 19K03910 and 20H00182, NAOJ ALMA Scientific Research grant No. 2018-10B, and FY2019 Leadership Program at NAOJ.

- As X-ray fluxes become large, the fractional abundances of gas-phase CH_4 , HCN, and NH_3 are decreasing within their own snowline positions. The radial CO and N_2 abundance profiles are constant for the various X-ray luminosities, and they are the dominant carbon and nitrogen carriers under the strong X-ray fields.
- The effects of X-ray induced chemistry are larger in the IRAS 2A model than those in the IRAS 4A model, which has 3 – 6 times larger in densities.
- Comparing the results of our modeling with the observationally obtained inner gas abundances of H_2O and $H^{13}CO^+$, L_X of IRAS 2A is estimated to be $\lesssim 10^{29} \text{ erg s}^{-1}$. In addition, our models with $L_X \sim 10^{30} \text{ erg s}^{-1}$ would explain both the low inner water gas abundances and the upper limit values of O_2 gas abundances obtained by previous observations towards IRAS 4A. However, in the cold outer part of the envelope, the best-fit profile obtained from observations is consistent with our model profiles for $L_X \lesssim 10^{28} \text{ erg s}^{-1}$. The discrepancy of suggested L_X between the inner and outer envelope is remained, unless the rates of direct X-ray induced photodesorption of water are around two orders of magnitude lower than our adopted values. Since probing the O and CO_2 gas abundance in the inner envelopes are difficult, observationally obtaining the abundance profiles of other tracers, especially HCO^+ and CH_3OH , is important to investigate the effects of X-ray induced chemistry and confine the values of L_X .

On the basis of our chemical modeling, X-ray induced chemistry strongly affects the abundances of water and other related molecules (such as O_2 , O, HCO^+ , CH_3OH , CO_2 , OH, CH_4 , HCN, and NH_3) especially in the inner regions, and can explain the observed low water abundances in the inner protostellar envelopes. We find that gas-phase destruction of molecules by X-rays as well as X-ray-induced photodesorption processes are important. Future molecular line observations towards the disks and envelopes around low-mass protostars, using e.g., ALMA and ngVLA, will constrain the effects of X-ray induced chemistry. In addition, it will be important to discuss how the X-ray induced chemistry at protostar phases affect the initial abundances and chemical evolution in planet forming disks.

Acknowledgements.

We are grateful to Daniel Harsono, Umut A. Yıldız, Joseph C. Mottram, Merel L. R. van't Hoff, and Lars E. Kristensen for giving us the data of temperature, number density, and water abundance profiles estimated from previous observations of Class 0 protostellar envelopes. We thank Shinsuke Takasao and Masanobu Kunitomo for their important comments about X-ray fields in protostars. We are also grateful to Yuri Aikawa for her useful comments on chemical evolutions and to Nami Sakai for her comments on the possibility of future ngVLA observations. We thank the referee for important suggestions and comments. Our numerical studies were carried out on PC cluster at Center for Computational Astrophysics (CfCA), National Astronomical Observatory of Japan (NAOJ), and on computer systems at Leiden Observatory, Leiden University. S.N. is grateful for support from JSPS (Japan Society for the Promotion of Science) Overseas Research Fellowships, RIKEN Special Postdoctoral Researcher Program (Fellowships), and MEXT/JSPS Grants-in-Aid for Scientific Research (KAKENHI) 20K22376, 20H05845, and 20H05847. C.W. acknowledges financial support from the University of Leeds and from the Science and Technology Facilities Council (grant

Appendix A: The dependance of X-ray induced chemistry on gas number density

In this section, we investigate the dependance of X-ray induced chemistry on the gas number density. The rates of formation or destruction for gas-phase species Y due to the X-ray induced photoionisation and photodissociation reactions are scaled with $\zeta_X(r) \times n_Y$, and these are first-order kinetic processes with regard to gas densities. In contrast, ion-molecule reactions, neutral-neutral reactions, are second-order kinetic processes with regard to gas densities. Thus, given the same X-ray ionisation rates $\zeta_X(r)$ and gas temperatures T_{gas} , the more important the latter “second-order” processes are, and the less important the former “first-order” processes are, as the gas density increases.

At $r \sim 60$ au (inside the water snowline), the gas density in IRAS 4A ($n_{\text{H}_2} = 1.1 \times 10^9 \text{ cm}^{-3}$) is around 5.5 times larger than that in IRAS 2A ($n_{\text{H}_2} = 2.0 \times 10^8 \text{ cm}^{-3}$), whereas the gas temperatures are similar ($T_{\text{gas}} \sim 140$ K for IRAS 2A and ~ 150 K for IRAS 4A). For $L_X = 10^{32} \text{ erg s}^{-1}$, $\zeta_X(r)$ in IRAS 4A ($2.0 \times 10^{-14} \text{ s}^{-1}$) is around 4.4 times lower than that in IRAS 2A ($8.8 \times 10^{-14} \text{ s}^{-1}$). We conduct a test chemical calculation, in which we adopt the IRAS 4A physical structure (n_{H_2} and T_{gas}) at $r \sim 60$ au and $L_X = 10^{32} \text{ erg s}^{-1}$, and rescale $\zeta_X(r)$ to the value at a similar radius in the IRAS 2A model. We compare the rates of reactions of this test calculation with those of the standard IRAS 2A model.

In this test calculation, at $t = 10^5$ years, the fractional abundance and absolute number density of water are 6.9×10^{-8} and $1.5 \times 10^2 \text{ cm}^{-3}$, respectively, and the same for HCO^+ are 4.2×10^{-9} and 9.4 cm^{-3} , respectively. On the basis of these values, the rate coefficient of the ion-molecule reaction with $\text{H}_2\text{O} + \text{HCO}^+ \rightarrow \text{CO} + \text{H}_3\text{O}^+$, k_6 , is $\sim 3.5 \times 10^{-9} \text{ cm}^3 \text{ s}^{-1}$ (Adams et al. 1978), and the reaction rate, $R(6) = k_6 n_{\text{H}_2\text{O}} n_{\text{HCO}^+}$, is $\sim 2.2 \times 10^{-5} \text{ cm}^{-3} \text{ s}^{-1}$ at $t = 10^5$ years. In contrast, the rate coefficient of X-ray-induced photodissociation leading to $\text{H} + \text{OH}$, k_7 , is $\sim 8.6 \times 10^{-11} \text{ s}^{-1}$ (Gredel et al. 1989), and the reaction rate, $R(7) = k_7 n_{\text{H}_2\text{O}}$, is $\sim 1.3 \times 10^{-8} \text{ cm}^{-3} \text{ s}^{-1}$ at $t = 10^5$ years.

Comparing these reaction rates with those of the standard IRAS 2A model (see Section 3.1), the differences of the reaction rates are larger in the former ion-molecule reaction ($R(6)/R(1) \sim 25$) than the latter X-ray-induced photodissociation ($R(7)/R(2) \sim 2.5$). It is because the former reaction is the “second-order” process and the latter reaction is the “first-order” process. Thus, as the gas densities become larger, the “second-order” processes including ion-molecule reactions become much more dominant compared with the “first-order” processes including X-ray-induced photodissociation.

Appendix B: Sub-grid calculations for the IRAS 4A envelope models

Figure B.1 shows the radial profiles of H_2O , O_2 , O , OH , HCO^+ , and CH_3OH gas fractional abundances in the IRAS 4A envelope models, with X-ray luminosities between $L_X = 10^{30}$ and $10^{31} \text{ erg s}^{-1}$. We plot these sub-grid model profiles since there is a large jump in abundances in this X-ray luminosity range (see Figures 3-7). For the abundance profiles of H_2O gas, between 10^{30} and $2 \times 10^{30} \text{ erg s}^{-1}$ seems to be the clear boundary, and they decrease from $\sim 10^{-4}$ to $< 10^{-7}$ at $r \lesssim 10^2$ au. For the abundance profiles of HCO^+ and CH_3OH gas, between 10^{30} and $2 \times 10^{30} \text{ erg s}^{-1}$ also seems to be the clear boundary. Compared to them,

the abundance profiles of O_2 and O gas gradually increase in the inner region as the values of L_X increase from 10^{30} to $\sim 6 \times 10^{30} \text{ erg s}^{-1}$.

Appendix C: CO_2 and CO fractional abundances

Figure C.1 shows the radial profiles of CO_2 gas and ice fractional abundances $n_{\text{CO}_2}/n_{\text{H}}$ in IRAS 2A (left panels) and IRAS 4A (right panels) envelope models, for the various X-ray luminosities. At $r \sim 3 \times 10^2 - 4 \times 10^3$ au (in the IRAS 2A model) and $r \sim 3 \times 10^2 - 2 \times 10^3$ au (in the IRAS 4A model), which are the regions between CO_2 and CO snowlines, CO_2 ice abundances are around 10^{-6} for $L_X \lesssim 10^{30} \text{ erg s}^{-1}$. In contrast, for $L_X \gtrsim 10^{31} \text{ erg s}^{-1}$, CO_2 ice abundances increase (up to 10^{-5}) in these regions. On the basis of Drozdovskaya et al. (2016), Eistrup et al. (2016, 2018), and Bosman et al. (2018b), in the presence of X-ray fluxes, the X-ray induced photodissociation of H_2O ice forms OH radicals within the ice mantle, which subsequently react with CO on grain surfaces to form CO_2 ice inside the CO snowline.

CO_2 gas abundances at $r \lesssim 10^4$ au in the IRAS 2A model and at $r \lesssim 6 \times 10^3$ au in the IRAS 4A model are affected by strong X-ray fluxes. For low and moderate X-ray luminosities¹⁰, CO_2 gas abundances become smaller, and reach $\lesssim 10^{-9}$ at $r \sim 3 \times 10^2 - 10^3$ au (outside the CO_2 snowline). In contrast, for high X-ray luminosities, CO_2 gas abundances become larger, and they reach around 10^{-6} (for IRAS 2A) and 10^{-7} (for IRAS 4A) at these radii for $L_X \sim 10^{32} \text{ erg s}^{-1}$. At $r \lesssim 3 \times 10^2$ au (inside CO_2 snowline), CO_2 abundances are around $10^{-6} - 10^{-5}$ for low X-ray luminosities. In addition, like OH , the CO_2 gas abundances increase as the X-ray fluxes become larger, and they reach $\sim 10^{-5} - 10^{-4}$ for moderate X-ray luminosities. However, they decrease for high X-ray luminosities. At $L_X \gtrsim 10^{31} \text{ erg s}^{-1}$ in the IRAS 2A model and $L_X \gtrsim 10^{32} \text{ erg s}^{-1}$ in the IRAS 4A model, the CO_2 gas abundances are around $3 \times 10^{-7} - 10^{-6}$.

Outside the CO_2 snowline, CO_2 gas is supplied by X-ray induced photodesorption reaction of CO_2 ice. In the inner envelope, gas-phase CO_2 is mainly formed by two body reaction of $\text{CO} + \text{OH}$ (Bosman et al. 2017), and destroyed with X-ray induced photodissociation. Therefore, CO_2 abundance profiles strongly depend on the radial profiles of X-ray fluxes and OH abundances.

The CO_2 abundances in the outer envelopes around low-mass protostars can be probed through the observations CO_2 ro-vibrational lines with JWST (see also Section 4.1), as done for high-mass protostellar envelopes using ISO (van Dishoeck et al. 1996; Boonman et al. 2003). For low-mass protostellar envelopes, a hint of gas-phase CO_2 lines has been obtained using Spitzer (see e.g., Poteet et al. 2013). We note that high dust opacities in the near and mid-infrared wavelengths make it difficult to probing the CO_2 gas abundances directly in the inner envelopes around low-mass protostars.

Boonman et al. (2003) and Bosman et al. (2018a) noted the disagreements of CO_2 gas abundances within the CO_2 snowline between models ($\sim 10^{-5}$) and observations ($\sim 10^{-7}$), both for high-mass protostar envelopes and Class II disks. Bosman et al. (2018a) discussed that the CO_2 should be de-

¹⁰ For the definition of the values of low, moderate, and high X-ray luminosities, please see Section 3.2.

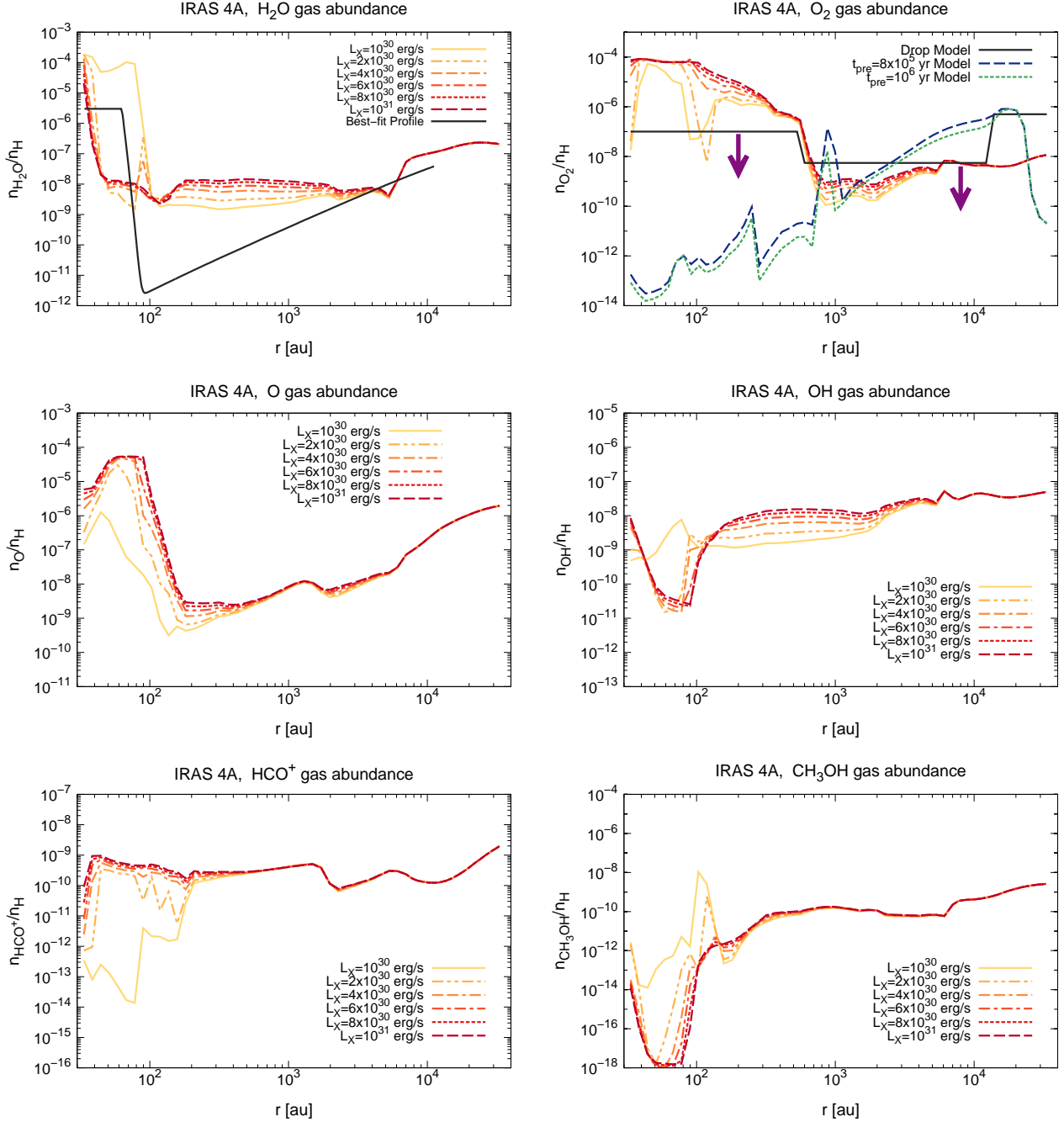


Fig. B.1. The radial profiles of gaseous fractional abundances of H_2O , O_2 , O , OH , HCO^+ , and CH_3OH in the NGC 1333-IRAS 4A envelope models, with X-ray luminosities between $L_X = 10^{30}$ and 10^{31} erg s^{-1} . The line colors are gradually change from yellow to orange, red, and brown as the values of L_X increase. In the top left panel, the observational best-fit H_2O gas abundance profile obtained in van Dishoeck et al. (2021) is over-plotted, as we plot in Figure 10. In the top right panel, the three model O_2 gas abundance profiles obtained in Yildiz et al. (2013) are over-plotted, as we plot in Figure 10.

stroyed within 10^4 years after the sublimation of CO_2 ice. X-ray induced destruction reactions discussed in this paper would help to destroy CO_2 molecules within the above timescale, assuming that CO_2 chemistry is similar among these type of sources.

Figure C.2 shows the radial profiles of CO gas and ice fractional abundances $n_{\text{CO}}/n_{\text{H}}$ in IRAS 2A (left panels) and IRAS 4A (right panels) envelope models, for the various X-ray luminosities. Unlike other dominant oxygen-bearing molecules (e.g., H_2O , O_2 , O , CO_2), both of CO gas and ice abundances

do not depend on X-ray fluxes. CO gas fractional abundances are around 10^{-4} at $r \lesssim 3 \times 10^3$ au at IRAS 2A and $r \lesssim 10^3$ au at IRAS 4A (within the CO snowline), and CO ice fractional abundances are around 10^{-4} at $r \gtrsim 4 \times 10^3$ au at IRAS 2A and $r \gtrsim 10^3$ au at IRAS 4A (outside the CO snowline).

With an ISM level cosmic-ray ionisation rate of $\xi_{\text{CR}}(r) = 1.0 \times 10^{-17} \text{ s}^{-1}$, longer timescale ($> 10^6$ years, which is a typical age of Class II disks) than that in our modeling (10^5 years, which is a typical age of Class 0 protostars)

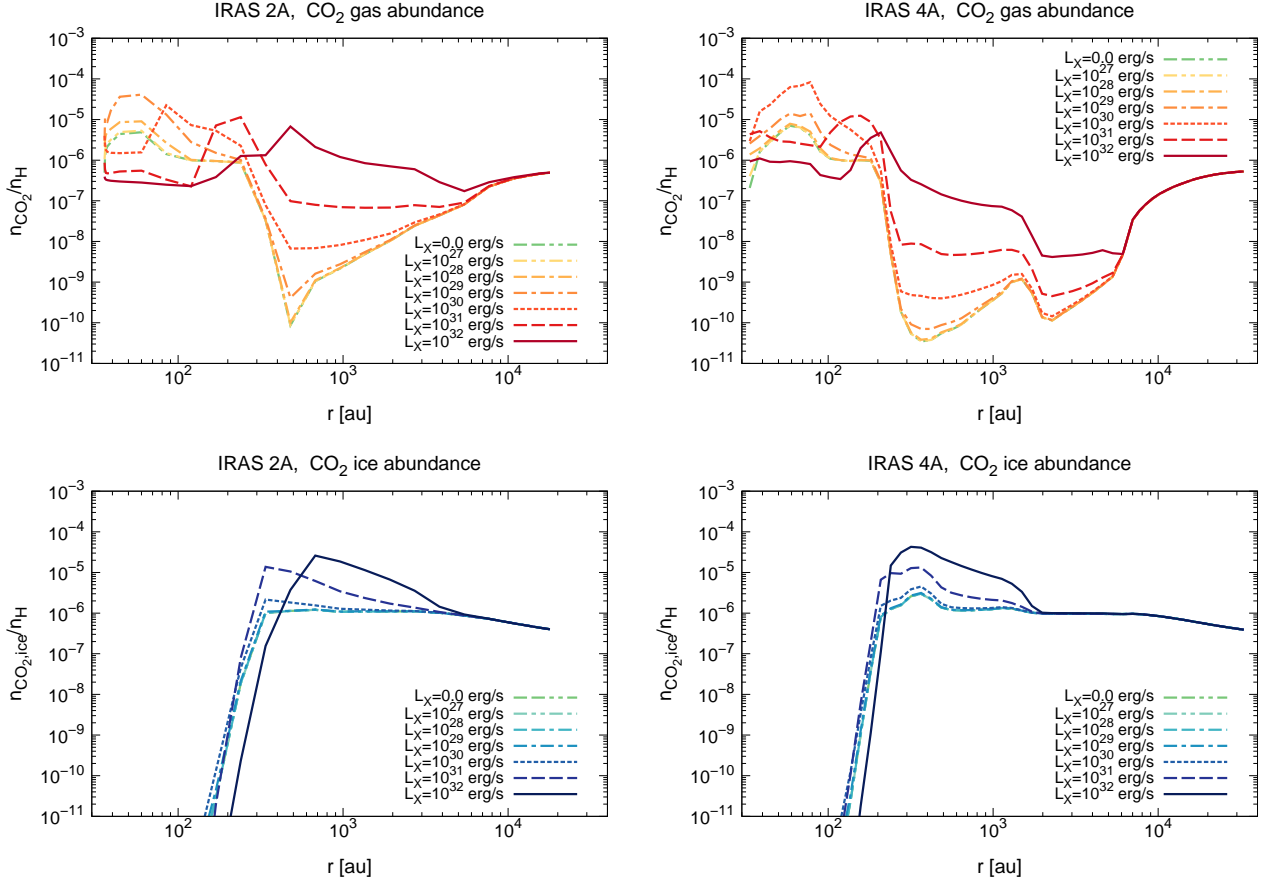


Fig. C.1. The radial profiles of CO₂ gas and ice fractional abundances $n_{\text{CO}_2}/n_{\text{H}}$ (top panels) and $n_{\text{CO}_2,\text{ice}}/n_{\text{H}}$ (bottom panels) in NGC 1333-IRAS 2A (left panels) and NGC 1333-IRAS 4A (right panels) envelope models.

is required to achieve a CO depletion by a factor of 10 and more (Bosman et al. 2018b; Eistrup et al. 2018; Schwarz et al. 2018). Moreover, in the inner envelopes where $\xi_X(r) > \xi_{\text{CR}}(r)$, efficient X-ray induced destruction reactions of other dominant molecules, especially H₂O, consider to supply more atomic oxygen, and it reacts with C⁺ to returning to CO. According to previous studies of chemical modeling with a timescale of $> 10^6$ years, CO is chemically processed and the carbon is sequestered into less volatile species such as CH₃OH, CH₄, and CO₂ (e.g., Furuya & Aikawa 2014; Yu et al. 2016; Bosman et al. 2018b; Schwarz et al. 2018, 2019; Krijt et al. 2020).

According to recent observations with e.g., ALMA, CO gas abundances in the Class 0-I disks with $< 10^6$ years are consistent with the ISM abundance ($\sim 10^{-4}$) within a factor of 2 (Harsono et al. 2014; van't Hoff et al. 2020; Zhang et al. 2020), nearly one order of magnitude higher than the average value in $10^6 - 10^7$ years Class II disks (e.g., Ansdell et al. 2016; Long et al. 2017; Zhang et al. 2019; Bergner et al. 2020).

Appendix D: CH₄, HCN, and C₂H fractional abundances

Top panels of Figure D.1 show the radial profiles of CH₄ gas fractional abundances $n_{\text{CH}_4}/n_{\text{H}}$ in IRAS 2A (left panel) and IRAS 4A (right panel) envelope models, for the various X-ray luminosities. For $L_X \lesssim 10^{28} \text{ erg s}^{-1}$, the CH₄ gas abundances are around $(3 - 8) \times 10^{-6}$ at $r \lesssim 10^3$ au in the IRAS 2A model

and at $r \lesssim 6 \times 10^2$ au in the IRAS 4A model (within the CH₄ snowline). As the X-ray flux becomes large, the CH₄ gas abundances in these radii decrease. For $L_X \gtrsim 10^{31} \text{ erg s}^{-1}$, the CH₄ gas abundances are around $10^{-9} - 10^{-8}$ at $r \lesssim 10^2$ au.

The X-ray induced photodissociation and ion-molecule reactions (with He⁺, H₃⁺ etc.) are considered to be dominant destruction processes of CH₄ in the inner envelopes (e.g., Aikawa et al. 1999; Eistrup et al. 2016). We note that ion-molecule reactions of gas-phase CH₄ with e.g., C⁺ within the CH₄ snowline are important to form unsaturated carbon chain molecules, such as C₂H, C₃H₂, and C₄H (WCCC, e.g., Hassel et al. 2008; Sakai et al. 2008; Sakai & Yamamoto 2013; Aikawa et al. 2012, 2020).

Middle panels of Figure D.1 show the radial profiles of HCN gas fractional abundances $n_{\text{HCN}}/n_{\text{H}}$ in IRAS 2A (left panel) and IRAS 4A (right panel) envelope models, for the various X-ray luminosities. The binding energy of HCN is somewhat smaller than that of H₂O and similar to that of CH₃OH ($E_{\text{des}}(\text{HCN})=3610 \text{ K}$, $E_{\text{des}}(\text{H}_2\text{O})=4880 \text{ K}$, $E_{\text{des}}(\text{CH}_3\text{OH})=3820 \text{ K}$, see Table 2), and the HCN snowline position ($\sim 2 \times 10^2$ au) exists outside the water snowline ($\sim 10^2$ au). For low X-ray luminosities, the HCN gas abundances are around $\sim 10^{-6} - 10^{-5}$ within the HCN snowline. As the X-ray flux becomes large, the HCN gas abundances in these radii decrease. For high X-ray luminosities, the HCN gas abundances are $\lesssim 10^{-9}$ within the HCN snowline. The X-ray induced photodissociation and

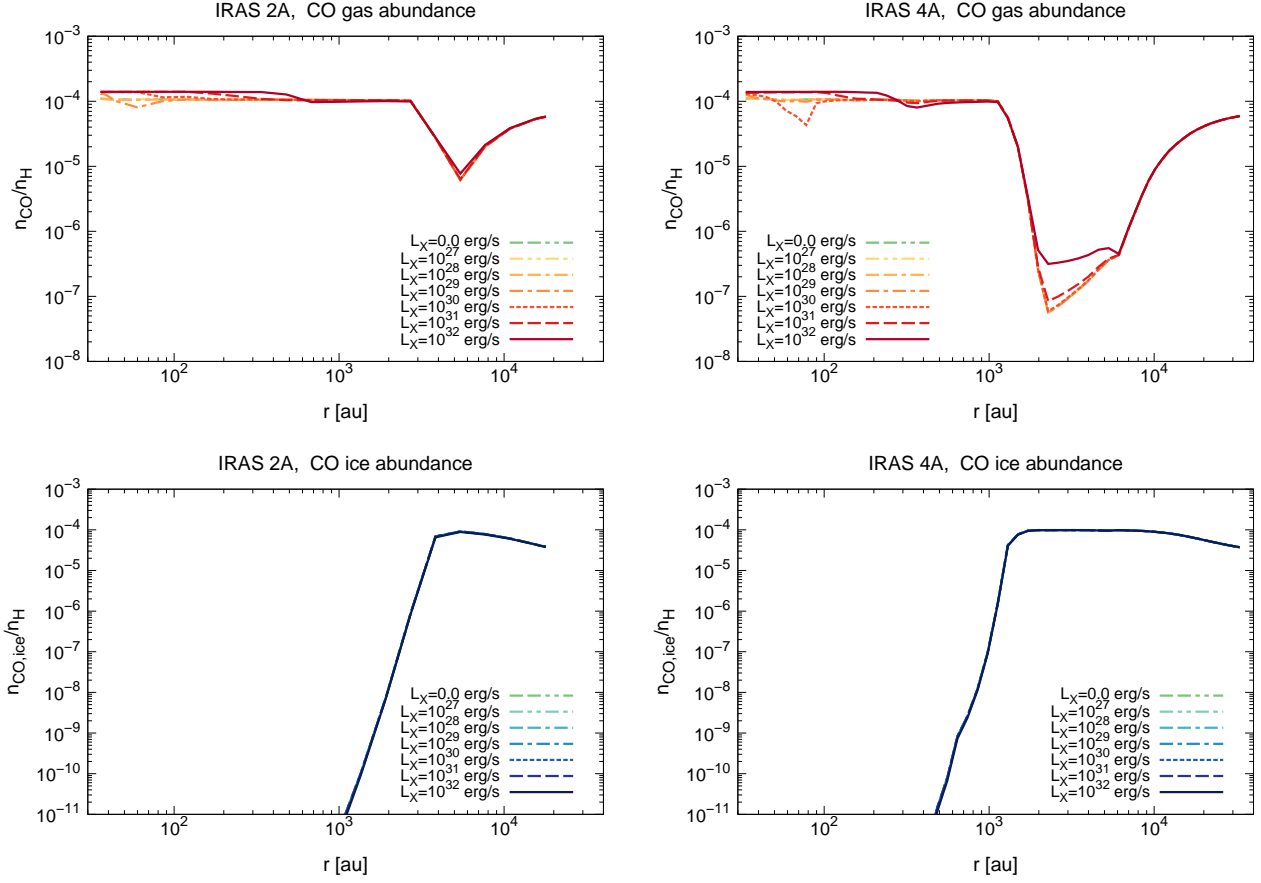


Fig. C.2. The radial profiles of CO gas and ice fractional abundances $n_{\text{CO}}/n_{\text{H}}$ (top panels) and $n_{\text{CO,ice}}/n_{\text{H}}$ (bottom panels) in NGC 1333-IRAS 2A (left panels) and NGC 1333-IRAS 4A (right panels) envelope models.

ion-molecule reactions (with He^+ , H_3^+ etc.) are considered to be dominant destruction processes of HCN in the inner envelopes (e.g., Huntress 1977; van Dishoeck et al. 2006; Walsh et al. 2015).

Bottom panels of Figure D.1 show the radial profiles of C_2H gas fractional abundances $n_{\text{C}_2\text{H}}/n_{\text{H}}$ in IRAS 2A (left panel) and IRAS 4A (right panel) envelope models, for the various X-ray luminosities. The C_2H gas fractional abundances are around $10^{-10} - 10^{-8}$ at $r \gtrsim 10^3$ au, and decrease at the inner radii. Within 10^2 au, they are $\sim 10^{-16} - 10^{-13}$ at IRAS 2A and $\sim 10^{-17} - 10^{-14}$ at IRAS 4A. The dependence of X-ray fluxes are smaller (within two orders of magnitude) than other dominant carbon-bearing molecules such as CH_3OH , HCN, and CH_4 . C_2H is the representative products of WCCC in star-forming cores (e.g., Sakai & Yamamoto 2013; Higuchi et al. 2018; Aikawa et al. 2020, see also Section 4.6), and it is mainly produced by the ion-molecule reaction of CH_4 gas with C^+ and the subsequent electron recombination reaction (Aikawa et al. 2012). C_2H also reacts with C^+ , which links to the formation of longer carbon chain molecules. Henning et al. (2010) discussed that in the atmospheres of Class II disks, the C_2H abundance is larger around Herbig Ae stars with stronger X-rays, than that in T Tauri stars.

Appendix E: NH_3 and N_2 fractional abundances

Top panels of Figure E.1 show the radial profiles of NH_3 gas fractional abundances $n_{\text{NH}_3}/n_{\text{H}}$ in IRAS 2A (left panel) and IRAS 4A (right panel) envelope models, for the various X-ray luminosities. The binding energy of NH_3 is smaller than that of H_2O and HCN, and larger than that of CO_2 ($E_{\text{des}}(\text{NH}_3)=2715$ K, $E_{\text{des}}(\text{HCN})=3610$ K, $E_{\text{des}}(\text{CO}_2)=2267$ K, and $E_{\text{des}}(\text{H}_2\text{O})=4880$ K, see Table 2), and the NH_3 snowline position exists outside the water snowline and the HCN snowline ($> 2 \times 10^2$ au) and inside the CO_2 snowline ($< 3 \times 10^2$ au). Zhang et al. (2018) discussed the possibility to observe the NH_3 line emission (the 23GHz 1,1 and 2,2 lines) with ngVLA as a proxy of the water snowline in disks.

According to Figure E.1, for $L_X \gtrsim 10^{31}$ erg s^{-1} , NH_3 gas abundances become higher (up to $\sim 10^{-8} - 10^{-7}$) outside the NH_3 snowline, compared with the values ($\sim 10^{-9} - 10^{-8}$ in IRAS 2A and $\sim 10^{-10} - 10^{-9}$ in IRAS 4A) for $L_X \lesssim 10^{30}$ erg s^{-1} . The X-ray induced photodesorption is considered to be important in this region. Inside the NH_3 snowline, for low X-ray luminosities, the NH_3 snowline gas abundances are around $\sim 10^{-5}$. As the X-ray fluxes increase, the NH_3 snowline gas abundances in these radii decrease. For $L_X \gtrsim 10^{30}$ erg s^{-1} , the NH_3 gas abundances are $\lesssim 10^{-8} - 10^{-7}$ within the NH_3 snowline. The X-ray induced photodissociation and ion-molecule reactions are considered to be dominant destruction processes of NH_3 in the inner envelopes (e.g., Gredel et al. 1989; Walsh et al. 2015; Eistrup et al.

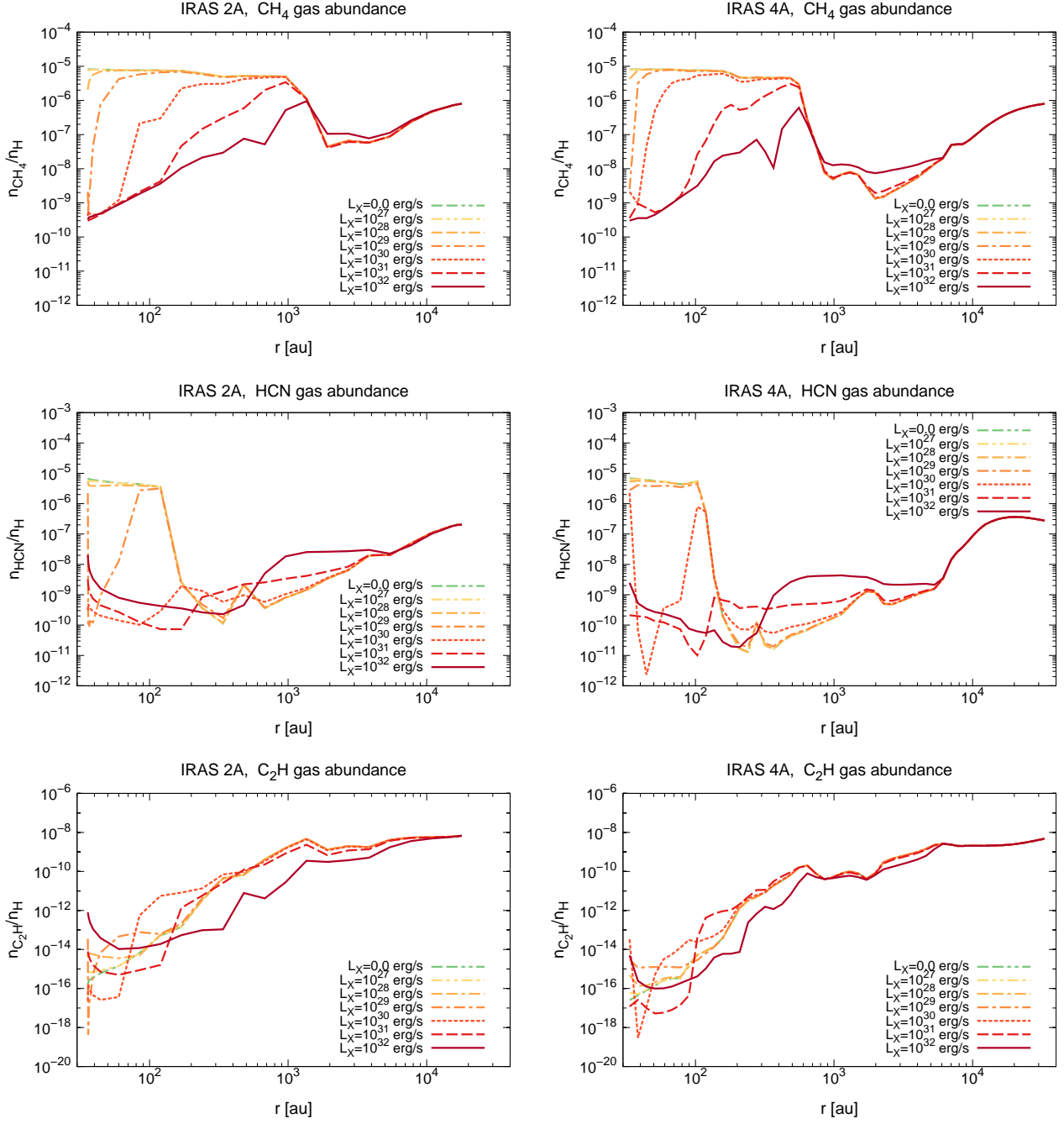


Fig. D.1. [Top panels]: The radial profiles of CH_4 fractional abundances $n_{\text{CH}_4}/n_{\text{H}}$ in NGC 1333-IRAS 2A (left panel) and NGC 1333-IRAS 4A (right panel) envelope models. [Middle panels]: The radial profiles of HCN gas fractional abundances $n_{\text{HCN}}/n_{\text{H}}$ in the IRAS 2A (left panel) and IRAS 4A (right panel) envelope models. [Bottom panels]: The radial profiles of C_2H gas fractional abundances $n_{\text{C}_2\text{H}}/n_{\text{H}}$ in the IRAS 2A (left panel) and IRAS 4A (right panel) envelope models.

2016). Thus, with strong X-ray field, the NH_3 abundance is no longer dominant nitrogen carrier. In addition, it cannot be used as the tracer of the water snowline position, since NH_3 gas abundances are similar within and outside the NH_3 snowline.

The NH_3 line emission (e.g., the 23GHz (1,1), (2,2), and (3,3) lines) have been observed toward protostar disks and envelopes using VLA (e.g., Choi et al. 2007, 2010). However, the spatial resolutions of such VLA observations ($\sim 1.0''$) were not sufficient to resolve the inner structures around the protostars

at a few hundred pc. Future ngVLA observations of these NH_3 lines with much higher resolutions ($\lesssim 0.3''$ at around 23 GHz) will resolve the NH_3 gas emission within its snowline towards many protostars, and can also constrain the impact of X-rays on NH_3 gas abundances. In addition, such observations will be important to trace the chemical history of nitrogen bearing molecules.

Bottom panels of Figure E.1 show the radial profiles of N_2 gas fractional abundances $n_{\text{N}_2}/n_{\text{H}}$ in IRAS 2A (left panel)

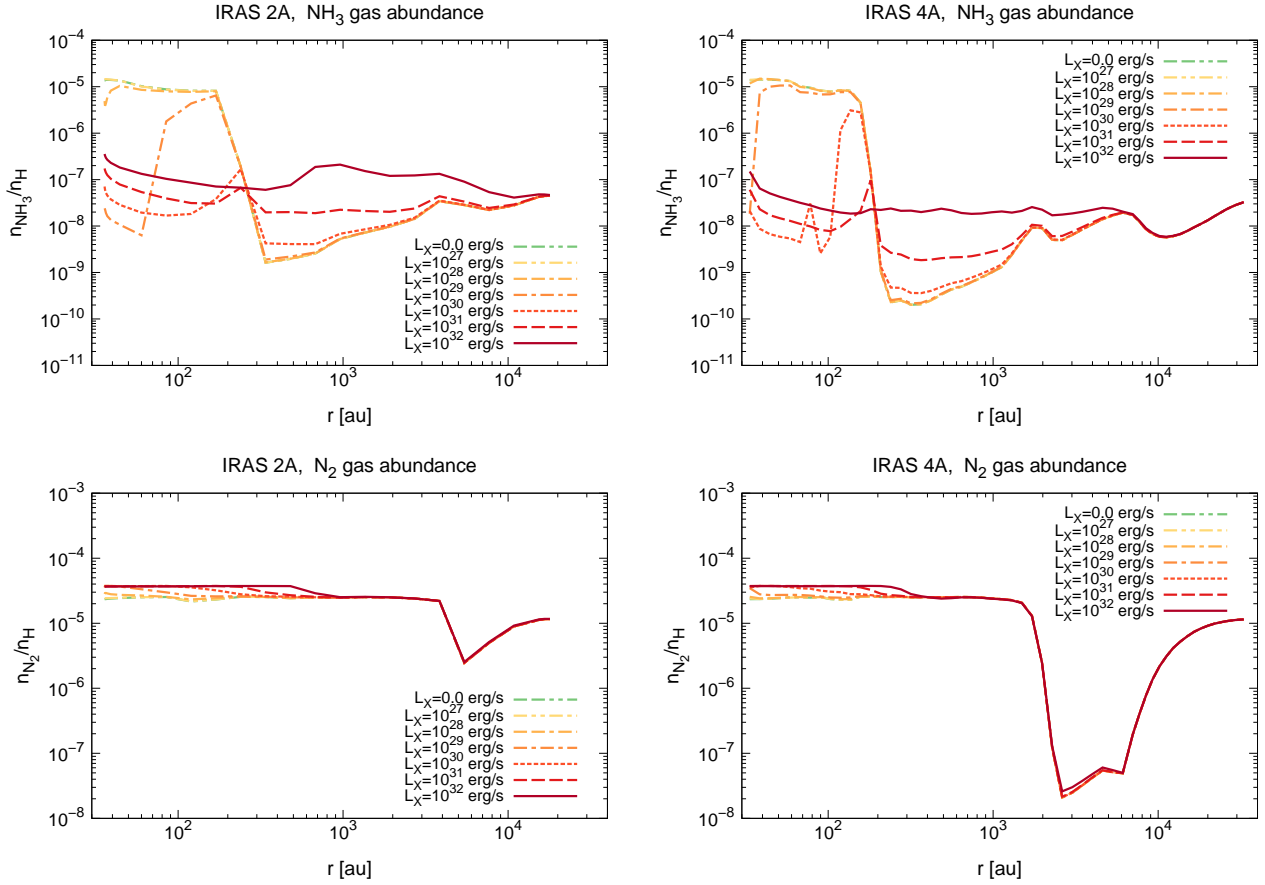


Fig. E.1. [Top panels]: The radial profiles of NH_3 fractional abundances $n_{\text{NH}_3}/n_{\text{H}}$ in NGC 1333-IRAS 2A (left panel) and NGC 1333-IRAS 4A (right panel) envelope models. [Bottom panels]: The radial profiles of N_2 gas fractional abundances $n_{\text{N}_2}/n_{\text{H}}$ in the IRAS 2A (left panel) and IRAS 4A (right panel) envelope models.

and IRAS 4A (right panel) envelope models, for the various X-ray luminosities. Like CO, N_2 gas abundances do not depend on X-ray fluxes.

Appendix F: The fractional abundances and percentage contributions of major oxygen bearing molecules

Table F.1 shows the fractional abundances of major oxygen bearing molecules at $r = 60$ au ($T_{\text{gas}} \sim 150$ K, inside the water snow-line) in the IRAS 2A and IRAS 4A envelope models for the various X-ray luminosities, and their percentage contributions (see also Figures 8 and 9 in Section 4.1). The cut-off threshold is 0.01% for the contributions.

Appendix G: The additional model calculations for X-ray induced photodesorption rates

In Figure G.1 and Figure 11 in Section 4.3, we show the radial profiles of gaseous fractional abundances of H_2O , O_2 , and OH, and icy fractional abundances of H_2O in the IRAS 4A envelope models, for our standard model calculations and additional model calculations. In Figures G.2 and G.3, we show the radial profiles of gaseous fractional abundances of O, HCO^+ , and CH_3OH , and icy fractional abundances of CH_3OH in the IRAS 4A envelope models, for our standard model cal-

culations and additional model calculations. For the additional model calculations in Figures G.1 and G.2, we include the photodesorption by UV photons generated internally via the interaction of secondary electrons produced by X-rays with H_2 molecules. For the additional model calculations in Figure G.3 and Figure 11 in Section 4.3, we switch off the direct X-ray induced photodesorption and include the secondary (indirect) X-ray induced photodesorption only.

According to Figures G.1 and G.2, the effects of such additional secondary (indirect) X-ray induced photodesorption is marginal (the abundances are changed by $<1\%$, see also Section 4.3). For molecules shown in Figure G.3, the differences in abundances between the standard model and the second additional model are much smaller than those in H_2O , OH, and O_2 (see Figure 11 in Section 4.3).

Appendix H: The impacts of the different photodissociation branching ratio and binding energies on the molecular abundances

Figure H.1 shows the gas-phase abundance profiles of H_2O , O_2 , O, and OH, which are calculated assuming the extreme case that the product of H_2O photodissociation is 100% atomic oxygen (Reaction 15 only both in the gas and ice). Figure H.2 shows the gas-phase abundance profiles of H_2O , O_2 , O, and OH, which are obtained from our test calculations assuming the smaller

Table F.1. The fractional abundances of major oxygen bearing molecules at $r = 60$ au ($T_{\text{gas}} \sim 150$ K, inside the water snowline) in the NGC 1333-IRAS 2A and NGC 1333-IRAS 4A envelope models for the various X-ray luminosities, and their percentage contributions relative to the total elemental oxygen abundance (3.2×10^{-4})

L_X [erg s $^{-1}$]	H $_2$ O gas	CO gas	O gas	O $_2$ gas
NGC 1333-IRAS 2A				
0	2.0×10^{-4} , 61%	1.1×10^{-4} , 34%	1.2×10^{-9} , $<10^{-2}\%$	3.7×10^{-7} , $2.3 \times 10^{-1}\%$
10^{27}	2.0×10^{-4} , 61%	1.1×10^{-4} , 33%	2.5×10^{-10} , $<10^{-2}\%$	3.0×10^{-7} , $1.9 \times 10^{-1}\%$
10^{28}	1.9×10^{-4} , 60%	1.1×10^{-4} , 33%	1.7×10^{-10} , $<10^{-2}\%$	1.9×10^{-8} , $1.2 \times 10^{-2}\%$
10^{29}	1.5×10^{-4} , 48%	8.1×10^{-5} , 25%	4.0×10^{-8} , $1.3 \times 10^{-2}\%$	1.5×10^{-6} , $9.2 \times 10^{-1}\%$
10^{30}	1.9×10^{-8} , $<10^{-2}\%$	1.4×10^{-4} , 43%	5.8×10^{-5} , 18%	6.0×10^{-5} , 38%
10^{31}	5.3×10^{-8} , $1.6 \times 10^{-2}\%$	1.4×10^{-4} , 44%	6.2×10^{-5} , 19%	5.9×10^{-5} , 37%
10^{32}	1.4×10^{-7} , $4.5 \times 10^{-2}\%$	1.4×10^{-4} , 44%	6.5×10^{-5} , 20%	5.8×10^{-5} , 36%
NGC 1333-IRAS 4A				
0	2.0×10^{-4} , 62%	1.1×10^{-4} , 33%	1.1×10^{-10} , $<10^{-2}\%$	1.0×10^{-9} , $<10^{-2}\%$
10^{27}	2.0×10^{-4} , 62%	1.1×10^{-4} , 33%	1.1×10^{-10} , $<10^{-2}\%$	1.0×10^{-9} , $<10^{-2}\%$
10^{28}	2.0×10^{-4} , 62%	1.0×10^{-4} , 33%	1.2×10^{-10} , $<10^{-2}\%$	1.0×10^{-9} , $<10^{-2}\%$
10^{29}	1.9×10^{-4} , 60%	9.9×10^{-5} , 31%	2.6×10^{-10} , $<10^{-2}\%$	1.5×10^{-9} , $<10^{-2}\%$
10^{30}	7.0×10^{-5} , 22%	7.2×10^{-5} , 23%	2.0×10^{-7} , $6.3 \times 10^{-2}\%$	2.6×10^{-5} , 16%
10^{31}	1.3×10^{-8} , $<10^{-2}\%$	1.4×10^{-4} , 43%	5.3×10^{-5} , 17%	6.2×10^{-5} , 39%
10^{32}	3.7×10^{-8} , $1.1 \times 10^{-2}\%$	1.4×10^{-4} , 43%	6.2×10^{-5} , 19%	5.9×10^{-5} , 37%

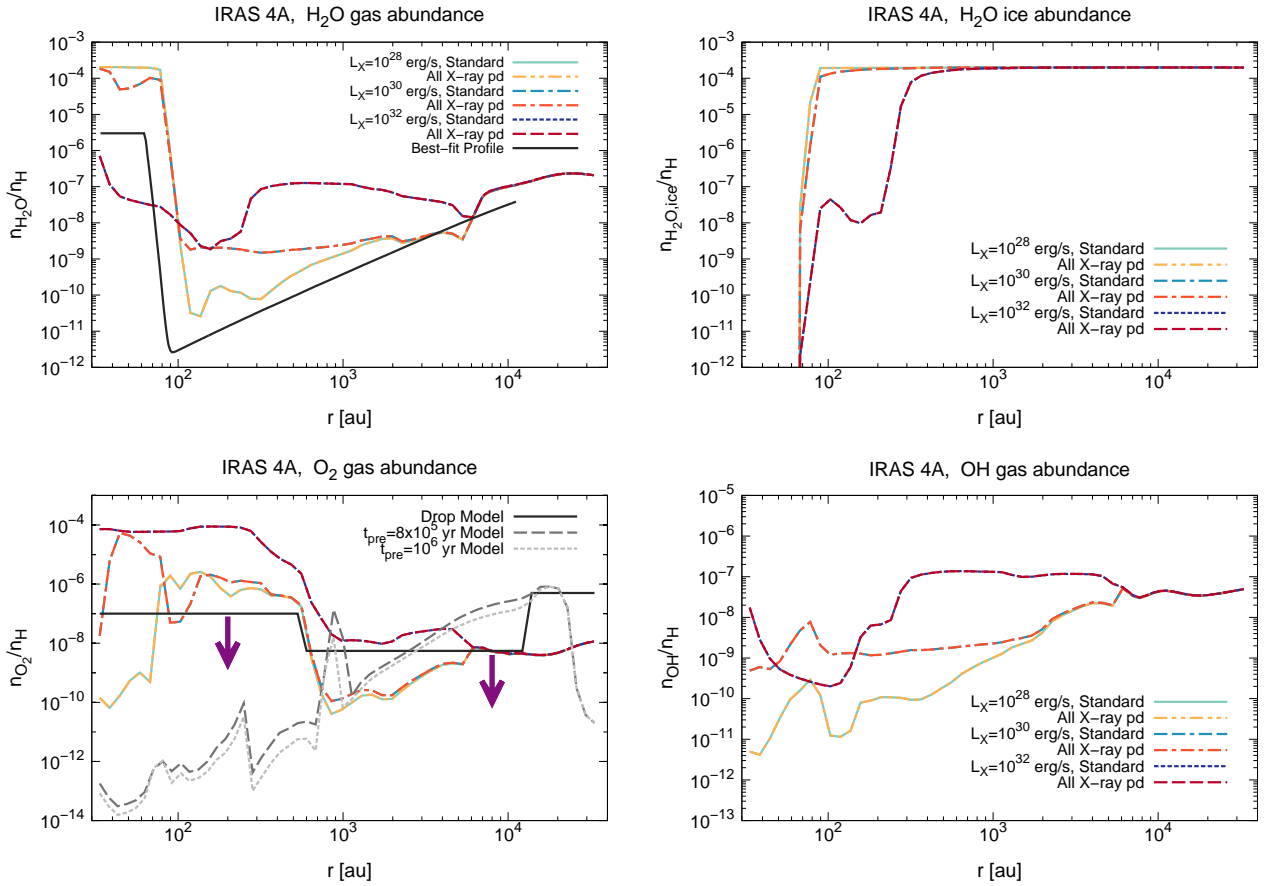


Fig. G.1. The radial profiles of gaseous fractional abundances of H $_2$ O, O $_2$, and OH, and icy fractional abundances of H $_2$ O in the NGC 1333-IRAS 4A envelope models. The light-green solid lines, the cyan double-dashed dotted lines, and blue dotted lines show the radial profiles of our standard model calculations, for values of central star X-ray luminosities $L_X=10^{28}$, 10^{30} , and 10^{32} erg s $^{-1}$, respectively (see also Figures 3, 4, 5, 6). The yellow dashed double-dotted lines, the scarlet dashed dotted lines, and the brown dashed lines show the radial profiles of our additional model calculations for $L_X=10^{28}$, 10^{30} , and 10^{32} erg s $^{-1}$, respectively. In the additional model calculations, we include the photodesorption by UV photons generated internally via the interaction of secondary electrons produced by X-rays with H $_2$ molecules (see also Figure G.2). In the top left panel, the observational best-fit H $_2$ O gas abundance profile obtained in van Dishoeck et al. (2021) is over-plotted with the black solid line (see also Figure 10). In the bottom left panel, the three model O $_2$ gas abundance profiles obtained in Yıldız et al. (2013) are over-plotted (see also Figure 10).

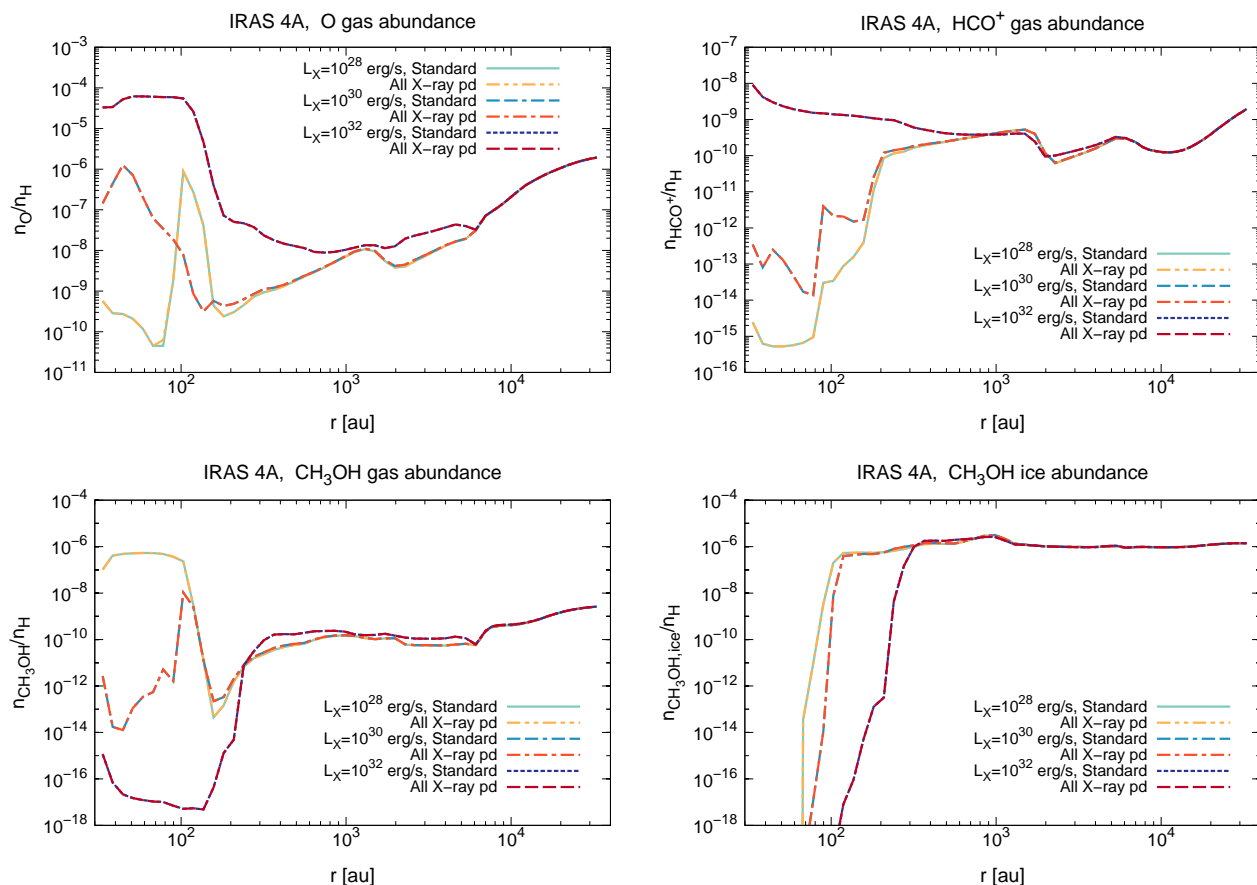


Fig. G.2. The radial profiles of gaseous fractional abundances of O, HCO⁺, and CH₃OH, and icy fractional abundances of CH₃OH in the NGC 1333-IRAS 4A envelope models. The line types and color patterns for the radial profiles of our standard model calculations (see also Figures 5, 6, and 7) and additional model calculations are same as Figure G.1. In the additional model calculations, we include the secondary (indirect) X-ray induced photodesorption (see also Figure G.1).

$E_{\text{des}}(\text{O})$ (= 800 K) than that in our fiducial model (= 1660 K).

We plot these figures in order to investigate the impacts of the different photodissociation branching ratio of H₂O and different binding energies of O on the abundances of H₂O and related molecules. In Section 4.4, we discuss these impacts in detail (see also Figure 12).

References

- Acharyya, K. 2014, *MNRAS*, 443, 1301
- Adams, N. G., Smith, D., & Grief, D. 1978, *International Journal of Mass Spectrometry and Ion Processes*, 26, 405
- Aikawa, Y., Furuya, K., Yamamoto, S., et al. 2020, *ApJ*, 897, 110
- Aikawa, Y., Miyama, S. M., Nakano, T., & Umemayashi, T. 1996, *ApJ*, 467, 684
- Aikawa, Y., Umemayashi, T., Nakano, T., et al. 1999, *ApJ*, 519, 705
- Aikawa, Y., Wakelam, V., Garrod, R. T., et al. 2008, *ApJ*, 674, 984
- Aikawa, Y., Wakelam, V., Hersant, F., et al. 2012, *ApJ*, 760, 40
- Al-Halabi, A., & van Dishoeck, E. F. 2007, *MNRAS*, 382, 1648
- Andrade, D. P. P., Rocco, M. L. M., & Boechat-Roberty, H. M. 2010, *MNRAS*, 409, 1289
- Ansdell, M., Williams, J. P., van der Marel, N., et al. 2016, *ApJ*, 828, 46
- Arakawa, S. & Krijt, S. 2021, *ApJ*, 910, 130
- Arasa, C., Andersson, S., Cuppen, H. M., et al. 2010, *J. Chem. Phys.*, 132, 184510
- Arasa, C., Koning, J., Kroes, G.-J., et al. 2015, *A&A*, 575, A121
- Barzel, B. & Biham, O. 2007, *ApJ*, 658, L37
- Basalgète, R., Dupuy, R., Féraud, G., et al. 2021a, *A&A*, 647, A35
- Basalgète, R., Dupuy, R., Féraud, G., et al. 2021b, *A&A*, 647, A36
- Baulch, D. L., Cobos, C. J., Cox, R. A., et al. 1992, *Journal of Physical and Chemical Reference Data*, 21, 411
- Benz, A. O., Bruderer, S., van Dishoeck, E. F., et al. 2016, *A&A*, 590, A105
- Berger, M. J., Hubbell, J. H., Seltzer, S. M., Coursey, J. S., & Zucker, D. S. 1999, XCOM: Photon Cross Section Database (version 1.5). Online Available: <https://www.nist.gov/pml/xcom-photon-cross-sections-database> (National Institute of Standards and Technology, Gaithersburg, MD)
- Bergner, J. B., Öberg, K. I., Bergin, E. A., et al. 2020, *ApJ*, 898, 97
- Bertin, M., Romanzin, C., Doronin, M., et al. 2016, *ApJ*, 817, L12
- Bianchi, E., Chandler, C. J., Ceccarelli, C., et al. 2020, *MNRAS*, 498, L87
- Bjerkeli, P., Jørgensen, J. K., Bergin, E. A., et al. 2016, *A&A*, 595, A39
- Boogert, A. C. A., Gerakines, P. A., & Whittet, D. C. B. 2015, *ARA&A*, 53, 541
- Boonman, A. M. S., van Dishoeck, E. F., Lahuis, F., et al. 2003, *A&A*, 399, 1063
- Bosman, A. D., Bruderer, S., & van Dishoeck, E. F. 2017, *A&A*, 601, A36
- Bosman, A. D., Tielens, A. G. G. M., & van Dishoeck, E. F. 2018a, *A&A*, 611, A80
- Bosman, A. D., Walsh, C., & van Dishoeck, E. F. 2018b, *A&A*, 618, A182
- Bruderer, S., Benz, A. O., Stäuber, P., et al. 2010, *ApJ*, 720, 1432
- Bruderer, S., Doty, S. D., & Benz, A. O. 2009, *ApJS*, 183, 179
- Cardelli, J. A., Meyer, D. M., Jura, M., et al. 1996, *ApJ*, 467, 334
- Cardelli, J. A., Savage, B. D., & Ebbets, D. C. 1991, *ApJ*, 383, L23
- Carty, D., Goddard, A., Kahler, S. P. K., Sims, I. R., & Smith, I. W. M. 2006, *J. Phys. Chem. A*, 110, 3101
- Caselli, P., Hasegawa, T. I., & Herbst, E. 1998, *ApJ*, 495, 309
- Caselli, P., Keto, E., Bergin, E. A., et al. 2012, *ApJ*, 759, L37
- Ceccarelli, C., Dominik, C., López-Sepulcre, A., et al. 2014, *ApJ*, 790, L1
- Charnley, S. B., Tielens, A. G. G. M., & Millar, T. J. 1992, *ApJ*, 399, L71
- Choi, M., Tatematsu, K., & Kang, M. 2010, *ApJ*, 723, L34
- Choi, M., Tatematsu, K., Park, G., et al. 2007, *ApJ*, 667, L183
- Chuang, K.-J., Fedoseev, G., Ioppolo, S., et al. 2016, *MNRAS*, 455, 1702
- Cieza, L. A., Casassus, S., Tobin, J., et al. 2016, *Nature*, 535, 258
- Cleeves, L. I., Bergin, E. A., & Adams, F. C. 2014, *ApJ*, 794, 123
- Cleeves, L. I., Bergin, E. A., Öberg, K. I., et al. 2017, *ApJ*, 843, L3

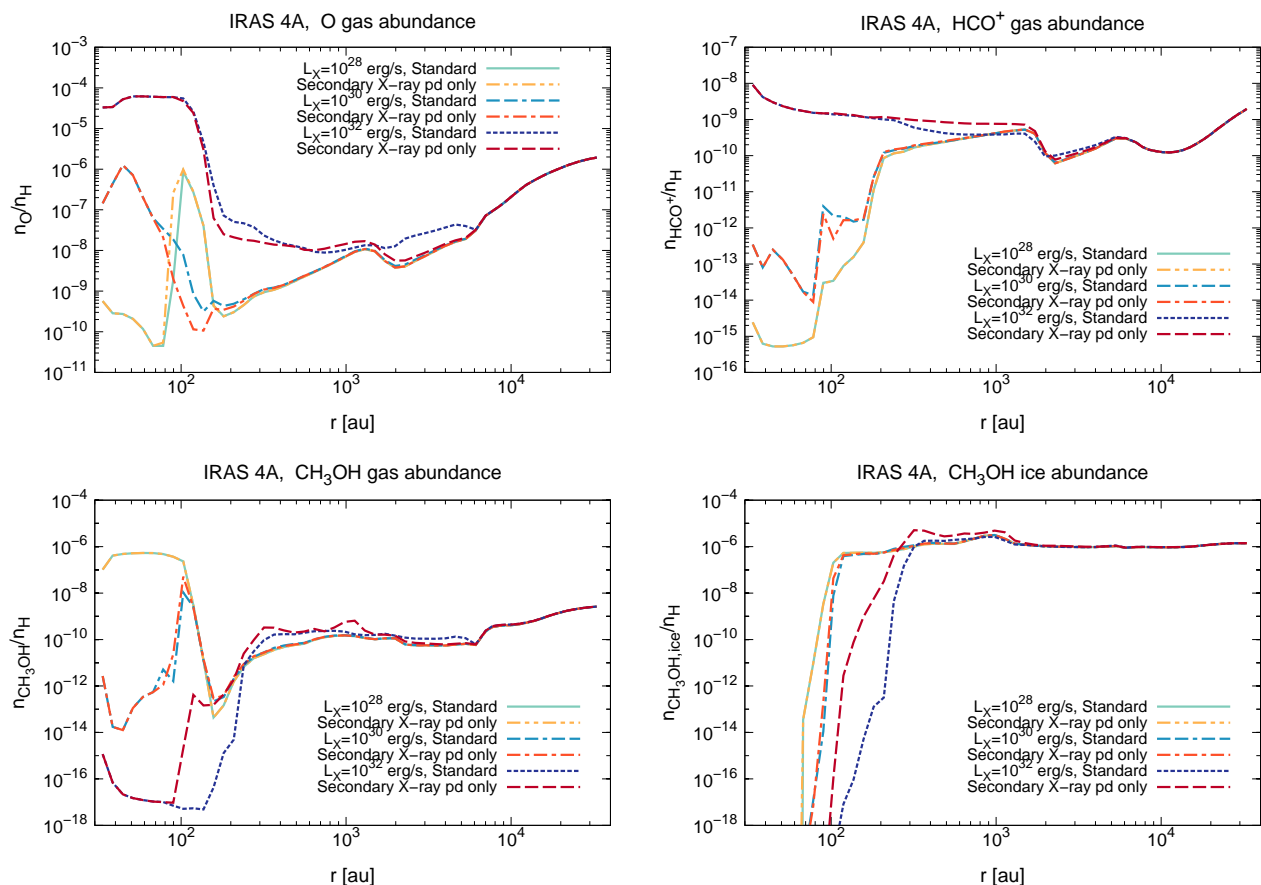


Fig. G.3. The radial profiles of gaseous fractional abundances of O, HCO⁺, and CH₃OH, and icy fractional abundances of CH₃OH in the NGC 1333-IRAS 4A envelope models. The profiles are same as Figure G.2, except in the additional model calculations we switch off the direct X-ray induced photodesorption and include the secondary (indirect) X-ray induced photodesorption only (see also Figure 11).

Collings, M. P., Anderson, M. A., Chen, R., et al. 2004, *MNRAS*, 354, 1133
Coutens, A., Commerçon, B., & Wakelam, V. 2020, *A&A*, 643, A108
Coutens, A., Vastel, C., Cabrit, S., et al. 2013, *A&A*, 560, A39
Coutens, A., Vastel, C., Caux, E., et al. 2012, *A&A*, 539, A132
Crownover, R. L., De Lucia, F. C., & Herbst, E. 1990, *ApJ*, 349, L29
Cruz-Díaz, G. A., Martín-Doménech, R., Muñoz Caro, G. M., et al. 2016, *A&A*, 592, A68
Cuppen, H. M., Ioppolo, S., Romanzin, C., et al. 2010, *Physical Chemistry Chemical Physics (Incorporating Faraday Transactions)*, 12, 12077
Cuppen, H. M., van Dishoeck, E. F., Herbst, E., et al. 2009, *A&A*, 508, 275
Cuppen, H. M., Walsh, C., Lamberts, T., et al. 2017, *Space Sci. Rev.*, 212, 1
De Simone, M., Ceccarelli, C., Codella, C., et al. 2020, *ApJ*, 896, L3
Drozdovskaya, M. N., Walsh, C., van Dishoeck, E. F., et al. 2016, *MNRAS*, 462, 977
Drozdovskaya, M. N., Walsh, C., Visser, R., et al. 2014, *MNRAS*, 445, 913
Dulieu, F., Congiu, E., Noble, J., et al. 2013, *Scientific Reports*, 3, 1338
Dunham, M. M., Stutz, A. M., Allen, L. E., et al. 2014, in *Protostars and Planets VI*, ed. H. Beuther et al. (Tucson, AZ: Univ. Arizona Press), 195
Dupuy, R., Bertin, M., Féraud, G., et al. 2018, *Nature Astronomy*, 2, 796
Eistrup, C. & Walsh, C. 2019, *A&A*, 621, A75
Eistrup, C., Walsh, C., & van Dishoeck, E. F. 2016, *A&A*, 595, A83
Eistrup, C., Walsh, C., & van Dishoeck, E. F. 2018, *A&A*, 613, A14
Enoch, M. L., Evans, N. J., Sargent, A. I., et al. 2008, *ApJ*, 684, 1240
Evans, N. J., Dunham, M. M., Jørgensen, J. K., et al. 2009, *ApJS*, 181, 321
Favre, C., López-Sepulcre, A., Ceccarelli, C., et al. 2017, *A&A*, 608, A82
Fillion, J.-H., Fayolle, E. C., Michaut, X., et al. 2014, *Faraday Discussions*, 168, 533
Forbrich, J., Preibisch, T., & Menten, K. M. 2006, *A&A*, 446, 155
Fuchs, G. W., Cuppen, H. M., Ioppolo, S., et al. 2009, *A&A*, 505, 629
Furuya, K., & Aikawa, Y. 2014, *ApJ*, 790, 97
Furuya, K., Drozdovskaya, M. N., Visser, R., et al. 2017, *A&A*, 599, A40
Furuya, K., van Dishoeck, E. F., & Aikawa, Y. 2016, *A&A*, 586, A127
Garrod, R. T., & Herbst, E. 2006, *A&A*, 457, 927
Garrod, R. T. 2008, *A&A*, 491, 239

Garrod, R. T., & Pauly, T. 2011, *ApJ*, 735, 15
Garrod, R. T., Vasyunin, A. I., Semenov, D. A., et al. 2009, *ApJ*, 700, L43
Garrod, R. T., Widicus Weaver, S. L., & Herbst, E. 2008, *ApJ*, 682, 283
Geppert, W. D., Hamberg, M., Thomas, R. D., et al. 2006, *Faraday Discussions*, 133, 177
Giardino, G., Favata, F., Micela, G., et al. 2007, *A&A*, 463, 275
Graedel, T. E., Langer, W. D., & Frerking, M. A. 1982, *ApJS*, 48, 321
Gredel, R., Lepp, S., & Dalgarno, A. 1987, *ApJ*, 323, L137
Gredel, R., Lepp, S., Dalgarno, A., et al. 1989, *ApJ*, 347, 289
Grosso, N., Hamaguchi, K., Principe, D. A., et al. 2020, *A&A*, 638, L4
Glassgold, A. E., Najita, J., & Igea, J. 1997, *ApJ*, 480, 344
Güdel, M., & Nazé, Y. 2009, *A&A Rev.*, 17, 309
Hamaguchi, K., Corcoran, M. F., Petre, R., et al. 2005, *ApJ*, 623, 291
Harsono, D., Bruderer, S., & van Dishoeck, E. F. 2015, *A&A*, 582, A41
Harsono, D., Jørgensen, J. K., van Dishoeck, E. F., et al. 2014, *A&A*, 562, A77
Harsono, D., Persson, M. V., Ramos, A., et al. 2020, *A&A*, 636, A26
Hasegawa, T. I., & Herbst, E. 1993, *MNRAS*, 261, 83
Hasegawa, T. I., Herbst, E., & Leung, C. M. 1992, *ApJS*, 82, 167
Hassel, G. E., Herbst, E., & Garrod, R. T. 2008, *ApJ*, 681, 1385
He, J., Jing, D., & Vidalí, G. 2014, *Physical Chemistry Chemical Physics (Incorporating Faraday Transactions)*, 16, 3493
He, J., & Vidalí, G. 2014, *ApJ*, 788, 50
Heays, A. N., Bosman, A. D., & van Dishoeck, E. F. 2017, *A&A*, 602, A105
Heinzeller, D., Nomura, H., Walsh, C., & Millar, T. J. 2011, *ApJ*, 731, 115
Henning, T., Semenov, D., Guilloteau, S., et al. 2010, *ApJ*, 714, 1511
Herbst, E., & van Dishoeck, E. F. 2009, *ARA&A*, 47, 427
Herczeg, G. J., Johnstone, D., Mairs, S., et al. 2017, *ApJ*, 849, 43
Higuchi, A. E., Sakai, N., Watanabe, Y., et al. 2018, *ApJS*, 236, 52
Hofner, P., & Churchwell, E. 1997, *ApJ*, 486, L39
Hogerheijde, M. R., & van der Tak, F. F. S. 2000, *A&A*, 362, 697
Hollenbach, D., Kaufman, M. J., Bergin, E. A., et al. 2009, *ApJ*, 690, 1497
Hodapp, K. W., Chini, R., Watermann, R., et al. 2012, *ApJ*, 744, 56
Hsieh, T.-H., Murillo, N. M., Belloche, A., et al. 2019, *ApJ*, 884, 149
Huntress, W. T. 1977, *ApJS*, 33, 495

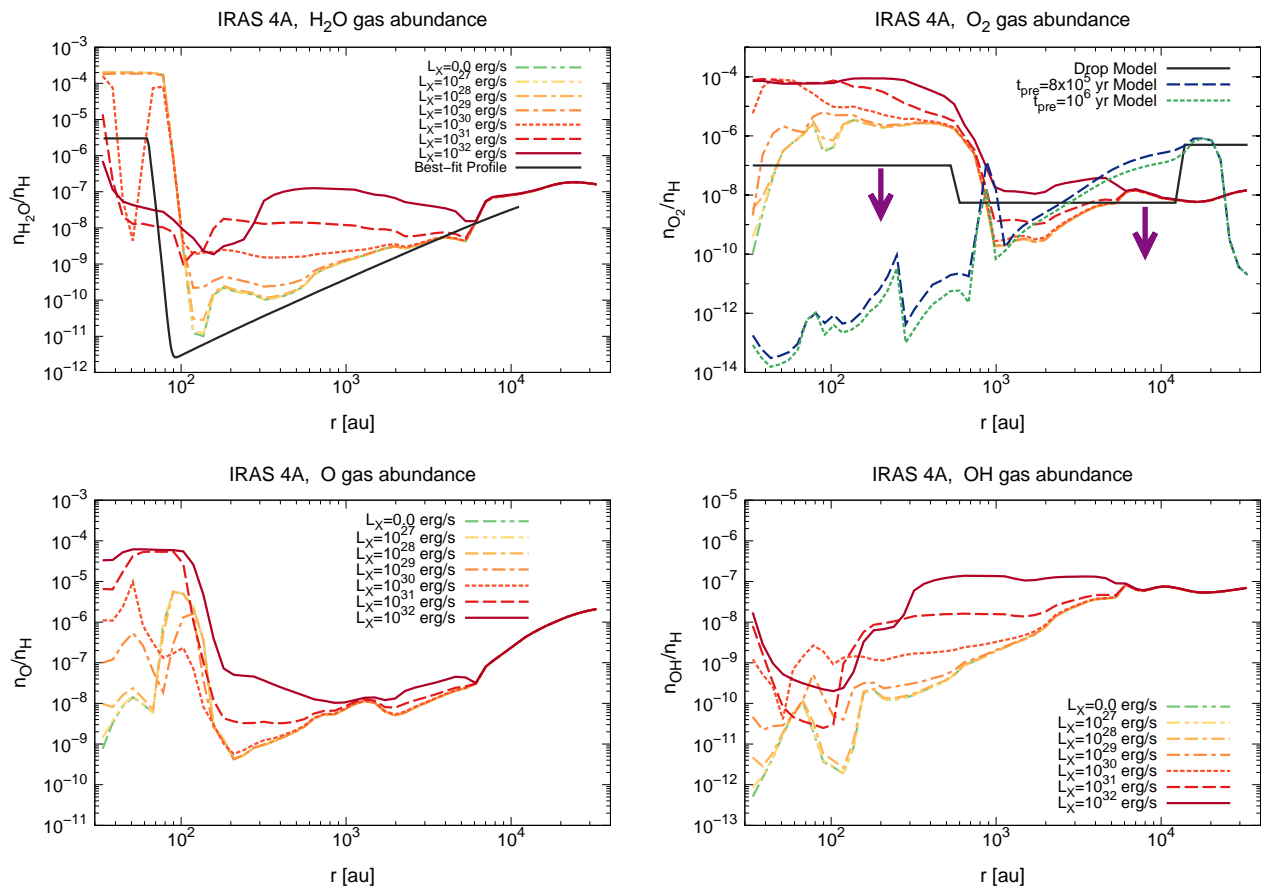


Fig. H.1. The radial profiles of gaseous fractional abundances of H_2O , O_2 , O , and OH in NGC 1333-IRAS 4A envelope models. These profiles are obtained from our test calculations assuming that the product of H_2O photodissociation is 100% atomic oxygen, unlike our fiducial model (100% OH). In the top left panel, the observational best-fit H_2O gas abundance profile obtained in van Dishoeck et al. (2021) is over-plotted with the black solid line (see also Figure 10). In the top right panel, the three model O_2 gas abundance profiles obtained in Yıldız et al. (2013) are over-plotted (see also Figure 10).

Igea, J. & Glassgold, A. E. 1999, *ApJ*, 518, 848
 Imai, M., Sakai, N., Oya, Y., et al. 2016, *ApJ*, 830, L37
 Imanishi, K., Koyama, K., & Tsuboi, Y. 2001, *ApJ*, 557, 747
 Ivezić, Z., & Elitzur, M. 1997, *MNRAS*, 287, 799
 Jensen, S. S., Jørgensen, J. K., Kristensen, L. E., et al. 2019, *A&A*, 631, A25
 Jørgensen, J. K., Belloche, A., & Garrod, R. T. 2020, *ARA&A*, 58, 727
 Jørgensen, J. K., Bourke, T. L., Myers, P. C., et al. 2007, *ApJ*, 659, 479
 Jørgensen, J. K., & van Dishoeck, E. F. 2010, *ApJ*, 710, L72
 Jørgensen, J. K., van Dishoeck, E. F., Visser, R., et al. 2009, *A&A*, 507, 861
 Jørgensen, J. K., Visser, R., Sakai, N., et al. 2013, *ApJ*, 779, L22
 Kamezaki, T., Imura, K., Omodaka, T., et al. 2014, *ApJS*, 211, 18
 Karska, A., Herczeg, G. J., van Dishoeck, E. F., et al. 2013, *A&A*, 552, A141
 Koumpia, E., Semenov, D. A., van der Tak, F. F. S., et al. 2017, *A&A*, 603, A88
 Krijt, S., Bosman, A. D., Zhang, K., et al. 2020, *ApJ*, 899, 134
 Kristensen, L. E. & Dunham, M. M. 2018, *A&A*, 618, A158
 Kristensen, L. E., Gusdorf, A., Mottram, J. C., et al. 2017, *A&A*, 601, L4
 Kristensen, L. E., van Dishoeck, E. F., Bergin, E. A., et al. 2012, *A&A*, 542, A8
 Kristensen, L. E., Visser, R., van Dishoeck, E. F., et al. 2010, *A&A*, 521, L30
 Lamberts, T., Cuppen, H. M., Ioppolo, S., et al. 2013, *Physical Chemistry Chemical Physics (Incorporating Faraday Transactions)*, 15, 8287
 Lee, J.-E., Lee, S., Baek, G., et al. 2019, *Nature Astronomy*, 3, 314
 Lee, S., Lee, J.-E., Aikawa, Y., et al. 2020, *ApJ*, 889, 20
 Leemker, M., van't Hoff, M. L. R., Trapman, L., et al. 2021, *A&A*, 646, A3
 Leger, A., Jura, M., & Omont, A. 1985, *A&A*, 144, 147
 Li, J. I.-H., Liu, H. B., Hasegawa, Y., et al. 2017, *ApJ*, 840, 72
 Long, F., Herczeg, G. J., Pascucci, I., et al. 2017, *ApJ*, 844, 99
 Maloney, P. R., Hollenbach, D. J., & Tielens, A. G. G. M. 1996, *ApJ*, 466, 561
 Marboeuf, U., Thiabaud, A., Alibert, Y., et al. 2014, *A&A*, 570, A35
 McElroy, D., Walsh, C., Markwick, A. J., et al. 2013, *A&A*, 550, A36
 Melnick, G. J., Tolls, V., Snell, R. L., et al. 2020, *ApJ*, 892, 22
 Meyer, D. M., Jura, M., & Cardelli, J. A. 1998, *ApJ*, 493, 222
 Miotello, A., Testi, L., Lodato, G., et al. 2014, *A&A*, 567, A32

Mottram, J. C., van Dishoeck, E. F., Schmalzl, M., et al. 2013, *A&A*, 558, A126
 Neufeld, D. A., Lepp, S., & Melnick, G. J. 1995, *ApJS*, 100, 132
 Nisini, B., Santangelo, G., Giannini, T., et al. 2015, *ApJ*, 801, 121
 Noble, J. A., Congiu, E., Dulieu, F., et al. 2012, *MNRAS*, 421, 768
 Noble, J. A., Theule, P., Congiu, E., et al. 2015, *A&A*, 576, A91
 Nomura, H., Aikawa, Y., Nakagawa, Y., et al. 2009, *A&A*, 495, 183
 Nomura, H., Aikawa, Y., Tsujimoto, M., Nakagawa, Y., & Millar, T. J. 2007, *ApJ*, 661, 334
 Nomura, H. & Millar, T. J. 2004, *A&A*, 414, 409
 Notsu, S., Akiyama, E., Booth, A., et al. 2019, *ApJ*, 875, 96
 Notsu, S., Eistrup, C., Walsh, C., & Nomura, H. 2020, *MNRAS*, 499, 2229
 Notsu, S., Nomura, H., Ishimoto, D., Walsh, C., Honda, M., Hirota, T., & Millar, T. J. 2017, *ApJ*, 836, 118
 Notsu, S., Nomura, H., Ishimoto, D., Walsh, C., Honda, M., Hirota, T., & Millar, T. J. 2016, *ApJ*, 827, 113
 Notsu, S., Nomura, H., Walsh, C., et al. 2018, *ApJ*, 855, 62
 Öberg, K. I. & Bergin, E. A. 2021, *Phys. Rep.*, 893, 1
 Öberg, K. I., Boogert, A. C. A., Pontoppidan, K. M., et al. 2011, *ApJ*, 740, 109
 Öberg, K. I., Cleeves, L. I., & Loomis, R. 2018, in *Astronomical Society of the Pacific Conference Series, Monograph 7, Science with a Next Generation Very Large Array*, Eric J. Murphy, ed. (San Francisco, CA: ASP), 223
 Öberg, K. I., Fuchs, G. W., Awad, Z., et al. 2007, *ApJ*, 662, L23
 Öberg, K. I., Garrod, R. T., van Dishoeck, E. F., & Linnartz, H. 2009c, *A&A*, 504, 891
 Öberg, K. I., Linnartz, H., Visser, R., & van Dishoeck, E. F. 2009b, *ApJ*, 693, 1209
 Öberg, K. I., van Broekhuizen, F., Fraser, H. J., et al. 2005, *ApJ*, 621, L33
 Öberg, K. I., van Dishoeck, E. F., & Linnartz, H. 2009a, *A&A*, 496, 281
 Okuzumi, S., Tanaka, H., Kobayashi, H., et al. 2012, *ApJ*, 752, 106
 Okuzumi, S. & Tazaki, R. 2019, *ApJ*, 878, 132
 Oldenberg, R. C., Loge, G. W., Harradine, D. M., & Winn, K. R. 1992, *J. Phys. Chem.*, 96, 8426

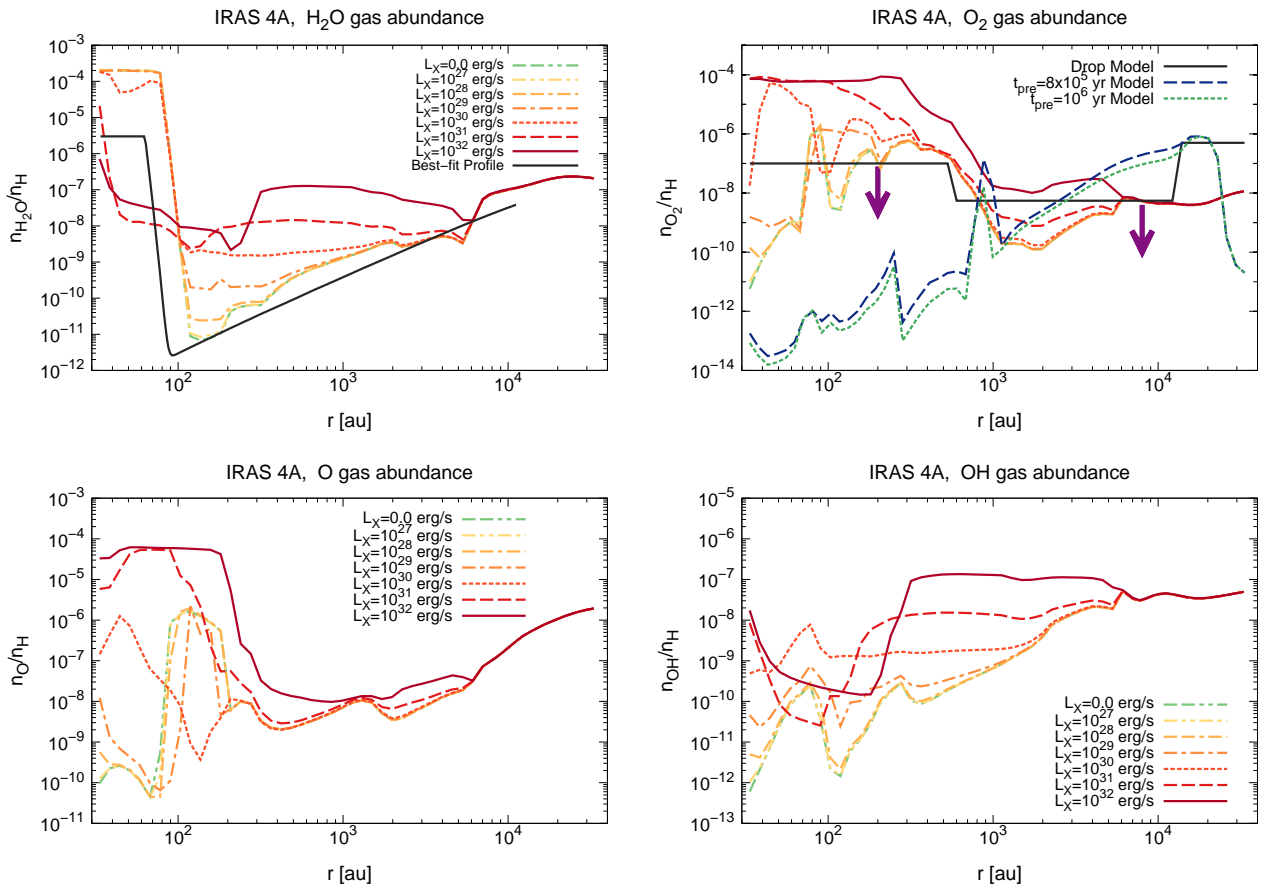


Fig. H.2. The radial profiles of gaseous fractional abundances of H_2O , O_2 , O , and OH in NGC 1333-IRAS 4A envelope models. These profiles are obtained from our test calculations assuming the smaller $E_{\text{des}}(j)$ for atomic oxygen ($= 800$ K) than that in our fiducial model ($= 1660$ K). In the top left panel, the observational best-fit H_2O gas abundance profile obtained in van Dishoeck et al. (2021) is over-plotted with the black solid line (see also Figures 10 and H.1). In the top right panel, the three model O_2 gas abundance profiles obtained in Yıldız et al. (2013) are over-plotted (see also Figure 10 and H.1).

Ormel, C. W., Paszun, D., Dominik, C., et al. 2009, *A&A*, 502, 845
Oya, Y., Sakai, N., López-Sepulcre, A., et al. 2016, *ApJ*, 824, 88
Padovani, M., Marcowith, A., Hennebelle, P., et al. 2016, *A&A*, 590, A8
Prasad, S. S. & Tarafdar, S. P. 1983, *ApJ*, 267, 603
Penteado, E. M., Walsh, C., & Cuppen, H. M. 2017, *ApJ*, 844, 71
Persson, M. V., Harsono, D., Tobin, J. J., et al. 2016, *A&A*, 590, A33
Persson, M. V., Jørgensen, J. K., & van Dishoeck, E. F. 2012, *A&A*, 541, A39
Persson, M. V., Jørgensen, J. K., & van Dishoeck, E. F. 2013, *A&A*, 549, L3
Persson, M. V., Jørgensen, J. K., van Dishoeck, E. F., et al. 2014, *A&A*, 563, A74
Poteet, C. A., Pontoppidan, K. M., Megeath, S. T., et al. 2013, *ApJ*, 766, 117
Preibisch, T. 2003, *A&A*, 410, 951
Preibisch, T., Kim, Y.-C., Favata, F., et al. 2005, *ApJS*, 160, 401
Sahu, D., Liu, S.-Y., Su, Y.-N., et al. 2019, *ApJ*, 872, 196
Sakai, N., Sakai, T., Hirota, T., et al. 2008, *ApJ*, 672, 371
Sakai, N., & Yamamoto, S. 2013, *Chemical Reviews*, 113, 8981
Schöier, F. L., Jørgensen, J. K., van Dishoeck, E. F., et al. 2002, *A&A*, 390, 1001
Schoonenberg, D., & Ormel, C. W. 2017, *A&A*, 602, A21
Schmalzl, M., Visser, R., Walsh, C., et al. 2014, *A&A*, 572, A81
Schwarz, K. R., Bergin, E. A., Cleaves, L. I., et al. 2018, *ApJ*, 856, 85
Schwarz, K. R., Bergin, E. A., Cleaves, L. I., et al. 2019, *ApJ*, 877, 131
Smith, R. S., May, R. A., & Kay, B. D. 2016, *J. Phys. Chem. B*, 120, 1979
Stantcheva, T. & Herbst, E. 2004, *A&A*, 423, 241
Stäuber, P., Benz, A. O., Jørgensen, J. K., et al. 2007, *A&A*, 466, 977
Stäuber, P., Doty, S. D., van Dishoeck, E. F., et al. 2005, *A&A*, 440, 949
Stäuber, P., Jørgensen, J. K., van Dishoeck, E. F., et al. 2006, *A&A*, 453, 555
Takasao, S., Tomida, K., Iwasaki, K., et al. 2019, *ApJ*, 878, L10
Taquet, V., Charnley, S. B., & Sipilä, O. 2014, *ApJ*, 791, 1
Taquet, V., Furuya, K., Walsh, C., et al. 2016b, *MNRAS*, 462, S99
Taquet, V., van Dishoeck, E. F., Swayne, M., et al. 2018, *A&A*, 618, A11
Taquet, V., Wirström, E. S., & Charnley, S. B. 2016a, *ApJ*, 821, 46
Tielens, A. G. G. M., & Hagen, W. 1982, *A&A*, 114, 245
Turrini, D., Schisano, E., Fonte, S., et al. 2021, *ApJ*, 909, 40

Umeybayashi, T. & Nakano, T. 2009, *ApJ*, 690, 69
van Dishoeck, E. F., Bergin, E. A., Lis, D. C., & Lunine, J. I. 2014, in *Protostars and Planets VI*, ed. H. Beuther et al. (Tucson, AZ: Univ. Arizona Press), 835
van Dishoeck, E. F., Helmich, F. P., de Graauw, T., et al. 1996, *A&A*, 315, L349
van Dishoeck, E. F., Herbst, E., & Neufeld, D. A. 2013, *Chemical Reviews*, 113, 9043
van Dishoeck, E. F., Jonkheid, B., & van Hemert, M. C. 2006, *Faraday Discussions*, 133, 231
van Dishoeck, E. F., Kristensen, L. E., Benz, A. O., et al. 2011, *PASP*, 123, 138
van Dishoeck, E. F., Kristensen, L. E., Mottram, J. C., et al. 2021, *A&A*, in press (arXiv:2102.02225)
van Harrevelt, R. & van Hemert, M. C. 2008, *Journal of Physical Chemistry A*, 112, 3002
van't Hoff, M. L. R., Harsono, D., Tobin, J. J., et al. 2020, *ApJ*, 901, 166
van't Hoff, M. L. R., Persson, M. V., Harsono, D., et al. 2018a, *A&A*, 613, A29
van't Hoff, M. L. R., Tobin, J. J., Trapman, L., et al. 2018b, *ApJ*, 864, L23
Vasyunin, A. I. & Herbst, E. 2013, *ApJ*, 762, 86
Vasyunin, A. I., Semenov, D. A., Wiebe, D. S., et al. 2009, *ApJ*, 691, 1459
Verner, D. A., Yakovlev, D. G., Band, I. M., et al. 1993, *Atomic Data and Nuclear Data Tables*, 55, 233
Visser, R., Bergin, E. A., & Jørgensen, J. K. 2015, *A&A*, 577, A102
Visser, R., Doty, S. D., & van Dishoeck, E. F. 2011, *A&A*, 534, A132
Visser, R., Jørgensen, J. K., Kristensen, L. E., et al. 2013, *ApJ*, 769, 19
Visser, R., Kristensen, L. E., Bruderer, S., et al. 2012, *A&A*, 537, A55
Visser, R., van Dishoeck, E. F., Doty, S. D., et al. 2009, *A&A*, 495, 881
Wada, K., Tanaka, H., Okuzumi, S., et al. 2013, *A&A*, 559, A62
Waggoner, A. R. & Cleaves, L. I. 2019, *ApJ*, 883, 197
Walsh, C., Loomis, R. A., Öberg, K. I., et al. 2016, *ApJ*, 823, L10
Walsh, C., Millar, T. J., & Nomura, H. 2010, *ApJ*, 722, 1607
Walsh, C., Herbst, E., Nomura, H., et al. 2014b, *Faraday Discussions*, 168, 389
Walsh, C., Millar, T. J., Nomura, H., et al. 2014a, *A&A*, 563, A33

- Walsh, C., Nomura, H., Millar, T. J., et al. 2012, *ApJ*, 747, 114
- Walsh, C., Nomura, H., & van Dishoeck, E. 2015, *A&A*, 582, A88
- Walsh, C., Vissapragada, S., & McGee, H. 2018, *Proceedings of the International Astronomical Union, IAU Symposium*, 332, 395
- Watanabe, N., & Kouchi, A. 2002, *ApJ*, 571, L173
- Whittet, D. C. B. 2010, *ApJ*, 710, 1009
- Woitke, P., Thi, W.-F., Kamp, I., et al. 2009, *A&A*, 501, L5
- Woods, P. M., Slater, B., Raza, Z., et al. 2013, *ApJ*, 777, 90
- Yang, Y.-L., Sakai, N., Zhang, Y., et al. 2021, *ApJ*, 910, 20
- Yıldız, U. A., Acharyya, K., Goldsmith, P. F., et al. 2013, *A&A*, 558, A58
- Yıldız, U. A., Kristensen, L. E., van Dishoeck, E. F., et al. 2012, *A&A*, 542, A86
- Yoneda, H., Tsukamoto, Y., Furuya, K., et al. 2016, *ApJ*, 833, 105
- Yoo, H., Lee, J.-E., Mairs, S., et al. 2017, *ApJ*, 849, 69
- Yu, M., Willacy, K., Dodson-Robinson, S. E., et al. 2016, *ApJ*, 822, 53
- Zhang, K., Bergin, E. A., Schwarz, K., et al. 2019, *ApJ*, 883, 98
- Zhang, K., Bergin, E. A., Williams, J. P., et al. 2018, in *Astronomical Society of the Pacific Conference Series, Monograph 7, Science with a Next Generation Very Large Array*, Eric J. Murphy, ed. (San Francisco, CA: ASP), 209
- Zhang, K., Schwarz, K. R., & Bergin, E. A. 2020, *ApJ*, 891, L17